

University of Louisville

ThinkIR: The University of Louisville's Institutional Repository

Electronic Theses and Dissertations

5-2022

Properties of 25Cr7Ni stainless steel fabricated through laser-powder bed fusion.

Arulselvan Arumugham Akilan
University of Louisville

Follow this and additional works at: <https://ir.library.louisville.edu/etd>



Part of the [Manufacturing Commons](#), and the [Metallurgy Commons](#)

Recommended Citation

Arumugham Akilan, Arulselvan, "Properties of 25Cr7Ni stainless steel fabricated through laser-powder bed fusion." (2022). *Electronic Theses and Dissertations*. Paper 3803.
<https://doi.org/10.18297/etd/3803>

This Doctoral Dissertation is brought to you for free and open access by ThinkIR: The University of Louisville's Institutional Repository. It has been accepted for inclusion in Electronic Theses and Dissertations by an authorized administrator of ThinkIR: The University of Louisville's Institutional Repository. This title appears here courtesy of the author, who has retained all other copyrights. For more information, please contact thinkir@louisville.edu.

PROPERTIES OF 25CR7NI STAINLESS STEEL
FABRICATED THROUGH LASER-POWDER BED
FUSION

By

Arulsevan Arumugham Akilan

A Dissertation
Submitted to the Faculty of the
J.B. Speed School of Engineering of the University of Louisville
in Fulfilment of the Requirements
for the Degree of

Doctor of Philosophy
in Mechanical Engineering

Department of Mechanical Engineering
University of Louisville
Louisville, Kentucky, United States

May 2022

Copyright by Arulselvan Arumugham Akilan
May 2022
All rights reserved

PROPERTIES OF 25CR7NI STAINLESS FABRICATED
THROUGH LASER-POWDER BED FUSION

By

Arulseivan Arumugham Akilan

A Dissertation Approved on

16 December 2021

By the following Dissertation
Committee

Dr. Sundar V. Atre
Dissertation Chair

Dr. Kunal H. Kate
Committee member

Dr. Thomas A. Berfield
Committee member

Dr. Gautam Gupta
Committee member

ACKNOWLEDGEMENT

At the outset I'd like to extend my profound gratitude to Prof. Dr. Sundar V. Atre, Endowed Chair of Manufacturing and Materials, *University of Louisville*, for taking me under his mentorship and helping me to navigate through my entire doctoral program. He always persisted in pointing out where I was lacking and has helped me to evolve. Thank you, sir. I'd also like to thank my PhD committee including Dr. Kunal H. Kate, who was always approachable to discuss about research or any other aspects of the doctoral program, Dr. Gautam Gupta, who was very instrumental in easing my way into the world of corrosion & Dr. Thomas A. Berfield, who's keen insights helped me shape my work.

I would like to take this opportunity to thank the visiting scholars and my collaborators Dr. Vamsi K. Balla, Dr. Dharmendra Chalasani, Dr. Azim Gokce whose invaluable contributions were instrumental in giving a defined shape to my dissertation. I would also like to thank Dr. Kevin Murphy, Dr. Jacek Jasinski, Dr. Ellen G. Brehob for their support at various stages of my doctoral program. I also recognize and appreciate the valuable help afforded by John Jones, Dianne Jenne & Gary Graf during the course of my doctoral program.

My dissertation wouldn't have been possible without multiple collaborating organizations and the corresponding collaborators namely, Jerome Stanley, *Hoeganaes AB*, Dr. Peter Harlin, *Sandvik Additive*, Chad Beamer, *Quintus*, Dr. Jagannadh Satyavolu, *Conn Centre for Renewable Energy Research* & James P. Adams, *MPIF*, Thank you all.

My friends in the Materials Innovation Guild, *University of Louisville*, namely Qasim, Subrata, Param, Pavan, Kavish, Saleh, Athira, were always source of joy and inspiration in between the hectic research life and I will always cherish their friendship.

Finally, my family whose strength & sacrifice keeps me striving to better myself every day.

I dedicate this work to you all....

ABSTRACT

PROPERTIES OF 25CR7NI STAINLESS STEEL FABRICATED BY LASER-POWDER BED FUSION

Arulselvan Arumugham Akilan

16 December 2021

Stainless steel is a low carbon high alloyed system with higher concentrations of Cr & Ni, which impart high corrosion resistance to them. Alloys with approximately 25% Cr & 7% Ni in their chemical composition are commercially referred to as 'Super Duplex Stainless Steel'. They have a unique phase composition of approximately 50% ferrite & 50% austenite, yielding a robust combination of high mechanical strength & corrosion resistance. They find extensive interest & application in the fields which demand a longer service life under intense mechanical / corrosive environment such as offshore oil rigs & pipelines in nuclear power plants. Traditional thermal processing and fabrication of super duplex stainless steel are fraught with limitations and shortcomings in terms of detrimental phase formation. Laser-Powder Bed Fusion is a form of additive manufacturing that involves layer wise addition and consolidation of metal powders in near net shape parts. The process is characterized by high cooling rates to the tune of 10^7 K/s. This unique characteristic allows for the suppression of formation of detrimental phases and is leveraged in processing of super duplex stainless steels. The available literature on L-PBF fabrication of super duplex stainless steel in comparison to conventional stainless steel alloys is quite lacking. This study quantitatively established the influence of the Laser-Powder Bed Fusion (L-PBF) process parameters, starting powder attributes, chemical composition, inert atmosphere & Hot Isostatic Pressing (HIP) on the as-printed properties of the fabricated super duplex stainless steel samples. As-printed samples of a gas atomized super duplex stainless steel yielded the highest UTS, yield strength and comparable corrosion resistance to wrought-annealed, MIM, PM, L-PBF literature super duplex stainless steel. Economical water atomized super duplex stainless steel powder was used to fabricate samples which had higher UTS, yield strength & comparable corrosion resistance to wrought-annealed stainless steel.

TABLE OF CONTENTS

CHAPTER 1 INTRODUCTION.....	1
Preamble.....	1
CHAPTER 2 INFLUENCE OF LASER-POWDER BED FUSION PROCESS PARAMETERS ON THE AS-PRINTED PROPERTIES OF LASER-POWDER BED FUSION FABRICATED 25CR7NI STAINLESS STEEL	7
Introduction.....	7
Methodology	8
Results & Discussion.....	11
Conclusions	23
CHAPTER 3 INFLUENCE OF HOT ISOSTATIC PRESSING ON THE PROPERTIES OF LASER-POWDER BED FUSION FABRICATED 25CR7NI STAINLESS STEEL	24
Introduction.....	24
Methodology.....	24
Results & Discussion.....	26
Conclusions	30
CHAPTER 4 INFLUENCE OF POWDER CHARACTERISTICS & CHEMICAL COMPOSITION ON THE PROPERTIES OF 25CR7NI STAINLESS STEEL FABRICATED BY LASER-POWDER BED FUSION	32
Introduction.....	32
Methodology	33
Results & Discussion.....	35
Conclusions	43
CHAPTER 5 INFLUENCE OF PROCESSING ATMOSPHERE ON THE PROPERTIES OF LASER-POWDER BED FUSION FABRICATED 25CR7NI STAINLESS STEEL	44
Introduction.....	44
Methodology	44
Results & Discussion.....	46
Conclusions	50
CHAPTER 6 CONCLUSIONS & FUTURE WORK	52

Conclusions	52
Future Work	54
REFERENCES	56
APPENDIX 1 CORROSION PROPERTIES OF LASER-POWDER BED FUSION FABRICATED 25CR7NI STAINLESS STEELS	66
APPENDIX 2 LASER POWDER BED FUSION OF IN-SITU COMPOSITES USING DRY MIXED TI6AL4V AND SI ₃ N ₄ POWDER	69
CURRICULUM VITAE.....	73

LIST OF TABLES

Table 1.1 Collated literature on L-PBF Fabricated 25Cr7Ni Stainless steel.....	4
Table 2.1 Comparison of Starting Powder Composition.....	10
Table 2.2 Process Parameters of L-PBF used in this study	11
Table 2.3 Mechanical properties of L-PBF water atomized 25Cr7Ni stainless steel ..	14
Table 2.4 Variation of corrosion properties of as-printed samples with energy density	20
Table 3.1 Mechanical Properties of 25Cr7Ni Stainless Steel	27
Table 3.2 Corrosion Properties of 25Cr7Ni Stainless Steel	30
Table 4.1 Composition of starting gas atomized 25Cr7Ni stainless steel powder	34
Table 4.2 Comparison of Corrosion Properties	41
Table 5.1 Chemical Compositions	48
Table 5.2 Comparison of Mechanical Properties	49
Table 5.3 Comparison of Corrosion Properties	52
Table 7.1 Comparison of Chemical Composition	59
Table 7.2 Comparison of Corrosion Properties	60
Table 8.1 L-PBF Process Parameters	62
Table 8.2 Composition of different microstructural constituents observed in the L-PBF processed Ti-TiN-Ti5Si3 in-situ composites	64

LIST OF FIGURES

Figure 1.1 Variation of Corrosion rate as a function of UTS from wrought stainless steel alloys	2
Figure 1.2 Schematic representation of detrimental phases	2
Figure 1.3 High cooling rates of L-PBF process responsible for prevention of detrimental phase evolution represented in Temperature – Time – Transformation diagram	3
Figure 1.4 Relative number of literatures on different stainless steel alloys processed by L-PBF	4
Figure 2.1 SEM micrograph of the starting powder used in the study	10
Figure 2.2 Variation of as print sample density with energy density	12
Figure 2.3 Light micrographs of as-printed L-PBF samples in (left) build direction (BD) (right) scan direction (SD) fabricated at different energy densities	13
Figure 2.4 Variation of (a) ultimate tensile strength (b) yield strength (c) elongation (d) hardness as a function of the density of as-printed 25Cr7Ni stainless steel of novel composition samples	15
Figure 2.5 XRD pattern of the wrought 25Cr7Ni stainless steel, starting 25Cr7Ni stainless steel powder of novel composition, L-PBF as-printed 25Cr7Ni stainless steel of novel composition sample.....	16
Figure 2.6 Optical micrographs of electro-etched as-printed L-PBF samples in the build direction printed at all the energy densities, the dotted lines indicating a melt-pool	17
Figure 2.7 EBSD maps of (left) texture, (middle) phases for as-printed L-PBF samples @ 63J/mm ³ along the build direction (right) phases for wrought 25Cr7Ni stainless steel samples	18
Figure 2.8 Linear sweep voltammetry (LSV) curves of three as-printed L-PBF 25Cr7Ni stainless steel samples at all energy densities in aerated aqueous solution containing 3.5 wt.% of NaCl	19

Figure 2.9 Variation of (a) polarization resistance, (b) corrosion current, (c) corrosion rate, (d) breakdown potential as a function of Archimedes density of as-printed L-PBF 25Cr7Ni stainless steel	20
Figure 2.10 Light micrographs of as-printed L-PBF specimen stainless steel samples for varying energy densities in the scan direction XY plane (left) before corrosion testing (right) after corrosion testing	22
Figure 2.11 SEM micrographs of L-PBF WA 25Cr7Ni SS sample @ 63 J/mm ³ (Left) before corrosion testing (Right) after corrosion testing	23
Figure 3.1 Micrographs of unetched sample in as-printed (left), printed+ HIP ₁₀₀₀ condition (middle) and printed+ HIP ₁₁₇₀ condition (right)	26
Figure 3.2 XRD profiles of 25Cr7Ni stainless steel samples	28
Figure 3.3 Optical micrographs of electro-etched as-printed (47 J/mm ³), HIP treated samples of L-PBF fabricated water atomized 25Cr7Ni stainless steel along the build direction (ZX)	28
Figure 3.4 SEM micrographs / Cr EDS elemental maps of electro-etched HIP treated samples of L-PBF fabricated water atomized 25Cr7Ni stainless steel along the build direction (ZX)	29
Figure 4.1 SEM micrographs of (left) water atomized 25Cr7Ni powder (right) gas atomized 25Cr7Ni powder	35
Figure 4.2 Optical micrographs of L-PBF (left) water atomized 25Cr7Ni samples (right) gas atomized 25Cr7Ni samples	36
Figure 4.3 Comparison of mechanical properties	38
Figure 4.4 Collated XRD profiles of (top) L-PBF water atomized (middle) L-PBF gas atomized (bottom) wrought – annealed 25Cr7Ni samples	39
Figure 4.5 Optical micrographs of electro-etched L-PBF (left) water atomized 25Cr7Ni samples (right) gas atomized 25Cr7Ni samples along the build direction (ZX)	39
Figure 4.6 SEM micrographs of electro-etched L-PBF gas atomized 25Cr7Ni sample along the build direction (ZX)	40

Figure 4.7 Tafel plots from the linear sweep voltammetry experiments collated with (black) L-PBF sample from water atomized (green) wrought – annealed (orange) L-PBF sample from gas atomized 25Cr7Ni stainless steel	40
Figure 4.8 (Left) Optical micrograph of corroded & eletroetched, (right) SEM micrograph of corroded & un-etched L-PBF gas atomized sample	42
Figure 4.9 Eletroetched optical micrographs of L-PBF samples from gas atomized (GA) powders, wrought – annealed 25Cr7Ni stainless steel	42
Figure 5.1 As-printed L-PBF samples fabricated from gas atomized 25Cr7Ni stainless steel under N atmosphere	49
Figure 5.2 Polished optical micrographs along build direction (ZX)	49
Figure 5.3 Collated XRD profiles of wrought & L-PBF samples	50
Figure 5.4 Electro-etched optical micrographs of L-PBF samples	50
Figure 5.5 Electro-etched SEM micrographs of 25Cr7Ni L-PBF sample printed in N atmosphere	51
Figure 5.6 Energy Dispersive Spectroscopy of 25Cr7Ni L-PBF sample printed in N atmosphere	51
Figure 5.7 Comparison of (left) Tafel plots, (right) Nyqvist plots of 25Cr7Ni L-PBF samples	52
Figure 6.1 L-PBF fabricated water atomized 25Cr7Ni stainless steel based flange....	58
Figure 6.2 Comparison of simulation data with experimental data of L-PBF fabricated 25Cr7Ni stainless steel cube under N atmosphere	58
Figure 7.1 Comparison of densities and porosities of as-printed samples	59
Figure 7.2 Collated XRD profiles of different 25Cr7Ni stainless steel samples	59
Figure 7.3 FRA – LSV corrosion setup	60
Figure 7.4 FRA / LSV curves for a set of wrought – annealed 25Cr7Ni , L-PBF fabricated water atomized & gas atomized 25Cr7Ni stainless steels	60
Figure 7.5 Electro-etched 25Cr7Ni stainless steel samples	60

Figure 7.6 Electro-etched corroded sample of a L-PBF fabricated gas atomized 25Cr7Ni stainless steel	61
Figure 7.7 EDS maps of electro-etched corroded sample of a L-PBF fabricated gas atomized 25Cr7Ni stainless steel	61
Figure 8.1 SEM images showing the size distribution and morphology of Ti6Al4V alloy and Si 3N4 powder used in this investigation	62
Figure 8.2 Powder bed photographs showing the changes in the powder spreading during L-PBF of Ti-TiN -Ti ₅ Si ₃ in-situ composites	63
Figure 8.3 Low-magnification microstructures of L-PBF processed Ti-TiN-Ti ₅ Si ₃ in-situ composites showing the influence of laser energy density	63
Figure 8.4 (a) XRD analysis showing in-situ reaction products in LL-PBF processed TMCs and (b) Typical microstructural features of Ti-TiN-Ti ₅ Si ₃ in-situ composites (89 J/mm ³) and their compositional analysis (c and d)	64
Figure 8.5 (a) Typical SEM microstructures showing the scale and distribution of microstructural features such as grain size and in-situ reaction products in LL-PBF processed Ti-TiN-Ti ₅ Si ₃ in-situ composites. (b) Schematic in-situ reaction forming Ti-TiN-Ti ₅ Si ₃ in-situ composites during LL-PBF of Ti6Al4V+5 wt.% Si ₃ N ₄ dry-mixed feedstock	65

CHAPTER 1 INTRODUCTION

Preamble

Stainless steel alloys are low carbon, high alloyed systems of Fe primarily with Cr and Ni, known for their high strength and corrosion resistance. In addition, Mo, Si, Mn, N are some of the other important alloying elements which forms the basis elemental composition of the stainless steel alloy system. The primary allotropic forms of Fe are delta ferrite (with BCC crystal structure, stable between 1394° C – 1538° C), gamma austenite (with FCC crystal structure, stable between 912° C – 1394° C), alpha ferrite (with BCC crystal structure, stable below 912° C). The different families of stainless steels are categorized based on the relative fractions of these allotropic forms of Fe along with certain other phases such as martensite (result of diffusion-less transformation of austenite) and precipitates at room temperature. The relative amounts of different alloying elements enable the room temperature stability of the different allotropes.

Different crystallographic structures and elemental compositions yield a set of unique properties to different families of stainless steels. Austenitic stainless steels are 300 series family of stainless steels composed of about 16 – 26 % Cr & 10 – 22 % Ni, with the microstructure being primarily austenite. This family of the stainless steels offer the highest corrosion resistance among all available grades of steels. The steels are non-magnetic and are not hardenable through heat treatment. Martensitic stainless steels contain between 11 – 18% Cr and up to 1.2% C. They are hardenable through heat treatment and have a lesser corrosion resistance than austenitic stainless steels. Precipitation hardening stainless steels are Cr – Ni steels along with precipitation hardening elements such as Cu, Ti & Al. The microstructure is either ferritic or martensitic. These types of steels are geared towards heat resistant applications such as gears and bearings [1–3].

Applications such as offshore oil rigs / chemical digester plants / piping in nuclear power plants present a unique challenge in terms of service environment and service life. A combination of a high mechanical stress and an intense corrosion environment coupled with the necessity for longer service life due to limitations to accessibility presented the case for the development of specialized stainless-steel alloys. Super duplex stainless steel, an alloy of approximately 25% Cr, 7% Ni, 0.3% Mo, 0.2% N was developed during the early part of the 21st century. With the right heat treatment cycle, the chemical composition renders the alloy with approximately 50% ferrite and 50% austenite. This specific composition has also been standardized by ASTM under the designation UNS 32750 [4,5]. This class of stainless steel will be referred to as 25Cr7Ni stainless steel throughout this study.

Figure 1.1 collates the corrosion rate in 3.5 wt% NaCl, of wrought alloys of different stainless-steel grades as a function of their UTS. We can see that the 25Cr7Ni stainless steel alloys offer a robust combination of lower corrosion rate while having a moderately high strength in comparison to austenitic (316L), Martensitic (420), precipitation hardening (17-4 PH) stainless steels. Such a robust combination of mechanical and corrosion properties, which is one of the primary value additions of 25Cr7Ni stainless steels are predominantly due to the approximately 50% ferrite and 50% austenite along with the presence of 27% Cr, 5% Ni, 0.3% Mo, 0.2% N within the stainless steel matrix [6].

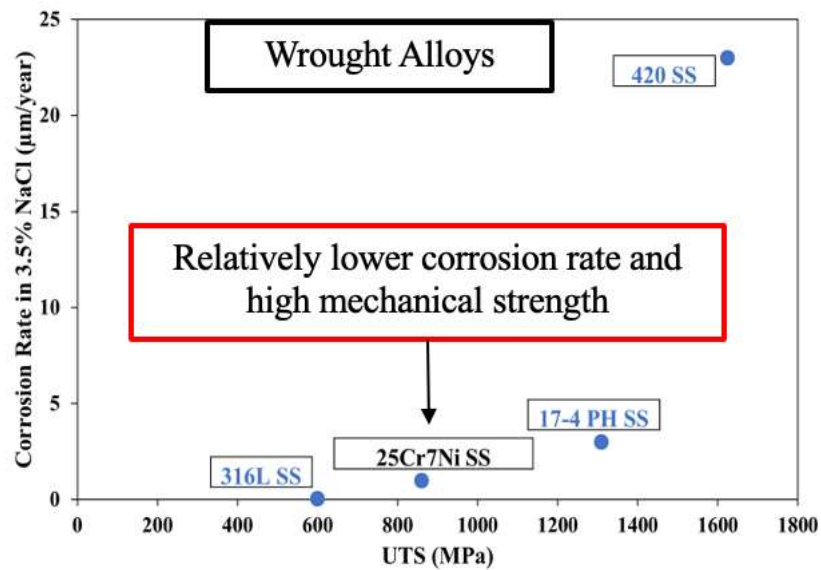


Figure 1.1. Variation of Corrosion rate as a function of UTS from wrought stainless steel alloys

Processing of 25Cr7Ni stainless steel through any means of unregulated hot forming operations or heat treatments have been shown to affect the phase balance and chemical composition [7]. Being a high alloyed stainless steel system, 25Cr7Ni stainless steel is quite sensitive to thermal cycles in terms of holding temperatures, holding times and cooling rates [8]. Slow cooling rates and prolonged exposure to temperatures between 500° C and 1000° C have been shown to initiate detrimental phases such as χ (BCC) and σ (tetragonal) phases. Their evolution has been identified to be as a result of decomposition of ferrite into austenite and the detrimental phases, directly affecting the 50 – 50 % ferrite and austenite phase balance. Additionally, these phases consume the Cr, Mo elements from the ferrite phase rendering a huge setback to the corrosion resistance of the 25Cr7Ni stainless steel system, as Cr, Mo are some of the primary passivating elements against corrosion. Coupled with their highly brittle nature,

detrimental phases destroy the robust combination of mechanical and corrosion properties offered by the 25Cr7Ni stainless steels [9–13].

Evolution of Detrimental Phases

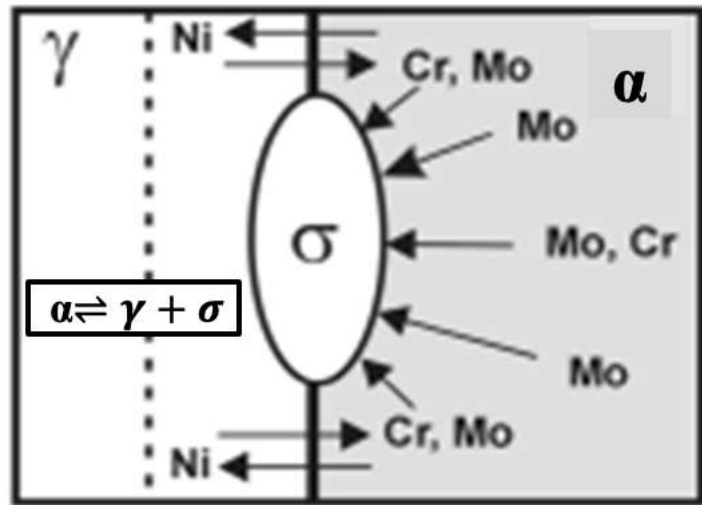


Figure 1.2. Schematic representation of detrimental phases

Along with the outlined limitations of processing 25Cr7Ni stainless steels under unregulated hot forming / heat treatment processes, in terms of inability to preserve the chemical composition, phase balance and to prevent the formation of the brittle detrimental phases, conventional fabrication also lacks the ability to cost effectively produce complex designs, design iterations and leads to longer lead times, increased warehousing cost for spares [14,15]. This has created a space for exploring alternate modes of processing 25Cr7Ni stainless steels.

The Laser-powder bed fusion (L-PBF) is a form of powder based additive manufacturing process where a metal alloy powder is processed into net-shape parts through laser energy. The fabrication is carried out under an inert atmosphere of Ar / N. The cycle time between powder melting / powder layer fusion / solidification is around 25 μm . This results in a very high cooling rate of around 10^7 k/s. Within the scope of processing 25Cr7Ni stainless steel, the high cooling rates of the L-PBF process help in preventing the formation of the detrimental phases and can preserve the chemical composition of the alloy system.

Additionally, the ability to fabricate near net shape parts with complex designs, on-demand, mitigating the lead times and warehousing costs, L-PBF offers significant value additions for processing 25Cr7Ni stainless steels [16–18].

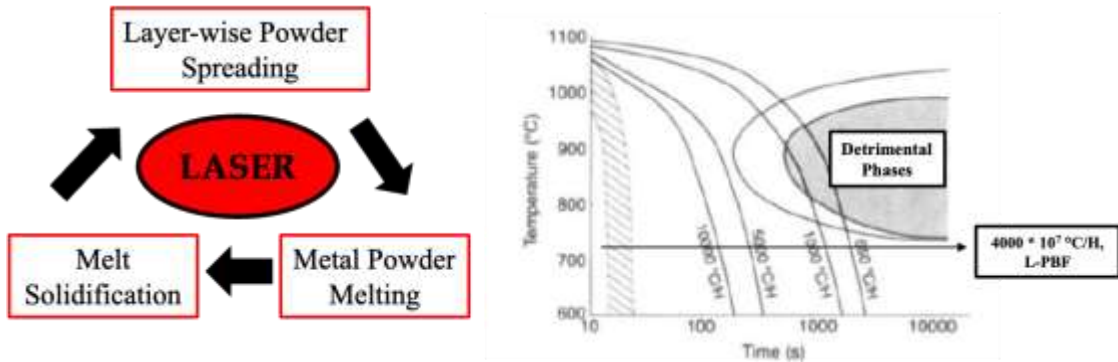


Figure 1.3. High cooling rates of L-PBF process responsible for prevention of detrimental phase evolution represented in Temperature – Time – Transformation diagram

As a novel process characterized by repeated additions of powder layers as small as 20 μm , cooling rates of $10^6 - 10^7$ k/s, involving feedstock of novel compositions that must be preserved throughout the process, the as-printed properties of the parts fabricated through L-PBF are pre-dominantly governed by four major aspects associated with the L-PBF process. The process parameters of the L-PBF process which include the laser power, scan speed, hatch spacing and the layer thickness. The powder attributes and chemical composition of the starting powder. The effect of post treatment such as ‘Hot Isostatic Pressing’ on the as-printed properties of the L-PBF fabricated parts. The effect of using N vs Ar as the inert atmosphere during L-PBF fabrication [10,16,19–22].

From Figure 1.4, in comparison to literature on L-PBF processing of conventional alloys such as 316L, 420, 17-4 PH steels, the literature on L-PBF processing of 25Cr7Ni stainless steel is significantly less [20,23–26]

Relative Number of Literature

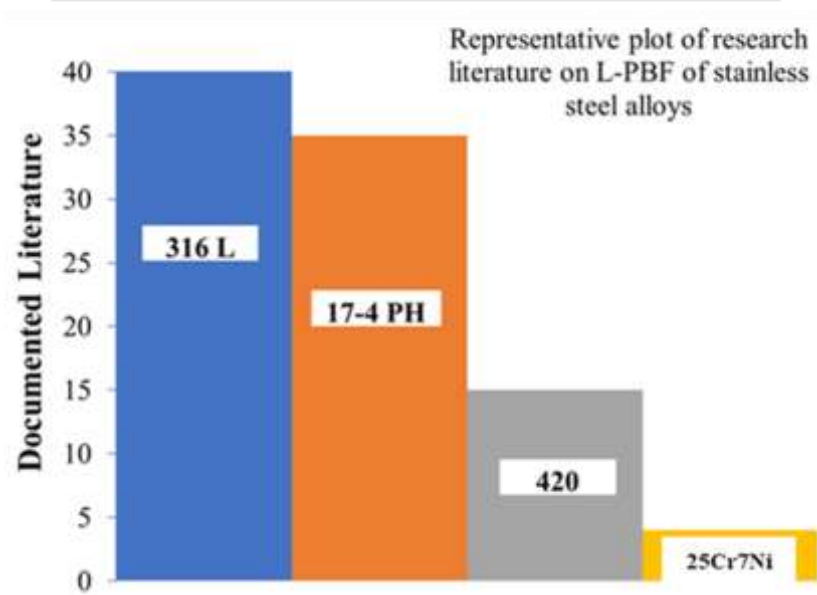


Figure 1.4. Relative number of literatures on different stainless steel alloys processed by L-PBF

Table 1.1. Collated literature on L-PBF processed 25Cr7Ni stainless steel

Author	Tensile strength (MPa)	Yield strength (MPa)	Elongation (%)	Relative Density (%)	Corrosion Properties	Significant Contribution
Singaneni et al.	-	-	-	90	-	Duplex microstructure achieved after heat treatment
Saeidi et al.	1321	1214	-	99.5	-	Microstructure ferritic in as-printed state
Raffeis et al.	1100 (Horizontal Orientation)	1035 (Horizontal Orientation)	8 (Horizontal Orientation)	99.95	-	Influence of part orientation/heat treatment

Table 1.1 evidence the research gap in characterizing the corrosion properties of the L-PBF fabricated 25Cr7Ni stainless steel. Also, among the reported studies, a lack of establishment of a comprehensive relationship between the process parameters, powder attributes, starting powder chemical composition, effect of HIP treatment and the effect of different fabrication atmospheres were present. This set the pace and scope of this current study, in primarily developing the ‘Process – Property – Microstructure’ relationship, by characterizing the physical, mechanical, microstructural and corrosion properties of test samples fabricated in varying process parameters, starting powder chemical composition, powder attributes, HIP treatment conditions and inert atmospheres. The study is spread across four primary chapters, with an additional two appendices.

Chapter 2 deals with the effect of varying the L-PBF process parameters while using a water atomized 25Cr7Ni stainless steel powder with an irregular powder morphology.

The fabrication was carried out in an Ar atmosphere. The physical, mechanical, corrosion properties of the as-printed L-PBF samples were compared against literature, a wrought – annealed, MIM, PM 25Cr7Ni stainless steel. The highlight of this work was the establishment of a correlation between a lower energy density – lack of fusion pores – poor mechanical / corrosion properties. The microstructure was also purely ferritic in the as-printed state at all energy densities.

Chapter 3 deals with the effect of HIP treatment at two different parameters on the properties of as-printed 25Cr7Ni stainless steels printed at a lower energy density (significant porosity/ferritic microstructure). The HIP treatment was carried out in an Ar atmosphere. The motivation for this work was to promote densification, duplex microstructure in the as-printed water atomized 25Cr7Ni stainless steel samples fabricated through L-PBF. The highlight of this work was the identification of the HIP parameter which promoted densification and austenite evolution rather than detrimental phases / deterioration of mechanical properties. The morphology of the evolved austenite in the HIP treated samples was also significantly different between the two HIP parameters.

Chapter 4 deals with the effect of powder attributes and chemical composition of two different batches of 25Cr7Ni stainless steel powders processed by L-PBF. One of the steel powders was water atomized with an irregular morphology and the other being gas atomized had a spherical morphology. The powders had a comparable PSD. The gas atomized powder had a chemical composition comparable to UNS32750 with the water atomized powder having a different composition in terms of lack of N. The L-PBF samples from both sets of powders were fabricated at the same process parameter under Ar atmosphere. The two highlight of this study was the spherical morphology of the gas atomized powder contributing to better densification – better mechanical / corrosion properties and the presence of N in the chemical composition of the gas atomized powder promoting the evolution of austenite in the as-printed condition. The properties were also compared with literature and with that of a wrought – annealed 25Cr7Ni stainless steel.

Chapter 5 deals with the effect of varying the processing atmospheres between Ar / N in fabricating a gas atomized 25Cr7Ni stainless steel powder through L-PBF. The samples were fabricated at the same L-PBF process parameters. The highlight of this study was the identification of ‘Nitrogen Porosity’ along with detrimental phases among samples fabricated in N atmosphere which impacted the mechanical and corrosion properties despite an entirely duplex microstructure in the as-printed state.

Appendix 1 dwells on the corrosion properties of a water atomized, gas atomized L-PBF fabricated 25Cr7Ni stainless steel along with a wrought – annealed 25Cr7Ni stainless steel, by correlating the powder attributes, chemical composition and evolved microstructure with the corrosion properties.

Appendix 2 deals with studying the effect of ‘in-situ alloying’ in a Ti-6Al-4V powder by mechanically mixing it with 5 wt% Si₃N₄ and processing through L-PBF. The study explored multiple energy densities in order to identify which set of the process parameters yielded an adequate distribution of nitrides within the alloy matrix upon L-PBF fabrication.

CHAPTER 2 INFLUENCE OF LASER-POWDER BED FUSION PROCESS PARAMETERS ON THE AS-PRINTED PROPERTIES OF LASER-POWDER BED FUSION FABRICATED 25Cr7Ni STAINLESS STEEL

Introduction

From the time of its invention laser-powder bed fusion (L-PBF) of metals has transitioned from a prototyping technology into a multi-billion dollar manufacturing revolution [1,2]. Design integration, reductions in lead times, ability to manufacture hard metals, novel properties of as-printed parts, defect rectification, recycling of the spent powders, ability to function with almost zero waste generation are some of the advantages additive manufacturing (L-PBF) offers over subtractive manufacturing [3]. These unique advantages are contributing to increased use of the L-PBF technology to manufacture complex shapes parts economically for various critical applications.

L-PBF fabrication of iron-based metal powders, especially conventional grade stainless steels such as ferritic steels, austenitic steels, martensitic steels, have been well established in both literature and on an industrial scale [2,4,5]. Dongdong Gu et al. [4] noted that the fabrication of steels through L-PBF is relatively easier in comparison to Al or Cu alloys. The Al or Cu alloys exhibit high thermal conductivity and lower laser absorption capacity, thus requiring a higher amount of laser energy density for formation of melt pool and fabrication of parts [4].

An ASTM standard 25Cr7Ni stainless steel is primarily a Fe-Cr-Ni alloy system with more than 24% of chromium, 6% of nickel denoted by UNS S32750 [6]. Conventional 25Cr7Ni stainless steel is characterized by a two-phase microstructure consisting of approximately 30 - 70% ferrite and 70 - 30% austenite. This unique two-phase microstructure results in high strength and corrosion resistance, leading to a wide range of applications especially in the petrochemical industry [6]. The evolution of the bi-phase microstructure in 25Cr7Ni stainless steel is influenced by the composition of the constitutional elements in the steel, wherein elements such as chromium, molybdenum and silicon are ferrite phase stabilizers and nickel, nitrogen are austenite phase stabilizers [5].

The corrosion properties of 25Cr7Ni alloys are imparted through chromium, molybdenum oxide layer [7]. Nickel primarily contributes to the corrosion resistance thorough its austenite phase stabilization and elemental partitioning between ferrite/austenite phases [7].

Very few studies have been conducted and reported on the L-PBF fabrication of duplex stainless steels [1,3,8,9] studied the evolution of microstructure and mechanical properties of L-PBF processed 23Cr5Ni and 25Cr5Ni steels respectively. The findings identified ferrite as the major phase in as-printed samples and duplex structure in heat

treated samples. The studies also reported as-printed samples demonstrating very high strength and low elongation compared to heat treated samples. Davidson et al. [3] studied the microstructure evolution in L-PBF fabrication of gas atomized 25Cr7Ni powders. The study identified ferrite as the major phase in the as printed samples. The ferrite grains were elongated in the build direction with austenite precipitation along the grain boundaries or as Widmanstätten laths. In another study Saeidi et al. [9] also reported identifying ferrite as major phase in the microstructure of L-PBF processing of gas atomized 25Cr7Ni.

The mode of powder atomization (water / gas / plasma) contributes to the overall cost of the starting 25Cr7Ni stainless steel powder with water atomization being the cheapest option [10]. Water atomization typically results in an irregular powder morphology, with gas and plasma atomization resulting in predominantly a spherical morphology. All the studies reported in literature on L-PBF of 25Cr7Ni were carried out using expensive gas atomized powders. There were also no studies carried out on the characterization of the corrosion properties of L-PBF fabricated 25Cr7Ni stainless steel. The present study is aimed at addressing this topic. The study is focused on evaluating the mechanical, corrosion and microstructure properties of L-PBF fabricated water atomized 25Cr7Ni stainless. The effect of different process parameters, and their influence on the as-printed physical, mechanical and corrosion resistant properties were characterized. The findings from the study will assist in understanding the feasibility of using lower cost water atomized 25Cr7Ni powder for fabricating parts via L-PBF technology. The findings will also provide an understanding of the effect of L-PBF process parameters on the mechanical and corrosion properties of the printed samples starting from water atomized 25Cr7Ni powders.

Methodology

Water atomized 25Cr7Ni stainless steel with a D_{50} of $35\mu\text{m}$ was used in this study as the starting powder. The composition of the starting powder is shown in **Table: 2.1**. The starting powder in the study had no nitrogen content and lower Mn and Mo content compared to UNS 32750 specification. The Mn and Mo content in the starting powder was 0.1 and 1.3% compared to the manganese content (0.9 %) and molybdenum content (3.88 %) in UNS 32750 stainless steel. The Si content (1.79 %) in the starting powder was higher than the silicon content (0.5 %) in UNS 32750. The tungsten content in the starting powder (0.8%) was also higher than the ASTM standard value (0.01%). Both these elements aid in passivation against corrosion [7]. The SEM micrograph of the starting powder **Figure 2.1** shows the irregular morphology of water atomized 25Cr7Ni powders. The pycnometer density of the powder was measured to be $7.68 \pm 0.02 \text{ g/cm}^3$. This value was used to calculate the relative density of the L-PBF as-printed samples, as a ratio of their Archimedes density value to pycnometer density. The powder had an apparent density of 3.0 g/cm^3 and a tap density of 3.4 g/cm^3 .

A Concept Laser Mlab cusing system, equipped with Yb fibre laser was used for the L-PBF process. The laser source had a maximum power of 100 W and the laser beam spot diameter was $50 \mu\text{m}$. The L-PBF process was used to fabricate flat E8M ASTM standard tensile samples with a gauge length of 74.5 mm, gauge width of 6.2 mm, a thickness of 3 mm. The samples were fabricated in the horizontal orientation, with the gauge length parallel to the scan direction plane (XY). Argon gas was constantly flooded into the build chamber and vented, to limit the oxygen concentration to less

than 0.2% throughout the fabrication process. The as-printed part properties are mainly influenced by laser power **P**, laser scan speed **v**, and the distance between adjacent laser scan track (hatch spacing) **h** and the thickness of the deposited powder layer **t**. These influences are quantified into a single significant value called the energy density **E** given by Equation (1):

$$E = \frac{P}{v * h * t} \quad (1)$$

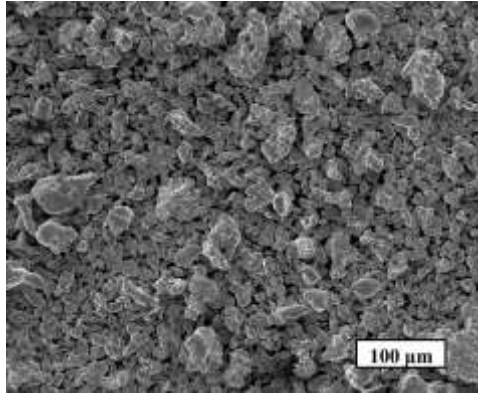


Figure 2.1 SEM micrograph of the starting powder used in the study

Table 2.1: Comparison of starting powder composition

Element	Amount (%)
Cr	25
Ni	6.2
Mo	1.3
Cu	2
Si	1.8
W	0.8
Mn	0.1
N	-
C	0.02
P	0.015
S	0.009
Fe	Balance

The energy density **E** has units J/mm^3 . The process parameters used in the present study are summarized in **Table 2.2**. The laser power at 90 W and layer thickness 20 μm were held as constant. All the samples were printed using continuous scan line strategy with a hatch angle of 90° (-45° and +45°).

The density of as-printed tensile bars was measured based on the Archimedes principle as per the ASTM 962-17 standard, using Mettler Toledo XS104 analytical balance. A total of five samples for each energy density were used for tensile testing and hardness measurement. The tensile properties of the as-printed samples were measured at a strain rate of $0.001 s^{-1}$ with an MTS Exceed hydraulic dual-column tensile testing system equipped with a 100 kN load cell. The hardness of the tensile bar samples was measured with a Rockwell ‘C’ hardness testing apparatus at 150 Kgf load. All the hardness

measurements were recorded on the scan surface (XY) of the tensile samples. A total of 5 hardness readings for each sample were recorded.

Table 2.2: Process parameters of L-PBF used in this study

S. no	Processing Conditions				
	Laser power, P (W)	Scan speed, v (mm/s)	Scan spacing, h (μm)	Layer thickness, t (μm)	Energy density (J/mm^3)
1	90	800	150	20	38
2	90	800	120	20	47
3	90	800	105	20	54
4	90	600	150	20	50
5	90	600	120	20	63

The corrosion properties of the as printed samples were evaluated using linear sweep voltammetry (LSV). As-printed L-PBF samples of all the energy densities, were polished along the scan direction (XY) for the LSV measurements. The surfaces were ground using SiC paper with grit sizes varying from 120 to 1200 and polished with 9 μm and 1 μm diamond suspensions. The LSV measurements were conducted in a 3.5% NaCl solution at room temperature using a Metrohm Autolab PGSTATION 100N system. The L-PBF samples were used as a working electrode along over an area of 0.2 mm^2 , with a platinum counter electrode and an Ag/AgCl reference electrode. For each trial, the open circuit potential (E_{oc}) was recorded, and each measurement began from this value. The PGSTATION system recorded the corrosion current. The experiments were conducted in the potential range between -1V and 2V from E_{oc} at a forward scan rate of 0.01 mVs^{-1} with a current density limit of 10 $\text{mA}\cdot\text{cm}^{-2}$. The corrosion current, polarization resistance, and breakdown potentials were recorded. Tafel plots were constructed with obtained corrosion current and the potentials. The corrosion rates were also calculated. Optical micrographs of the surfaces subjected to the corrosion testing were obtained before and after the corrosion tests.

The oxygen, carbon, nitrogen, sulphur and hydrogen composition of the as-printed L-PBF sample printed at 63 J/mm^3 was also recorded using LECO elemental analyser. The x-ray diffraction (XRD) was carried out using a Discovery D8 diffractometer (BRUKER, AXS, Inc., USA) with a Cu-K α radiation $\lambda = 1.54 \text{ \AA}$, 45kV, 40 mA on the water atomized 25Cr7Ni stainless steel powder, as-printed L-PBF samples, and a wrought – annealed 25Cr7Ni stainless steel sample. The evolved intensity peaks were compared against JCPDS cards corresponding to the most probable phases to evolve, such as α -ferrite and γ -austenite.

For metallographic evaluation, the samples along their build direction were mechanically ground through grit sizes of 60, 120, 400, 800, and polished with 9 μm

and 1 μm diamond solutions. Electro-etching was done using 40% KOH solution at 4.5V DC (Direct Current) for a time span of around 5 seconds. The etched surfaces were characterized through an optical microscope. The microstructures were also characterized at higher magnifications using a TESCAN scanning electron microscope at an electron accelerating voltage of 10 kV. Electron backscattered diffraction (EBSD) was carried out in the Field Emission - SEM system. The samples for EBSD were mechanically ground and polished through 9 μm , 1 μm , and 0.5 μm diamond solutions. This was followed by vibratory polishing for four hours in colloidal silica suspension. The EBSD measurements were carried out with a step size of 2 μm , in an area of 240 μm x 240 μm . A strong confidence index of more than 0.5 was consistently maintained. APEX software was used for the data-acquisition and post-processing.

Results & Discussion

The variation of obtained density of the as printed samples with energy density is shown in **Figure 2.2**. As seen from **Figure 2.2**, the Archimedes density of as-printed L-PBF samples increased from $7.11 \pm 0.01 \text{ g/cm}^3$ at an energy density of 38 J/mm^3 to $7.52 \pm 0.01 \text{ g/cm}^3$ at 63 J/mm^3 . The relative densities of as-printed samples also increased from $92\% \pm 0.1\%$ to $97.6\% \pm 0.2\%$ with increase in energy density from 38 J/mm^3 to 63 J/mm^3 . The increase in the sample density with increase in energy density is expected due to the complete melting of metal powder and fusion of the metal powder at higher temperatures [2,5]. The highest relative density of the L-PBF fabricated parts in this study was around $97.9\% \pm 0.1\%$. Prior study carried out by [3] with L-PBF of gas atomized 25Cr7Ni achieved a density of only 92.7 and 92.6% when processed at high energy densities of 134 and 141 J/mm^3 respectively. Another study carried out by [9] reported achieving 99.5% density in L-PBF of gas atomized 25Cr7Ni when processed at high energy density of 127 J/mm^3 . It is very interesting to note that a very high density of 97.9% was obtained in the current study at a very low energy density of 63 J/mm^3 . The result is significant as the high density was obtained using water atomized 25Cr7Ni stainless steel which has irregular morphology, inferior flowability and low bulk density. Several studies have reported achieving high densities with L-PBF processing gas atomized powders compared to water atomized powders [2]. The results indicate, a potential to achieve higher densities above 99% by increasing the energy density above 63 J/mm^3 . Using a powder of spherical morphology and increasing the energy density can be explored to achieve over 99% relative density of as-printed samples in future fabrications.

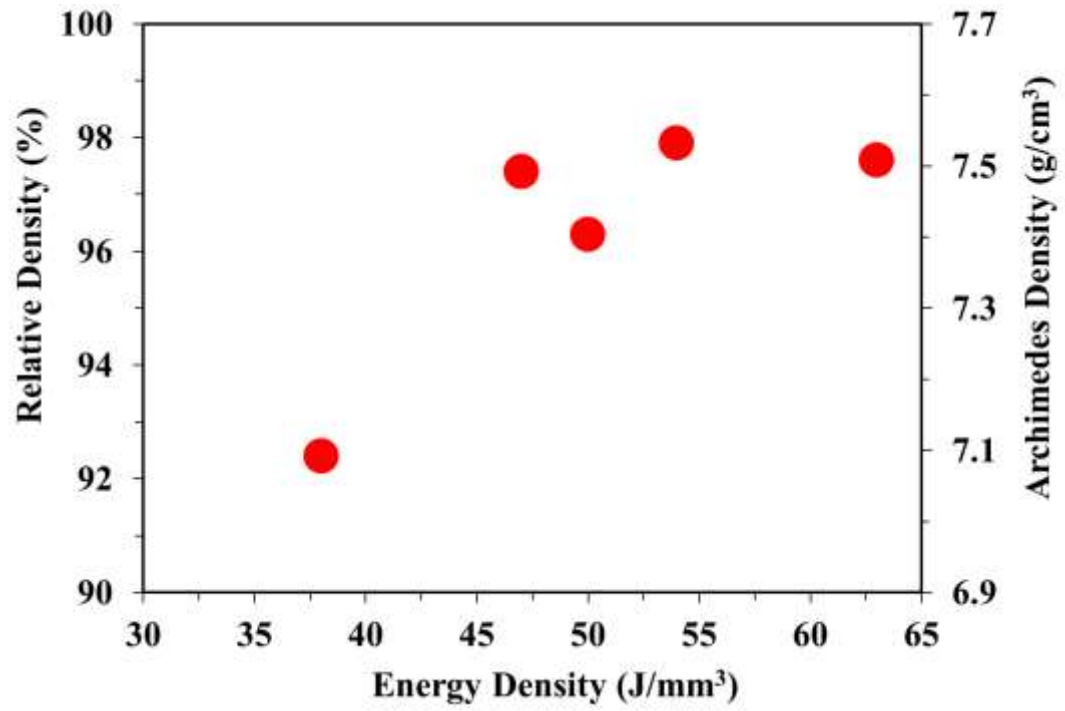


Figure 2.2 Variation of as print sample density with energy density

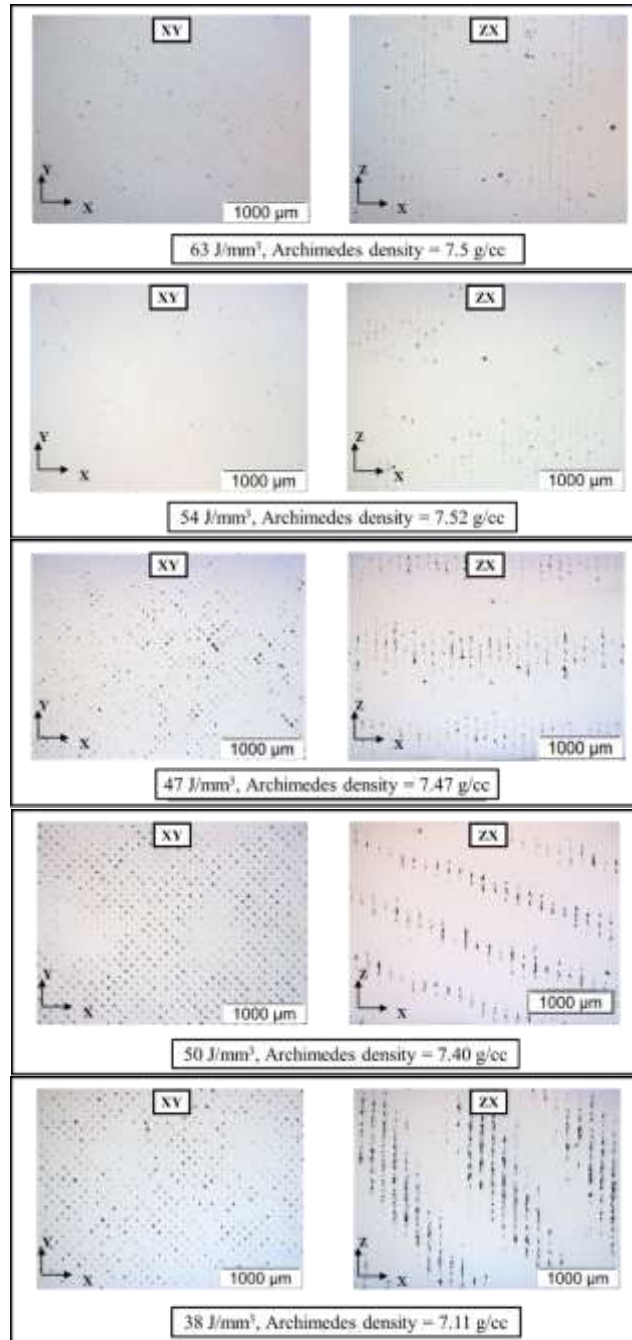


Figure 2.3 Light micrographs of as-printed L-PBF samples in (left) build direction (BD) (right) scan direction (SD) fabricated at different energy densities

Figure 2.3 shows representative optical micrographs of the polished surfaces of as-printed samples along the scan (XY) and build (ZX) directions. A qualitative reduction in overall porosity and size with an increase in the energy density was observed. The number and distribution of pores in the samples printed at lower energy density are markedly high compared to the sample printed at the highest energy density indicating adequate fusion and densification of the powder layers in the L-PBF samples at higher energy densities. Anisotropy of pores between the scan and build direction was also

observed. The porosity and the size of pores decreased from around 4.7 % and $70 \pm 10 \mu\text{m}$ @ 38 J/mm^3 to less than 0.8 % and $10 \pm 2 \mu\text{m}$ @ 63 J/mm^3 .

At lower energy densities, in the scan direction, alignment of pores in a ‘crisscross’ pattern is visible. This pattern co-relates with the laser hatching patterns (-45° & $+45^\circ$) employed in the L-PBF process. These pores thus indicate a lack of scan track overlap (large hatch spacing) at lower energy densities.

The mechanical properties of as-printed samples for the different energy densities are tabulated in **Table 2.3**.

Table 2.3: Mechanical properties of L-PBF water atomized 25Cr7Ni stainless steel

Energy Density (J/mm^3)	Relative density (%)	UTS (MPa)	El (%)	Yield Strength (Mpa)	HRC
63	97.6 ± 0.2	1040 ± 15	11 ± 2.2	980 ± 13	26 ± 0.5
54	97.9 ± 0.1	1050 ± 2	11 ± 1.1	990 ± 2	30 ± 0.2
50	96.3 ± 0.1	940 ± 20	9 ± 1.0	865 ± 20	26 ± 0.4
47	97.4 ± 0.1	1000 ± 15	12 ± 0.6	935 ± 17	26 ± 0.8
38	92.4 ± 0.1	840 ± 20	8 ± 0.8	730 ± 25	18 ± 0.6

The highest ultimate tensile strength of $1050 \pm 2 \text{ MPa}$ with $990 \pm 13 \text{ MPa}$ yield stress and $11 \pm 1.1 \%$ elongation were recorded at 54 J/mm^3 . The UTS and yield strength was higher than wrought ($860 \pm 30 \text{ MPa}$ & $580 \pm 9 \text{ MPa}$), metal injection moulded (730 MPa & 435 MPa), powder metallurgically sintered (900 MPa & 550 MPa) 25Cr7Ni stainless steel samples and comparable to the available literature on L-PBF as-printed 25Cr7Ni stainless steel (1100 MPa & 1035 MPa) [1,8,11]. The elongation of the as-printed sample at 63 J/mm^3 was higher compared to the 8% elongation reported in a prior study [8]. The as-printed samples exhibit comparable hardness to metal injection moulded samples, but lower hardness than fully dense wrought samples, as seen in **Table 2.3**.

The L-PBF samples exhibited higher tensile strength than wrought, MIM, PM 25Cr7Ni stainless steels, despite the starting powder having 3 times lower amounts of Molybdenum and no nitrogen in comparison to an ASTM standard 25Cr7Ni stainless steel. Both these elements have a precipitation hardening effect (Mo) & solid solution strengthening effect (N) on stainless steel [12]. L-PBF technology involves melting of powders followed by rapid cooling and solidification. The process results in formation of high dislocation density in the printed samples. The observed high strength is attributed to the high dislocation density of the samples [1,8].

Figure 2.4 (a) shows the influence of as-printed part density on the ultimate tensile strength, **Figure 2.4(b)** shows the variation of yield strength with density and **Figure**

4(c) captures the variation in elongation with the density of as-printed samples. As seen in Figure 4, all these parameters increased with increase in density. The samples processed at high energy densities displayed high final density **Figure 2.2**. A densification of over 98% relative density of printed parts resulted in reduction in the size and density of pores. Hence, the ultimate strength of the as-printed samples increases from 840 MPa at 38 J/mm^3 energy density to 1040 MPa at 63 J/mm^3 energy density. Correspondingly, the percentage elongation of the as-printed samples increased from $8 \pm 0.8 \%$ elongation at 38 J/mm^3 to $11 \pm 2\%$ elongation at 63 J/mm^3 . The voids in the as-printed samples of lower densities act as micro cracks within the sample and produce numerous stress concentration sites leading to premature failure and lower tensile strengths [30]. The voids in the as-printed samples with lower densities also contributed to lower hardness.

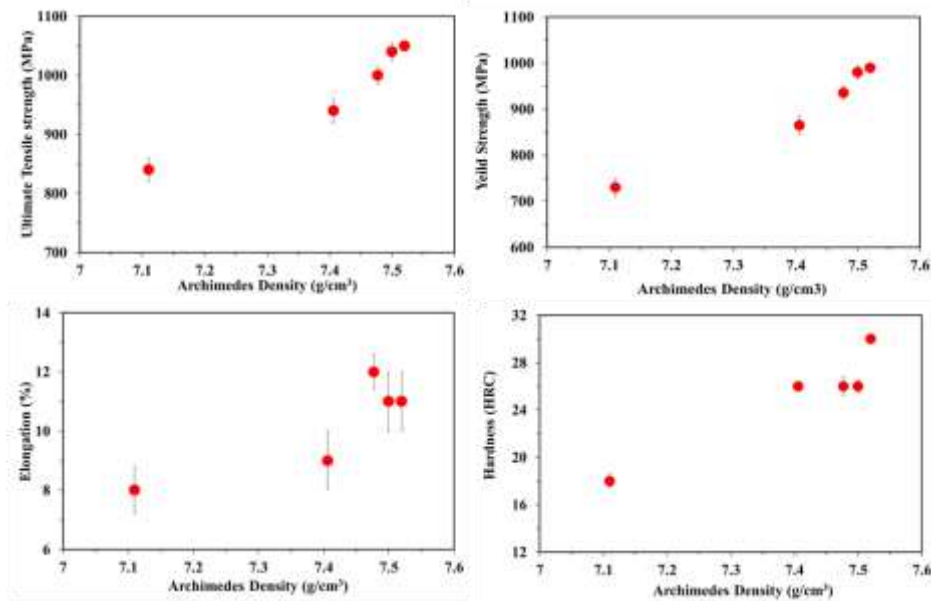


Figure 2.4 Variation of (a) ultimate tensile strength (b) yield strength (c) elongation (d) hardness as a function of the density of as-printed 25Cr7Ni stainless steel of novel composition samples

Figure 2.5 shows XRD patterns of wrought 25Cr7Ni stainless steel sample, water atomized 25Cr7Ni stainless steel powder along with as-printed L-PBF water atomized 25Cr7Ni stainless steel samples. The starting powder and the as-printed L-PBF samples were composed of ferrite phase ($2\theta = 44^\circ, 64^\circ, 81^\circ$) with no traces of peaks corresponding to the austenite phase. In comparison, the recorded XRD pattern of a wrought 25Cr7Ni stainless steel sample showed significant peaks of austenite ($2\theta = 43^\circ, 50^\circ, 74^\circ$) besides ferrite phases. The lack of even trace amounts of austenite and/or secondary phases in the starting powder can be reasoned due to high cooling rates in water atomization and lack of nitrogen in the starting powder.

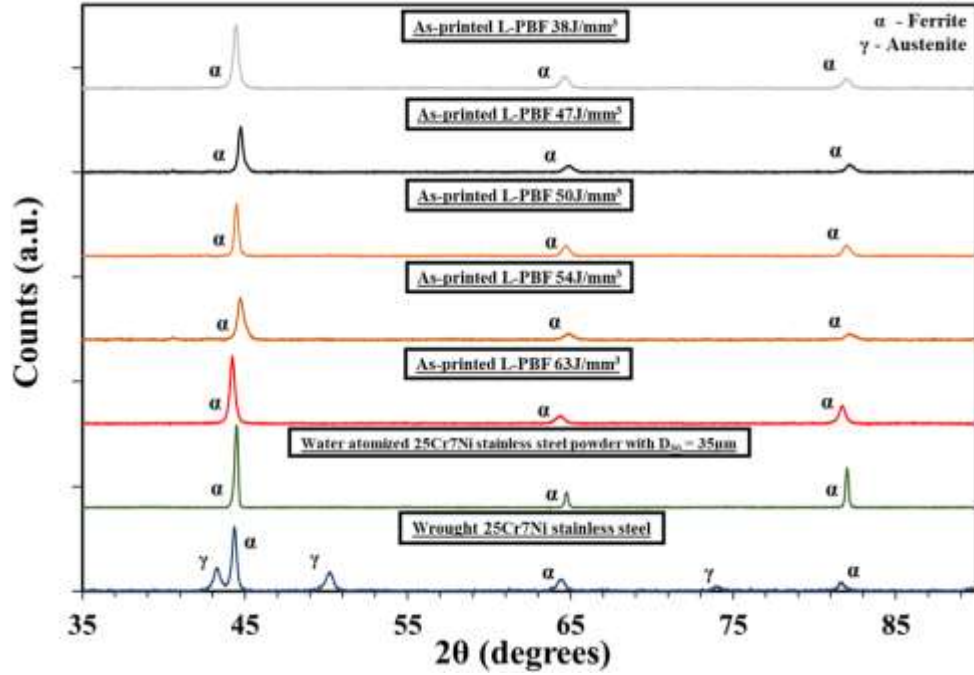


Figure 2.5 XRD pattern of the wrought 25Cr7Ni stainless steel, starting 25Cr7Ni stainless steel powder of novel composition, L-PBF as-printed 25Cr7Ni stainless steel of novel composition sample

The amount of ferrite and austenite in the as-printed L-PBF sample was estimated using the Schaeffler diagram based on the Cr_{eq}/Ni_{eq} in the precursor powder composition [12]. The chromium and nickel equivalent estimations are calculated through the equations (2), (3) given below,

$$Cr_{eq} = \%Cr + \%Mo + 0.5\%Nb + 1.5\%Si \quad (2)$$

$$Ni_{eq} = \%Ni + 30\%C + 0.5\%Mn \quad (3)$$

From the above equations the chromium and nickel equivalents were calculated to be 29.8 and 7.9 respectively. The chromium and nickel equivalent were used to estimate a microstructure with more than 90% ferrite, showing a good correlation with the xrd analysis of the starting powder and the as-printed L-PBF sample. Prior research studies have also reported ferrite as the major phase in L-PBF printed 25Cr7Ni samples [3,9].

The ferrite peaks observed in the L-PBF as-printed samples were slightly broadened compared to the corresponding peaks in the starting powder. Prior studies attribute the increase in peak width in a diffraction profile to the micro strains in the crystal lattice [34-35]. Correlating this result with the present work, the high thermal cycles involved in the L-PBF process results in high dislocation density within the as-printed samples, like the observations made in [1]. Such high dislocations density could lead to higher lattice strains leading to peak broadening in the L-PBF sample relative to the stainless-steel powder.

The optical micrographs of the as-printed samples processed at different energy densities along the build direction is shown in **Figure 2.6**. The electro-etching primarily

etches the ferrite phase and leaves the austenite phase un-etched [13]. The micrographs which were captured along the build direction, revealed complete etching across the entire region in samples of all energy densities, indicating a completely ferrite phase. This shows good correlation with the XRD analysis. The melt pool in the micrographs is indicated by dotted lines.

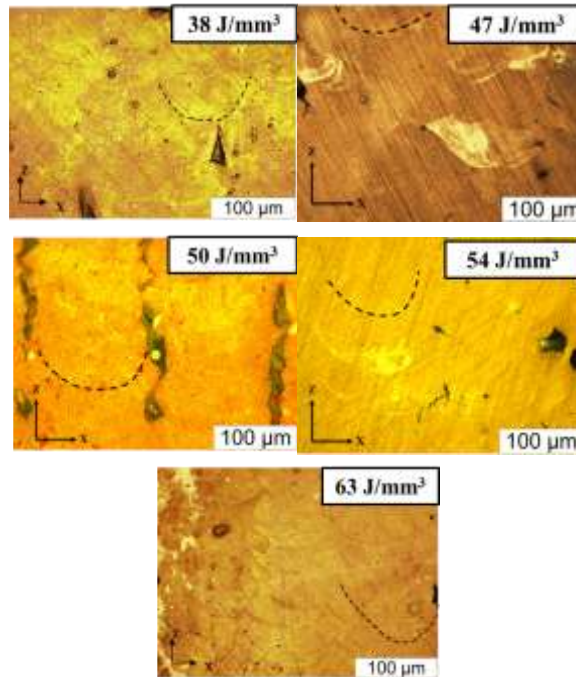


Figure 2.6 Optical micrographs of electro-etched as-printed L-PBF samples in the build direction printed at all the energy densities, the dotted lines indicating a melt-pool

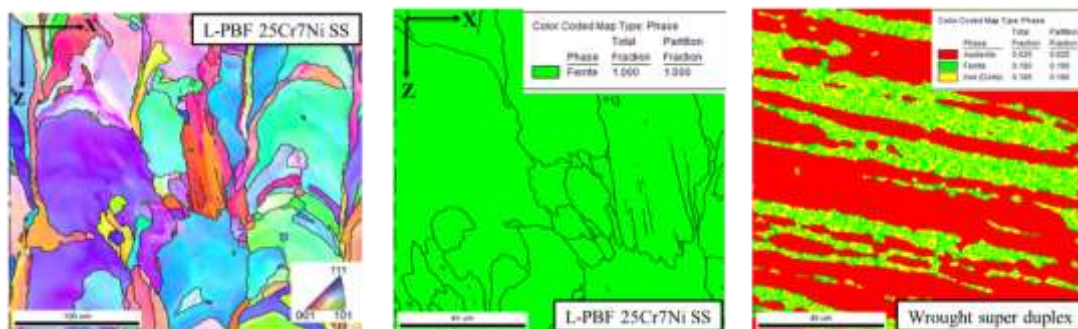


Figure 2.7 EBSD maps of (left) texture, (middle) phases for as-printed L-PBF samples @ 63J/mm³ along the build direction (right) phases for wrought 25Cr7Ni stainless steel samples

Extending the phase analysis, EBSD phase maps of an as-printed L-PBF 25Cr7Ni stainless steel along the building direction and a wrought 25Cr7Ni stainless steel in the rolling direction are represented in the **Figure 2.7**. As it can be seen from the phase maps, the wrought 25Cr7Ni stainless steel is composed of more than 60 % of austenite, around 40% ferrite. In comparison the recorded phase map of the as-printed L-PBF 25Cr7Ni stainless sample was composed of 100% of ferrite completely devoid of austenite phases. The average grain sizes of the water atomized as-printed L-PBF 25Cr7Ni stainless steel along the build direction was recorded to be 50 µm. From the

EBSD texture map of 63 J/mm³, we can see that the grains have coarsened across multiples powder layers along ((111), building direction - Z) indicating adequate re-melting and fusion.

The cathodic and anodic polarization curve extracted from the LSV experiments are potted in Figure 8. These curves were used to determine the corrosion current I_{corr} and breakdown potential along with cathode and anode slope by Tafel method. This was followed by calculation of polarization resistance R_p and corrosion rate CR based on the formulas given below [14] in Equations 4, 5.

$$R_p = \left(\frac{1}{I_{corr}} \right) * \frac{\beta_a * \beta_c}{\beta_a + \beta_c} \quad (4)$$

where the Tafel constants β_a, β_c represent the anodic and cathodic slopes in the plot. Similarly,

$$CR = \frac{I_{corr} * k * EW}{\rho A} \quad (5)$$

where ρ is the Archimedes density of the material, k is a constant 3.272 m/year and EW is the equivalent weight of the material 23.11 g.

The corrosion properties of as-printed samples extrapolated from the Tafel plots (Figure 8) and calculated based on Equations 4 & 5 are summarized in **Table 2.4**.

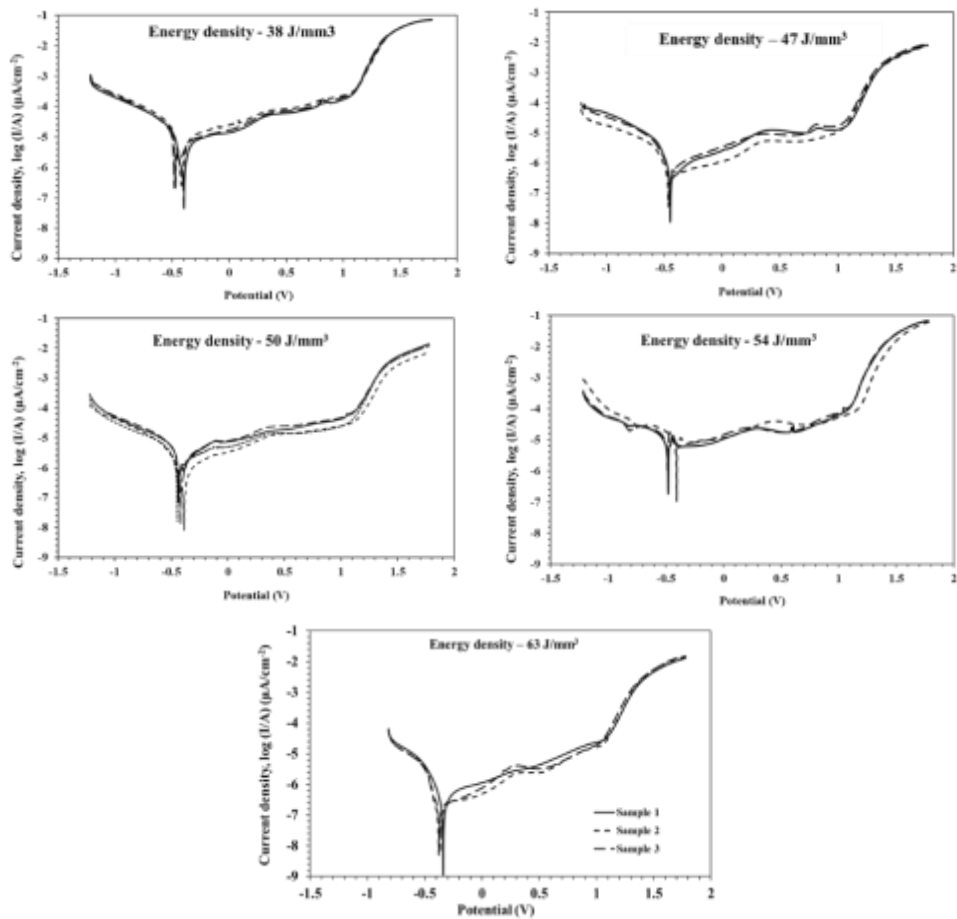


Figure 2.8 Linear sweep voltammetry (LSV) curves of three as-printed L-PBF 25Cr7Ni stainless steel samples at all energy densities in aerated aqueous solution containing 3.5 wt.% of NaCl

As seen in **Table 2.4**, the as-printed samples fabricated at 63 J/mm^3 displayed the least corrosion rate of $5.7 \pm 2 \text{ } \mu\text{m/year}$ and the highest polarization resistance (which is resistance of a metal to oxidation in the presence of an external potential source) among the as-printed L-PBF samples. The polarization resistance gradually decreased, and the corrosion rate increased with decrease in laser energy density from 63 J/mm^3 to 38 J/mm^3 . As-printed 25Cr7Ni stainless steel samples fabricated at 38 J/mm^3 laser energy density had the highest corrosion rate and the least polarization resistance indicating low corrosion resistance.

Table 2.4: Variation of corrosion properties of as-printed samples with energy density

Specimen	Relative Density (%)	Corrosion current, I_{corr} ($\mu\text{A}/\text{cm}^2$)	Corrosion potential, E_{corr} (V)	Breakdown potential, E_b (V)	Polarization resistance, R_p (Ω/cm^2) $\times 10^5$	Corrosion rate ($\mu\text{m}/\text{year}$)
63 J/mm ³	98 \pm 0.2	0.1 \pm 0.04	-0.36 \pm 0.02	1.02 \pm 0.01	4.62 \pm 0.54	5.7 \pm 2
54 J/mm ³	97.9 \pm 0.1	0.29 \pm 0.06	-0.45 \pm 0.03	1.01 \pm 0.02	1.44 \pm 0.2	15 \pm 3
50 J/mm ³	96.3 \pm 0.1	0.7 \pm 0.2	-0.43 \pm 0.02	1.07 \pm 0.02	0.56 \pm 0.28	36.8 \pm 10
47 J/mm ³	97.4 \pm 0.1	0.44 \pm 0.1	-0.45 \pm 0.01	1.05 \pm 0.01	1.7 \pm 0.1	22.6 \pm 5
38 J/mm ³	92.4 \pm 0.1	2.26 \pm 0.7	-0.42 \pm 0.02	1.09 \pm 0.00	0.27 \pm 0.05	124 \pm 38
Wrought 25Cr7Ni	100	0.10 \pm 0.01	-0.28 \pm 0.05	1.01 \pm 0.05	4.47 \pm 0.37	5.01 \pm 0.7

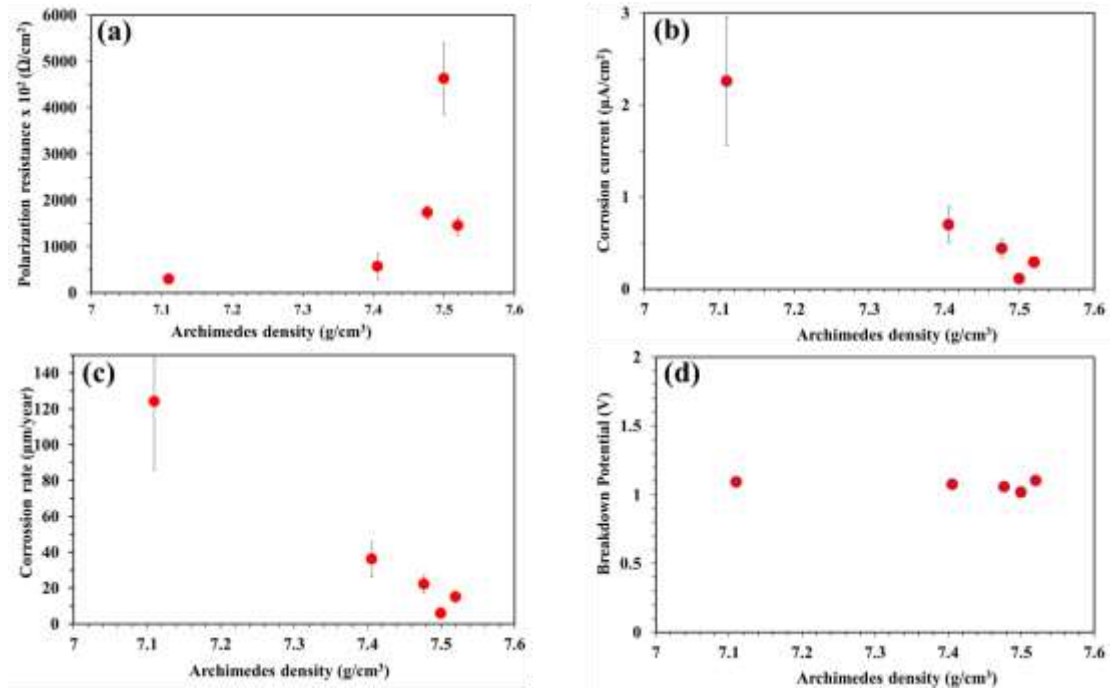


Figure 2.9 Variation of (a) polarization resistance, (b) corrosion current, (c) corrosion rate, (d) breakdown potential as a function of Archimedes density of as-printed L-PBF 25Cr7Ni stainless steel

To further understand the underlying trend behind the marked variation of corrosion properties of as-printed stainless steel samples, the corrosion current, polarization resistance, the corrosion rate and the breakdown potential were plotted as a function of part density **Figure 2.9**. The plots clearly depict an increase in polarization and corrosion resistance with increasing density. The results indicate a strong dependency of the corrosion properties on the porosity of the samples.

The breakdown potential was constant at around $1.05 \pm 0.01\text{V}$ across all the part densities. The observed non-smooth nature of the cathodic arm of the Tafel plots in

Figure 2.8 is due to the formation of ‘corrosion pits’ within the pores of the as-printed L-PBF samples [15,16]. Prior study indicated that the pores in the as-printed samples lead to stagnation of corrosive solutions at these locations intensifying the effect of pitting corrosion [2]. Processing at high energy density results in reduction of pores in the samples contributing to enhanced pitting corrosion resistance. The micrographs of samples before and after corrosion testing shown in **Figure 2.10** confirms lower localized pitting corrosion of samples with low pore size and density. The SEM micrograph of a L-PBF sample printed at 63 J/mm^3 , before and after corrosion testing along the scan direction is shown Figure 11. Evolution of corrosion pits spaced $120 \mu\text{m}$, similar to the hatch spacing of the 63 J/mm^3 energy density was observed in the micrographs. Enlargement of pores between before and after corrosion micrographs corroborates the previous assertion that porosity in the samples acted as sites for pitting corrosion.

The corrosion rate of L-PBF samples ($5.7 \pm 2 \mu\text{m/year}$) in the present study was comparable to the wrought 25Cr7Ni stainless steel (corrosion rate – $5.01 \pm 0.7 \mu\text{m/year}$). The result is very interesting as only ferrite phase was observed in the L-PBF printed samples. Pitting corrosion in 25Cr7Ni stainless steels are predominantly an intragranular corrosion phenomenon. The corrosion initiates at the sites where the chromium content is relatively lower such as at the grain boundaries wherein chromium is precipitated as carbides and nitrides [8]. This phenomenon which is referred to as ‘sensitization’, results in areas of partial chromium oxide layer passivation subsequent electrochemical corrosion. The composition of the starting powder had only trace amounts of nitrogen and the fabrication was conducted in an argon gas atmosphere ensuring relatively lower carbon inclusion. The carbon and nitrogen in the as-printed samples was $0.0183 \pm 0.002 \%$ and $0.00048 \pm 0.001 \%$, respectively. These factors could have possibly ensured lower amounts of nitrides or carbides of chromium to be precipitated along the grain boundaries. The EBSD phase maps of as-printed L-PBF samples in the build direction ZX seen in **Figure 2.7** (middle) also identified no significant carbides/nitrides. The lower Molybdenum content in starting powder assists in eliminating the formation of detrimental σ phase (which deplete Chromium from the composition) in the printed sample. The absence of σ phase was also confirmed by the EBSD analysis. Thus, lower ‘sensitization’ and lack of σ phase, could be the possible reasons for the comparable corrosion rates of the as-printed L-PBF 25Cr7Ni stainless steel samples in comparison to the wrought 25Cr7Ni stainless steel samples

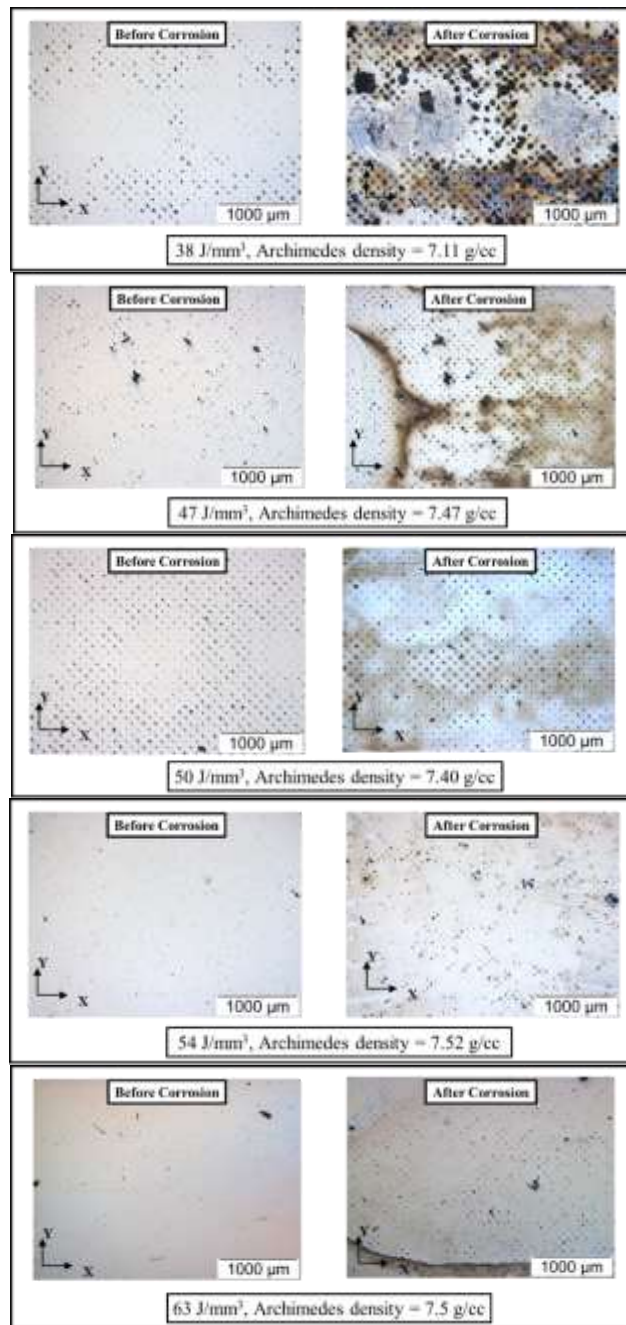


Figure 2.10 Light micrographs of as-printed L-PBF specimen stainless steel samples for varying energy densities in the scan direction XY plane (left) before corrosion testing (right) after corrosion testing

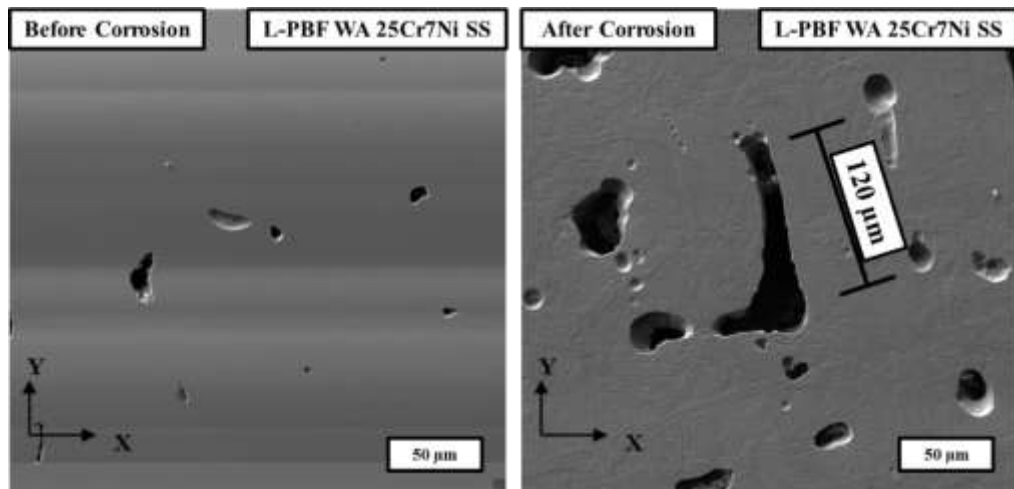


Figure 2.11 SEM micrographs of L-PBF WA 25Cr7Ni SS sample @ 63 J/mm³ (Left) before corrosion testing (Right) after corrosion testing

Conclusions

The effects L-PBF process parameters on mechanical, physical and the corrosion properties of the water atomized 25Cr7Ni stainless steel fabricated via L-PBF were examined in this study. The final density, mechanical and corrosion properties of the as printed samples increased with increase in energy density. A maximum of 98% relative density was obtained in samples processed at 54 and 63 J/mm³. Ferrite was observed as the major phase in the microstructure of the printed samples. The maximum UTS and yield strength of the printed samples in the study was higher than wrought, metal injection molded, powder metallurgically sintered 25Cr7Ni stainless steel samples and comparable to the available literature on L-PBF as-printed 25Cr7Ni stainless steel. The high UTS and yield strength is attribution to the formation of high dislocation density in the as-printed samples. The corrosion rate of L-PBF samples in the present study was comparable to the wrought 25Cr7Ni stainless steel despite displaying only ferrite phase. The high corrosion resistance is attributed to the absence of chromium carbide/nitrides as well as sigma phase in the printed samples.

CHAPTER 3 INFLUENCE OF HOT ISOSTATIC PRESSING ON THE PROPERTIES OF LASER-POWDER BED FUSION FABRICATED 25CR7NI STAINLESS STEEL

Introduction

The value addition for the 25Cr7Ni stainless steel in terms of its strength, toughness and corrosion resistance stems from its combination of ferritic and austenitic microstructure[1]. Conventional fabrication of 25Cr7Ni stainless steels under higher processing temperature and slower cooling rates are susceptible to evolution of detrimental phases / precipitates such as σ , χ , carbides and nitrides, which have a deleterious effect on the final properties[2-5]. L-PBF fabrication through its higher cooling rates in the order of 10 K/s, effectively suppresses the formation of the above mentioned secondary phases in 22Cr5Ni stainless steels. However, the inherently high cooling rates of the L-PBF process concurrently suppresses the formation of austenite in the as-printed samples leading to either less than 1% of austenite in a 22Cr5Ni sample or an entirely a ferritic microstructure in 25Cr7Ni samples [6-8]. Davidson et al. reported Widmanstätten austenite evolution under higher energy densities with a base plate heating of 170 °C during L-PBF fabrication of 25Cr7Ni stainless steels [9]. Several methods have been explored to achieve the ferrite/austenite phase balance in the L-PBF fabricated samples namely using a nitrogen process atmosphere during printing and post-heat treatment processes [10,11]. Hengsbach et al. [6] reported observing highest austenite evolution (from 1% in as-printed to 34% in annealed) on subjecting an as-printed L-PBF 22Cr5Ni stainless steel through annealing for 5 minutes at 1000°C. Iams et al. [5] reported an increase in austenite phase content in the direct energy deposition fabricated samples of 25Cr7Ni stainless steel from 59 % to 65 % through hot isostatic pressing at 1170 °C, 140 MPa for 3 h. A prior investigation of L-PBF fabricated water atomized 25Cr7Ni stainless steel resulted in a completely ferritic microstructure. The present study was aimed on investigating the feasibility of obtaining a duplex (composed of ferrite and austenite) microstructure using hot isostatic pressing treatment of the as printed samples. The present study also focussed on evaluating the effect of hot isostatic pressing on physical, mechanical and corrosion properties of a L-PBF fabricated water atomized 25Cr7Ni stainless steel printed at 47 J/mm³.

Methodology

A water atomized 25Cr7Ni stainless steel with $D_{50} = 35 \mu\text{m}$ (North American Höganäs) was used as the starting powder in the study. The powder had an irregular morphology characteristic of water atomization. The bulk and tap density of the water atomized powder was 3.0 and 3.4 g/cc respectively. In terms of chemical composition, along with Fe, the powder had 25% Cr, 6.5% Ni, 1.8% Si, 1.3% Mo, 0.8% W and no nitrogen. A

total of 15 tensile samples were fabricated with a Concept Laser mLab cusing system with a 100W Yb laser with an energy density of 47 J/mm^3 (90W, 20 μm layer thickness, 120 μm hatch spacing, 800 mm/s scan speed). The samples were printed with their tensile axis parallel to the scan direction XY.

Two sets of 5 tensile samples each were subjected to HIP treatment (Quintus Technologies, Columbus US) at two distinct parameters, 1000 °C; 140 MPa; 3 h (HIP₁₀₀₀) & 1170 °C; 140 MPa; 3 h (HIP₁₁₇₀) in an argon atmosphere. The samples from both the conditions were followed by air cooling at 2.1 °C/s. The 10 HIP treated samples along with 5 as-printed L-PBF samples were characterized for their physical, mechanical and corrosion properties.

The Archimedes density of the as-printed samples along with the HIP treated samples were characterized using a Mettler Toledo XS104 analytical balance based on ASTM 962-17. The relative densities were calculated as the ratios of the Archimedes density to the gas pycnometer density of the water atomized 25Cr7Ni stainless steel. The tensile samples were characterized for their tensile properties using MTS Exceed hydraulic dual-column tensile testing system equipped with a 100 kN load cell, at a strain rate of 0.001 s^{-1} . The elongation of the samples was measured as the increase in gauge length prior to and after the tensile testing. The Rockwell hardness was characterized using a Rockwell C testing apparatus at 150 kgf load.

For metallography, the samples were sectioned along the build direction ZX and mechanically ground through grit sizes of 60, 120, 400, 800, and polished with 9 μm and 1 μm diamond solutions. The polished samples were subjected to optical microscopy to compare the porosity distribution between the as-printed and HIP treated samples. In terms of phase analysis, the polished samples were sonicated and analyzed by xray diffraction in a Discovery D8 diffractometer (BRUKER, AXS Inc., USA) at Cu-K α radiation ($\lambda = 1.54 \text{ \AA}$), 45kV, 40 mA. The recorded xrd patterns were matched against JCPDS cards corresponding to the most probable phases to evolve in 25Cr7Ni stainless steels. Towards microstructure characterization, electro-etching was done using 40% KOH solution at 4.5V DC (Direct Current) for a time span of around 5 seconds. The etched surfaces were characterized through an optical microscope. The microstructures were also characterized at higher magnifications using a TESCAN scanning electron microscope at an electron accelerating voltage of 20 kV. The chromium distribution under higher magnification was obtained as energy dispersive spectrum (EDS) elemental map and analysed using EDAX genesis software.

The corrosion properties of the as-printed and the HIP treated samples were characterized along the scan direction XY. The ground and polished samples were subjected to linear sweep voltametry experiments in 3.5% NaCl solution at room temperature through a Metrohm Autolab PGSTATION 100N system. The 25Cr7Ni stainless steels samples were used a working electrode, with a platinum counter electrode and an Ag/AgCl reference electrode. For each trial, the open circuit potential (E_{oc}) was recorded, and each measurement began from this value. This was followed by applying a DC voltage bias through the potentiostat between -1 V to 2 V at 0.01 mVs^{-1} and the current was recorded with a current density limit of 10 mA.cm^{-2} . The corrosion current, polarization resistance, and breakdown potentials were recorded. Tafel plots

were constructed with obtained corrosion current and the potentials. The corrosion rates were also calculated.

Results & Discussion

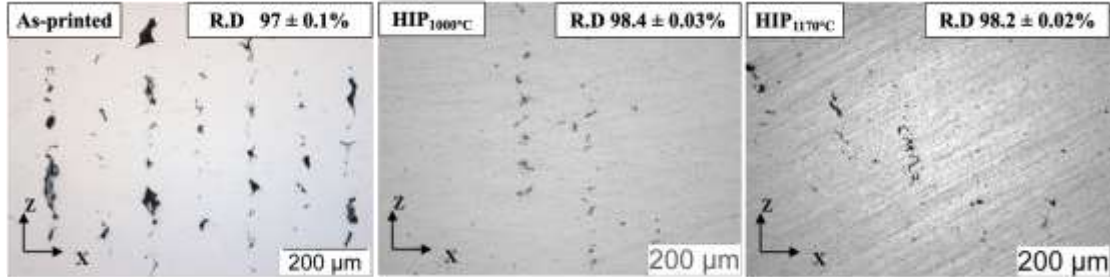


Figure 3.1 Micrographs of unetched sample in as-printed (left), printed+ HIP₁₀₀₀ condition (middle) and printed+ HIP₁₁₇₀ condition (right)

An increase in relative density of as-printed samples from $97 \pm 0.1\%$ to $98.4 \pm 0.03\%$ & $98.2 \pm 0.02\%$ was observed after HIP treatment at HIP₁₀₀₀ and HIP₁₁₇₀ respectively. The polished optical micrograph of the as-printed L-PBF sample along the build direction ZX predominantly displayed irregular pores due to un-melted powders. The micrographs also showed larger irregular pores that are continuous across multiple layers indicating lack of fusion [12]. With HIP treatment, a reduction in overall porosity in as-printed samples from over 5.4% to less than 0.01% was observed. Prior studies also reported a similar densification with concurrent closure of irregular pores upon HIP treatment of L-PBF printed samples [13,14].

Table 3.1: Mechanical Properties of 25Cr7Ni Stainless Steel

Stainless steel	Hardness (HRC)	Ultimate Tensile strength (MPa)	Yield strength (MPa)	Elongation (%)	Relative Density (%)
As-printed L-PBF 25Cr7Ni	26 ± 0.8	1000 ± 15	935 ± 17	12 ± 0.6	97 ± 0.1
HIP ₁₀₀₀	22.5 ± 1.5	900 ± 70	560 ± 30	18 ± 2	98.4 ± 0.03
HIP ₁₁₇₀	15 ± 1	885 ± 62	627 ± 32	9 ± 2	98.2 ± 0.02
Wrought 25Cr7Ni	29 ± 1	860 ± 30	580 ± 9	30 ± 2	100

The data in **Table 3.1**, clearly shows a decrease in the tensile strength, yield strength and hardness of the samples upon HIP treatment. The decrease in the properties was observed despite an increase in densification compared to as-printed L-PBF sample. The as-printed samples in the L-PBF technology are characterized by fine grain size and high dislocation density due to high cooling rates involved in the process. The fine grain size and high dislocation density contribute to the high tensile strength in the printed samples [15–17]. The HIP process is carried out by exposing the printed samples to temperatures above 1000 °C for a prolonged holding time resulting in recovery and annihilation of the dislocations followed by recrystallization and grain growth [18,19]. The reduction in dislocation density through annihilation and grain growth could be one of the reasons for the observed reduction in tensile and yield strength in the HIP treated samples. The reduction in hardness in the HIP treated samples along with the increase in elongation in HIP₁₀₀₀ condition and a lack of change

in elongation in HIP₁₁₇₀ condition will be analyzed based on phase and microstructural analysis in the following sections.

The XRD profile of the starting 25Cr7Ni stainless steel powder, as-printed L-PBF 25Cr7Ni sample, HIP₁₀₀₀, HIP₁₁₇₀ samples along with a wrought – annealed 25Cr7Ni stainless steel are collated and compared in **Figure 3.2**. The XRD analysis shows evolution of duplex microstructure in the HIP treated samples (ferrite $2\theta = 44^\circ, 64^\circ, 81^\circ$, austenite $2\theta = 43^\circ, 50^\circ, 74^\circ$). In comparison to the as-printed samples which showed peaks corresponding to only ferrite phase. In addition, the HIP treated samples also exhibited peaks that correspond to tetragonal σ ($2\theta = 45.3^\circ$) phase. Prior studies also reported observing the presence of tetragonal σ phase in HIP treated samples [20,21].

The etched micrographs of as-printed, and samples along the build direction ZX are collected in **Figure 3.3**. In comparison to the as-printed samples where the microstructure is purely ferritic (etched region), the HIP treated samples displayed ferrite (etched region) and austenite (un-etched region) microstructures. The evolution of austenite in the HIP treated samples can be correlated to the drop in tensile strength and yield strength as observed in [6].

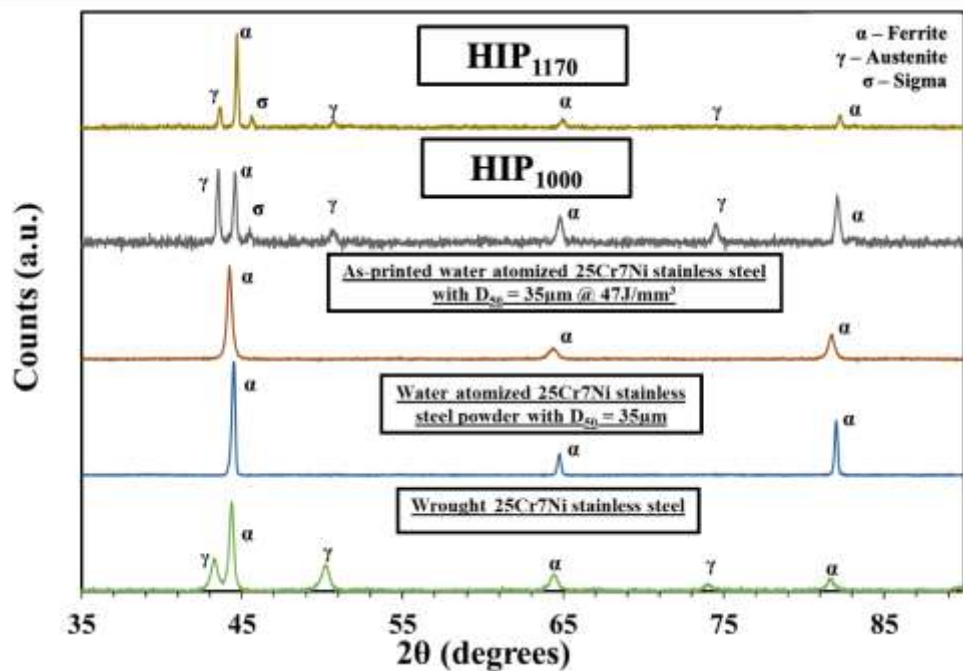


Figure 3.2 XRD profiles of 25Cr7Ni stainless steel samples

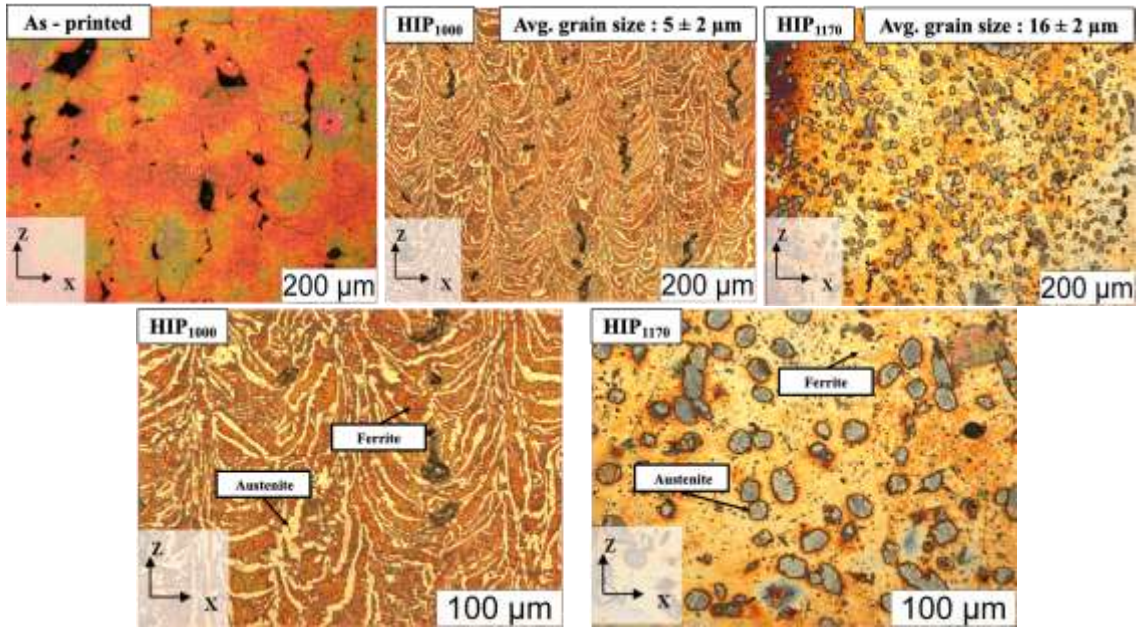


Figure 3.3 Optical micrographs of electro-etched as-printed (47 J/mm^3), HIP treated samples of L-PBF fabricated water atomized 25Cr7Ni stainless steel along the build direction (ZX)

The amount of austenite evolved in the HIP treated samples were quantified using image J software to be 30 % in both conditions. A difference in formation of austenite phase was observed in samples subjected to HIP_{1000} and HIP_{1170} condition. In case of HIP_{1000} , a continuous intra granular austenite phase was formed at the grain boundaries. The evolved austenite had an average grain size of $5 \pm 2 \mu\text{m}$. However, in case of HIP_{1170} , discontinuous and coarsened austenite grains was observed. The austenite in this condition was of an average grainsize of $16 \pm 2 \mu\text{m}$. In stark contrast to HIP_{1000} condition, the dissolution of melt-pool boundaries and corresponding elemental segregation was clearly evident in samples treated in HIP_{1170} condition. This difference in austenite microstructure between the two HIP treated samples, could aid in reasoning the higher elongation observed in HIP_{1000} condition. The tensile axis is perpendicular to the build direction ZX (optical micrographs). A continuous network of austenite grains in case of HIP_{1000} would thereby result in an increased elongation as opposed to a discontinuous yet coarsened austenite grains in HIP_{1170} .

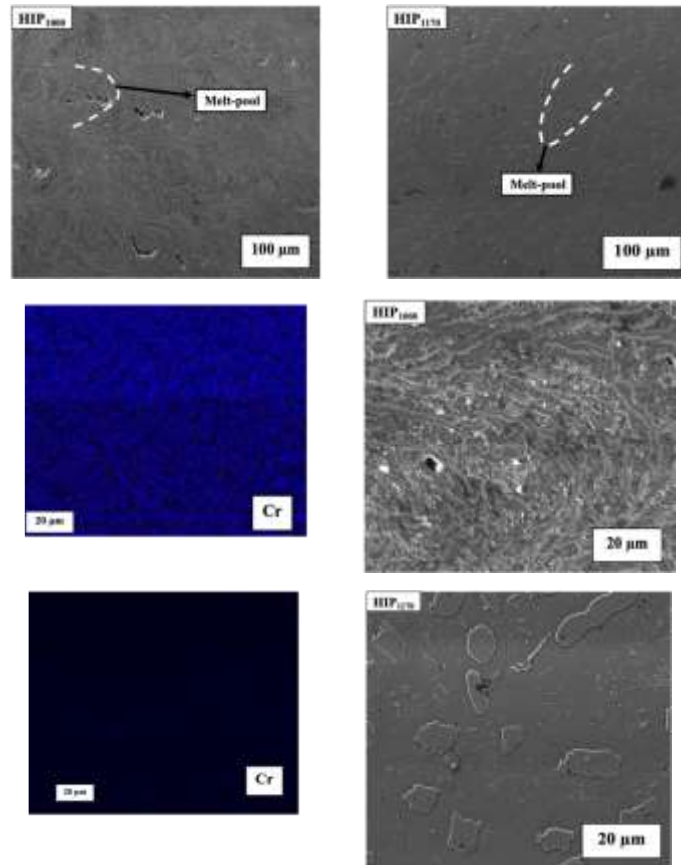


Figure 3.4 SEM micrographs / Cr EDS elemental maps of electro-etched HIP treated samples of L-PBF fabricated water atomized 25Cr7Ni stainless steel along the build direction (ZX)

The SEM micrographs of the electro-etched samples is shown in **Figure 3.4**. The micrographs reveal selective etched/smooth regions of ferrite and un-etched/raised regions of austenite [22]. The micrographs also show precipitates within the austenite grains of HIP₁₀₀₀ samples. However no significant precipitates were observed in HIP₁₁₇₀ samples. Chromium elemental maps (EDS) of HIP₁₀₀₀ samples, revealed the precipitates to be rich in chromium. The presence of precipitates in the austenite grains collaborates the identification of σ phase in the XRD analysis of the present study [20,23].

Table 3.2: Corrosion Properties of 25Cr7Ni Stainless Steel

Specimen	Relative Density (%)	Corrosion current, I_{corr} ($\mu\text{A}/\text{cm}^2$)	Breakdown potential, E_b (V)	Polarization resistance, R_p (Ω/cm^2) $\times 10^5$	Calculated corrosion rate ($\mu\text{m}/\text{year}$)
Water atomized 25Cr7Ni SS HIP ₁₀₀₀	98.4 \pm 0.03	0.1 \pm 0.01	1.1 \pm 0.0	1.5 \pm 0.7	9.3 \pm 4
Water atomized 25Cr7Ni SS HIP ₁₁₇₀	98.2 \pm 0.02	0.1 \pm 0.0	1.0 \pm 0.0	2.84 \pm 0.6	8.35 \pm 0.3
Water atomized 25Cr7Ni SS as-printed L-PBF (47 J/mm ³)	97 \pm 0.1	0.3 \pm 0.06	1.05 \pm 0.01	1.7 \pm 0.1	19.6 \pm 1
Wrought-annealed 25Cr7Ni SS	100	0.1 \pm 0.01	1.01 \pm 0.05	4.4 \pm 0.4	5.1 \pm 0.7

The corrosion properties of the water atomized L-PBF as-printed and HIP treated samples in terms of corrosion current, breakdown potential, polarization resistance and corrosion rate were calculated from the Tafel plots and are shown in **Table 3.2**. The corrosion properties of wrought – annealed 25Cr7Ni stainless steel samples are also included in **Table 3.2**. Compared to as-printed samples, the HIP treated samples displayed higher polarization resistance and lower corrosion rate. The superior corrosion resistance can be attributed to higher density (lower porosity) and presence of austenite phase in the microstructures in HIP treated samples. The superior effect of absence of porosity and presence of austenite phase on corrosion properties is very well reported in the literature. [24-27]. The corrosion properties of the HIP treated samples are found to be inferior when compared to wrought – annealed 25Cr7Ni stainless steels. The significantly higher austenite content (over 60 %) in the wrought - annealed 25Cr7Ni stainless steel as compared to HIP samples (over 30%) in the present study might be the reason for superior corrosion resistance of the wrought – annealed 25Cr7Ni stainless steel [26,28].

Conclusions

- HIP treatment of water atomized L-PBF as-printed samples resulted in higher densification of samples. The density of the samples increased from 97 \pm 0.1% to 98.4 \pm 0.03 % & 98.2 \pm 0.02 % with HIP treatment at 1000 and 1170°C. HIP treatment of the printed samples resulted in achieving duplex microstructure of both austenite and ferrite phases
- The annihilation of dislocations, grain growth and presence of austenite phase in the HIP samples resulted in lower yield strength, tensile strength and hardness compared to as printed samples
- A difference in evolution of austenite phase was observed on HIP treatment at 1000 and 1170°C. The samples HIP treated at 1000C showed continuous network of intra-granular austenite. However the samples HIP treated at 1170°C showed discontinuous coarsened austenite grains

- The XRD and metallography analysis confirmed presence of σ phase chromium rich precipitates within the intra-granular austenite grains for HIP samples at 1000°C
- The presence of lower porosity and austenite phase in HIP treated samples resulted in superior corrosion resistance compared to as printed L-PBF printed sample

CHAPTER 4 INFLUENCE OF POWDER CHARACTERISTICS & CHEMICAL COMPOSITION ON THE PROPERTIES OF 25CR7NI STAINLESS STEEL FABRICATED BY LASER-POWDER BED FUSION

Introduction

The 25Cr7Ni stainless steel alloys were developed through careful control of their chemical composition to present a duplex microstructure, approximately 50% ferrite and 50% austenite, combining the strength of 420 steels and corrosion resistance of 316L steels [1]. These alloys adequately address the demands of high strength and corrosion resistance required by components used in offshore oil & gas industry, chemical digester plants where they are constantly exposed to a highly corrosive environment [2]. The chemical composition of the 25Cr7Ni stainless steel alloy, having over 27% of alloying elements, is sensitive to the temperature – time profile of any heat treatment / hot forming operation. At slower cooling rates of conventional hot forming processes, the 25Cr7Ni stainless steel alloy system has been shown to promote precipitation of detrimental phases such as χ , σ phases [3,4] which severely impede the mechanical and corrosion resistant properties. Limitations of a slower cooling rate, lack of design integration/complexity, inability to adequately recycle raw materials has garnered a high degree of interest in Laser-powder bed fusion for processing 25Cr7Ni stainless steel alloy systems [5].

With the primary raw material for the L-PBF process being powder, powder attributes such as morphology and particle size distribution have a significant influence on the L-PBF printability and the printed part porosity [6]. The mode of atomization has a direct co-relation with the powder morphology with water atomization predominantly yielding an irregular morphology and gas atomization yielding a more regular, spherical morphology but being a costlier alternative [7,8]. An irregular morphology of the starting powder has been shown to have a lack of uniform spreading / compaction in the powder bed due to inter-locking of the powder particles which eventually manifests as porosity, lack of fusion between powder layers and even failed prints [6,7]. Conversely, a spherical morphology results in uniform powder spreading & adequate powder bed compaction leading to over 99% relative densities of as-printed L-PBF parts [9,10]. In terms of chemical composition, water atomization due to its in-ability to provide an inert atmosphere for atomization is limited in the scope of alloying elements that can promote oxygen pick up during atomization such as manganese [11].

Independently, the chemical composition of the starting powder influences the printed part properties by affecting the phase balance. Elements such as Cr, Mo are ferrite stabilizers and Ni, N are austenite stabilizers, with manganese shown to increase the solubility of N in the stainless-steel alloy [1]. The corrosion resistance of the alloy system is heavily governed by the Cr, Mo, and N content [12,13]. Few studies have been conducted to establish the influence of the powder attributes and chemical composition of the starting powder on the mechanical properties, microstructure of L-PBF fabricated 25Cr7Ni stainless steel [14–17] with no qualification of corrosion properties of the fabricated parts. The present study seeks to address that research gap.

Methodology

For the present work, a gas atomized 25Cr7Ni stainless steel powder with a D_{10} of 20.6 μm , D_{50} of 32, D_{90} of 51.9 μm , provided by Sandvik Additive Manufacturing, USA, was used as the starting powder. The as-printed properties of the fabricated samples were compared with the as-printed properties of a L-PBF fabricated water atomized 25Cr7Ni stainless steel powder with a D_{10} of 16 μm , D_{50} of 35 μm , D_{90} of 62 μm provided by North American Hoeganaes, USA, printed at the same process parameters. The pycnometer densities of the water atomized powder was 7.68 ± 0.02 g/cc and gas atomized powder was 7.66 ± 0 g/cc.

The chemical composition of the gas atomized 25Cr7Ni stainless steel powder, shown in **Table 4.1.**, fulfilled ASTM standard 25Cr7Ni stainless steel composition (UNS 32750). In comparison, the water atomized 25Cr7Ni stainless steel powder had the same amount of Cr and Ni content as the ASTM standard 25Cr7Ni stainless steel but had lower amounts of Mo, Mn, and no N. In contrast it had higher amounts of W and Si in comparison to an ASTM standard 25Cr7Ni stainless steel.

A Concept Laser mLab cusing machine equipped with a single 100W Yb laser was used to carry out the L-PBF process to fabricate five ASTM E8 M tensile specimens with the gas atomized and water atomized 25Cr7Ni stainless steel powders, at an energy density of 47 J/mm^3 (90W, 20 μm layer thickness, 120 μm hatch spacing, 800 mm/s scan speed). The samples were fabricated with the tensile axis parallel to the build plate / scan direction (XY). The build direction was (ZX). The samples were fabricated in a constant flow of argon gas within the build chamber limiting the oxygen content to less than 0.5%.

Table 4.1: Composition of starting gas atomized 25Cr7Ni stainless steel powder

Elements	Type of 25Cr7Ni Stainless Steel	
	Water Atomized (%)	Gas Atomized (%)
Cr	25	25.1
Ni	6.2	7.2
Mo	1.3	3.94
Cu	2	0.02
Si	1.8	0.5
W	0.8	0.01
Mn	0.1	0.9
N	-	0.28
C	0.02	0.02
P	0.015	0.01
S	0.009	0.007
Fe	Balance	Balance

The bulk density, tap density and the pycnometer density of the starting powders were characterized using an AS-100 tap density volumeter and a micrometrics gas pycnometer. The Hausner's ratio, which was qualitatively used to characterize the flowability of the starting powder during the L-PBF process and the powder bed packing density similar to the works of [10,18], which was calculated as the ratio of the tap density to the apparent density. The as-printed samples were cut from the base plate and their Archimedes density was calculated using a Mettler Toledo XS104 analytical balance based on ASTM 962-17 standard. The relative density of the as-printed samples was calculated as the ratio of the Archimedes density to the pycnometer density of the respective starting powder.

The x-ray diffraction (XRD) of the as-printed samples were captured using a Discovery D8 diffractometer (BRUKER, AXS Inc., USA) at Cu-K α radiation ($\lambda = 1.54 \text{ \AA}$), 45kV, 40 mA. The microstructure of the as-printed samples was captured along the building direction (ZX), by sectioning the as-printed sample followed by mechanically grinding with grit sizes of 60, 120, 400, 800, and polished with 9 μm and 1 μm diamond solutions. The polished samples were then electrically etched in a DC current at 3V for 5 seconds in a 40% KOH solution, immediately followed by cleaning the sample with distilled water. This selectively etched ferrite phase and left the austenite unetched.

The L-PBF as-printed samples were subjected to tensile testing in an MTS Exceed hydraulic dual-column tensile testing system equipped with a 100 kN load cell, at a strain rate of 0.001 s^{-1} . The elongation of the samples was measured as the increase in gauge length prior to and after the tensile testing.

The corrosion properties of the as-printed samples were characterized in a 3.5% sodium chloride solution to simulate the salinity of the seawater. using Linear sweep voltammetry (LSV). A pre-defined area was polished to mirror-like surface finish along the scan direction (XY) and was exposed to a 3.5% sodium chloride electrolyte. The as-printed sample served as the working electrode, a silver-silver chloride electrode

served as the reference electrode and a platinum wire mesh served as a counter electrode. All the electrodes were immersed in the sodium chloride electrolyte and externally connected through a potentiostat. The voltage was swept across -1 V to 2 V using the potentiostat and the corrosion current was recorded. The corrosion resistance was calculated using the Tafel plots and Tafel equations [18,19], to obtain polarization resistance, breakdown potential, corrosion current and the corrosion rate.

Results & Discussion

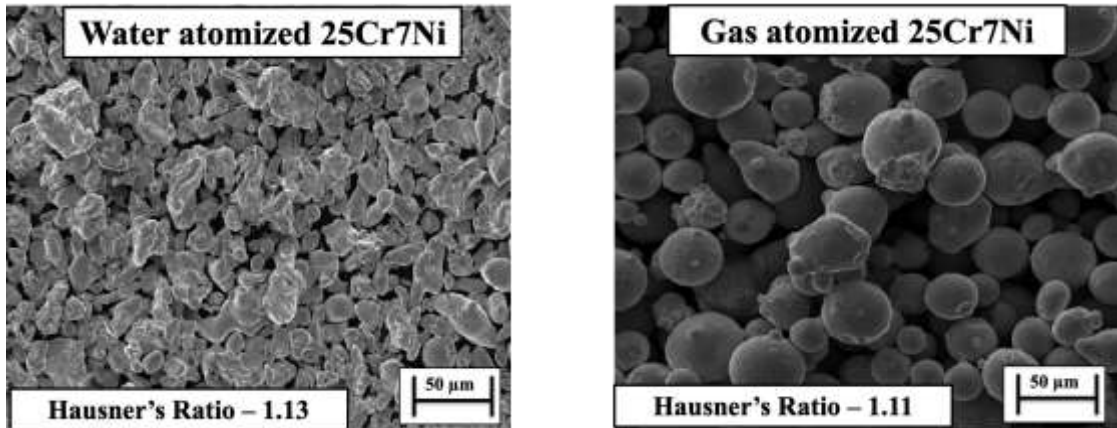


Figure 4.1. SEM micrographs of (left) water atomized 25Cr7Ni powder (right) gas atomized 25Cr7Ni powder

From the SEM micrographs in **Figure 4.1**, we can see that the gas atomized powders had a more uniform and a spherical morphology in comparison to the water atomized powders. The observed morphology trend could be explained by the atomization media / atomizing jets, with water atomization employing water and gas atomization employing gases such as Ar & N. The process workflow of the atomization process involves segregating the metal melt introduced into the atomizer, through an atomizing jet, into droplets. The segregated droplets cool down and solidify into water slurry (in case of water atomization) / powder slurry (in case of gas atomization) [8]. The cooling rates afforded by a water atomizing medium is about two orders of magnitude higher than gas atomizing medium, which restricts the time available for the segregated melt droplet to solidify under its own surface tension into spherical particles in the case of water atomization. This is the main reason for the irregular morphology of powders atomized through water atomization [7,20].

Comparing the bulk densities characterized for the starting powders, the gas atomized powder had a higher bulk density of 4.28 ± 0.02 g/cc in comparison to water atomized powder which had a bulk density of 3.0 ± 0.01 g/cc. When analysing the D_{10} sizes and the D_{90} sizes of the starting powders, the water atomized powders had wider distribution of fine and large sized particles (D_{10} 16 µm and the D_{90} 62 µm) than gas atomized powders (D_{10} 20.6 µm and the D_{90} 51.9 µm). In the works of [21,22], a wider distribution in particle sizes enables a higher bulk / powder bed packing density with finer powder particles packing in the voids between the larger sized powder particles. In the context of the present study, water atomized powders in spite of a wider particle size distribution yielded a lower bulk density than gas atomized powders, due to the irregular morphology - promoting inter-locking between the powder particles and in-turn retarding powder flow and spread [23]. The Hausner's ratio, which aides in

quantifying the powder bed packing density, were characterized for water atomized powders as 1.13 and gas atomized powders as 1.11, with a lower value co-relating to a higher bulk / powder bed packing density.

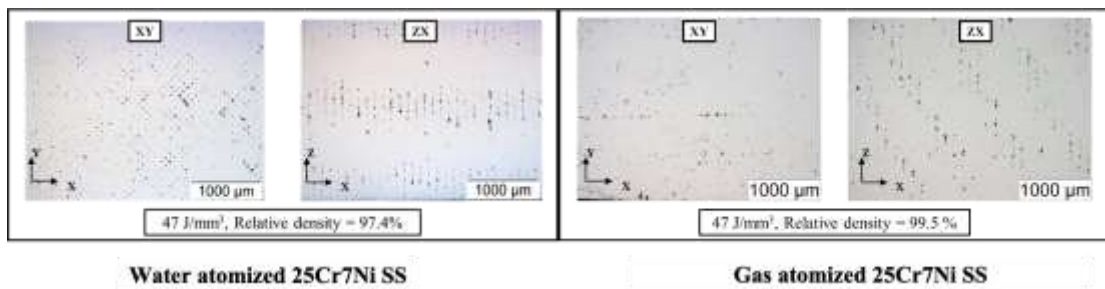


Figure 4.2 Optical micrographs of L-PBF (left) water atomized 25Cr7Ni samples (right) gas atomized 25Cr7Ni samples

The Archimedes density and relative density of the as-printed L-PBF samples from the water atomized powders were characterized to be 7.48 g/cc and 97.4 % were lower than the densities of as-printed L-PBF samples from gas atomized powders which were 7.62 g/cc and 99.5 %, co-relating with the lower powder bed packing density of water atomized powders. The unpacked voids in the powder bed prevalent in the water atomized powders, primarily solidified as porosities in the as-printed samples [24]. The optical micrographs in **Figure 4.2**, captures the distribution of pores in both scan (XY) & build directions (ZX) in the L-PBF as-printed samples. The average porosity in the as-printed samples from the water atomized powders were characterized to be over 3 % in comparison to less than 0.5 % in as-printed samples from gas-atomized powders correlating with the results of powder bed packing density. The porosity was characterized using image J software.

Apart from powder bed compaction, spatter generation (liquid spattering & hot powder spattering) during the interaction of laser with melt pool & powder particles contribute towards evolution of porosity in L-PBF as-printed samples [25,26]. Looking at hot powder spattering, ejection of un-melted powder by the melt pool vapours, [23] reported that the irregular morphology of water atomized powders promoted interlocking between powder particles resulting in larger sized spatters being ejected in comparison to similarly sized, spherical gas atomized powders along the laser scan tracks. Studying the optical micrographs along scan direction (XY) in **Figure 4.2**, in this context, for the same process parameters (laser power, scan speed, hatch spacing & layer thickness), as-printed samples from water atomized powders exhibited more porosity than as-printed samples from gas atomized powders.

The oxygen content in the starting powders of water and gas atomized stainless steel powders were characterized using a Leco elemental analyser to be 0.171 ± 0.042 % in water atomized powder & 0.07 ± 0.005 % in gas atomized powder. Kaplan et al. [27] reported that even a small variations in concentrations of surface active elements such as oxygen can directly impact thermo-capillary forces of the melt with a higher oxygen

content resulting in lower surface tension of the melt and larger liquid spatter able to escape the melt. The higher oxygen content in the water atomized powders could have resulted in larger liquid spatters increasing the porosity of their as-printed L-PBF parts. The reduction in surface tension of the melt pool also decreases the wettability of the melt with the powder particles leading to porosities from lack of fusion between powder layers [23].

Figure 4.3 collates the mechanical properties of the L-PBF samples printed from water atomized, gas atomized powders of 25Cr7Ni stainless steels with a wrought-annealed 25Cr7Ni stainless steel. L-PBF samples from both the powder lots had a higher UTS and hardness than the wrought – annealed 25Cr7Ni stainless steel sample, primarily due to the high dislocation densities inherent to the L-PBF as-printed samples from the intense thermal cycles of the process [15], as well as grain refinement from high cooling rates [14]. The higher elongation of the wrought – annealed samples over the L-PBF samples can partially be attributed to the lack of porosities in the wrought – annealed samples. Comparing the L-PBF samples, the samples produced from gas atomized powders had a higher UTS, elongation as well as hardness than the samples produced from water atomized powders. The higher porosity of the samples from the water atomized powder lot could be one of the reasons for this difference in mechanical properties, as lack of densification in L-PBF samples have been shown to have a limiting effect on the as-printed L-PBF sample mechanical properties [10,18]. Looking in terms of the chemical compositions of the two powder lots, the gas atomized powders had over twice the amount of N, three times more Mo and over nine times more Mn content than the water atomized powders. Mo & Ni are strong substitutional solid solution strengthening elements, N is similarly a strong interstitial solid solution strengthening element with Mn contributing towards marginally improving UTS without compromising the ductility [28–30]. The higher UTS and elongation of the L-PBF samples from the gas atomized powders over the L-PBF samples from the water atomized powders can also be reasoned based on the above-mentioned influence of the alloying elements.

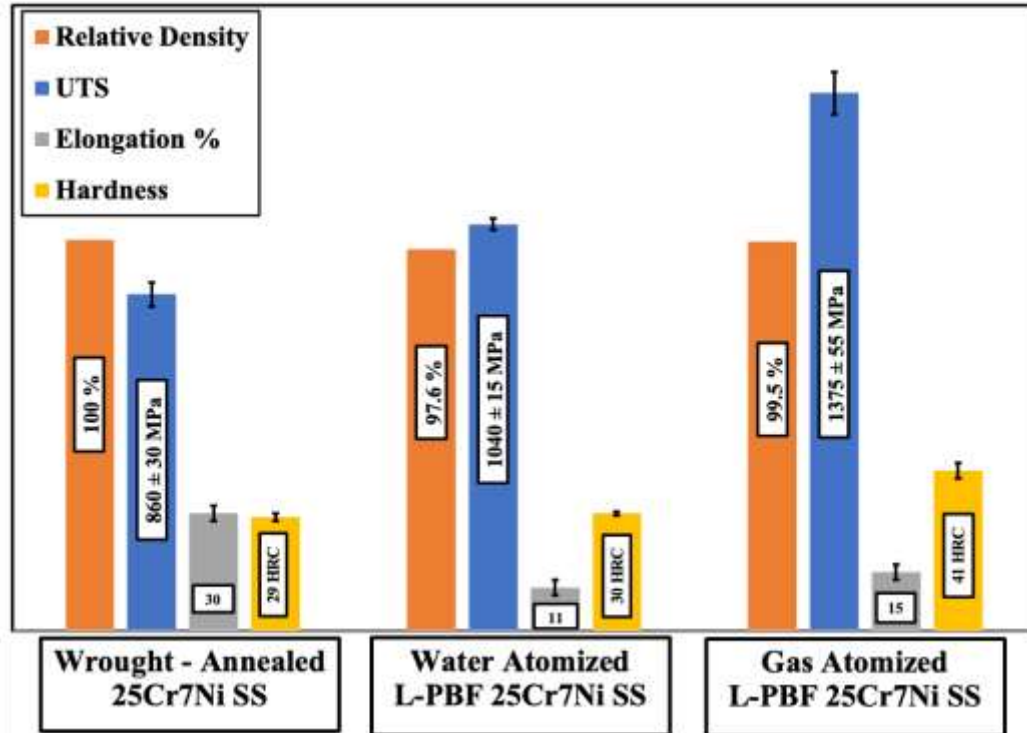


Figure 4.3 Comparison of mechanical properties

Figure 4.3 collates the XRD profiles for a wrought – annealed, L-PBF samples from gas atomized (GA), water atomized (WA) powders of 25Cr7Ni stainless steel. Both austenite peaks ($2\theta = 43^\circ, 50^\circ, 74^\circ$) and ferrite peaks ($2\theta = 44^\circ, 64^\circ, 81^\circ$) were registered in the XRD profile of the wrought – annealed 25Cr7Ni stainless steel sample. XRD profiles of L-PBF samples printed from the water atomized powders displayed only ferrite peaks, while the L-PBF samples from the gas atomized powders displayed both ferrite and austenite peaks. The above observation can be explained based on two competing phenomena. The high cooling rates involved in the L-PBF processes ($10^6 - 10^7$ K/s), effectively suppress the decomposition of ferrite into austenite in the as-printed state during fabrication [31]. Specific elements in the alloy composition such as, nitrogen (primary austenite phase stabilizer), manganese (improves solubility of nitrogen in austenite) aid in stabilizing the retained austenite formed during the L-PBF process [28,32]. With no N and over nine times less Mn in the water atomized powder in comparison to gas atomized powders, possibility of any retained austenite in the corresponding L-PBF samples of the water atomized powders is completely negated by the high cooling rates of the L-PBF process. Presence of austenite in the L-PBF samples printed from gas atomized powders can also be co-related to their higher elongation than samples from water atomized powder, as austenite phase has been shown to afford higher elongation than ferrite phase [18].

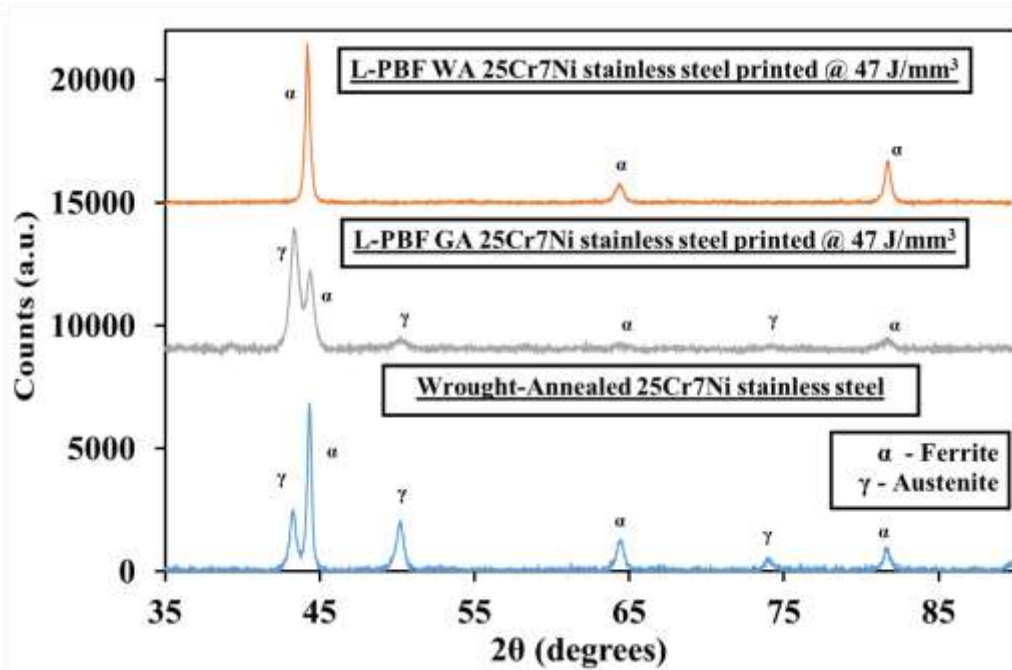


Figure 4.4 Collated XRD profiles of (top) L-PBF water atomized (middle) L-PBF gas atomized (bottom) wrought – annealed 25Cr7Ni samples

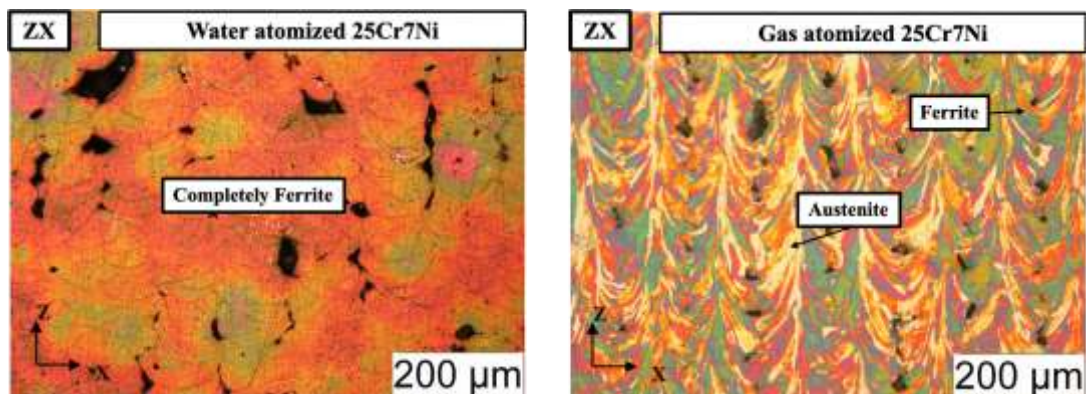


Figure 4.5 Optical micrographs of electro-etched L-PBF (left) water atomized 25Cr7Ni samples (right) gas atomized 25Cr7Ni samples along the build direction (ZX)

The electro-etched micrographs in **Figure 4.5** corroborate the XRD results, with the L-PBF samples from the water atomized powders being completely etched to reveal a 100% ferrite microstructure and the L-PBF samples from the gas atomized powders reveal both an etched ferrite phase and an unetched grain boundary austenite phase. The fraction of retained austenite in the L-PBF samples from the gas atomized powders were estimated with Image J software to be around 15%. Detrimental phases such as σ & χ phases were not observed in both the cases.

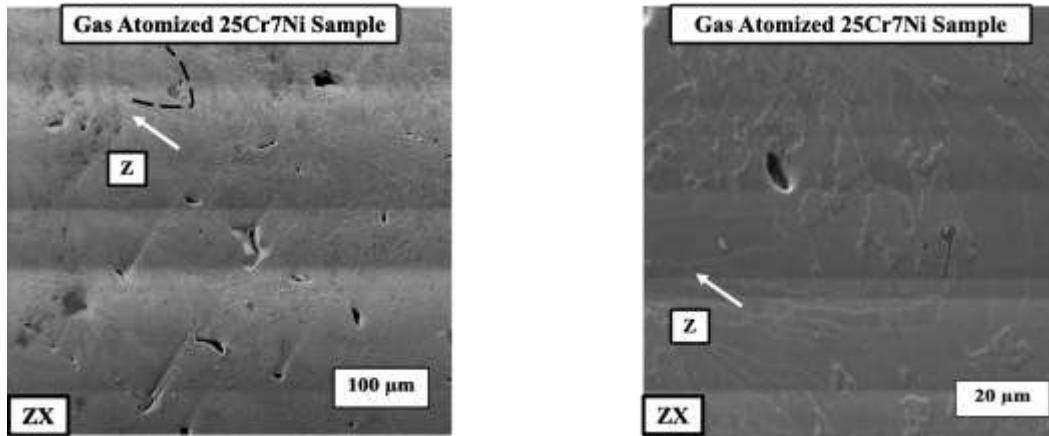


Figure 4.6 SEM micrographs of electro-etched L-PBF gas atomized 25Cr7Ni sample along the build direction (ZX)

With the presence of both ferrite and grain boundary austenite in the L-PBF samples from the gas atomized powder, the corresponding electro-etched samples were observed under SEM and EDS to study if there were any elemental partitioning / segregation between the phases. The SEM micrographs did not reveal any precipitates nor the EDS any elemental partitioning between the ferrite and austenite phases.

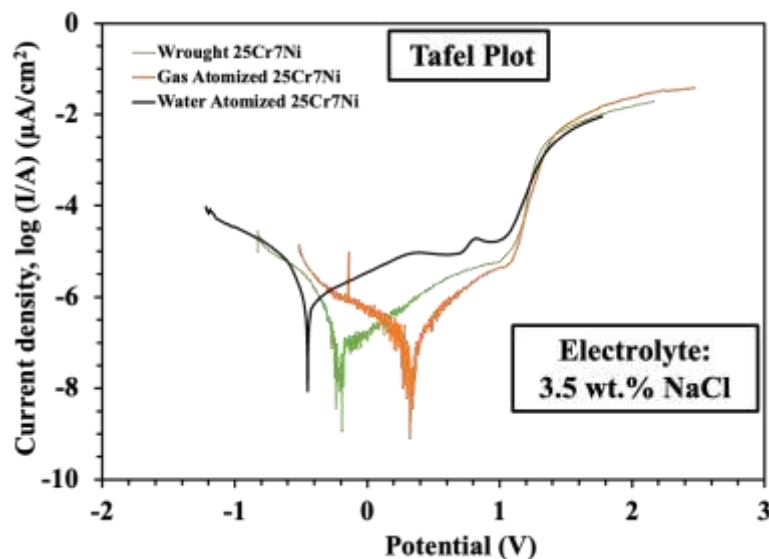


Figure 4.7 Tafel plots from the linear sweep voltammetry experiments collated with (black) L-PBF sample from water atomized (green) wrought – annealed (orange) L-PBF sample from gas atomized 25Cr7Ni stainless steel

The results from the linear sweep voltammetry experiments were processed using NOVA software, from which Tafel plots were extracted as seen in **Figure 4.7**. The corrosion properties of all the samples in terms of corrosion current, breakdown potential, polarization resistance and the corrosion rate were obtained by the use of Tafel equations and Butler – Volmer equations [9].

Table 4.2: Comparison of Corrosion Properties

Specimen	Relative Density (%)	Corrosion Current, I_{corr} (μA)	Breakdown Potential, E_b (V)	Polarization Resistance, R_p (Ω/cm^2) $\times 10^5$	Corrosion Rate ($\mu\text{m}/\text{year}$)
L-PBF gas atomized 25Cr7Ni	99.5	0.06 ± 0.04	1.1 ± 0.02	6.3 ± 0.6	3.05 ± 2
L-PBF water atomized 25Cr7Ni	97.6	0.3 ± 0.06	1.0 ± 0.01	1.7 ± 0.1	19.6 ± 1
Wrought – annealed 25Cr7Ni	100	0.1 ± 0.01	1.0 ± 0.05	4.4 ± 0.4	5.1 ± 0.7

Table 4.2 collates the corrosion properties of the L-PBF samples from the gas atomized powders, water atomized powders, wrought – annealed 25Cr7Ni stainless steels. The L-PBF samples from the gas atomized powders had about 6 times the corrosion resistance than the L-PBF samples from the water atomized powder in terms of higher polarization resistance, breakdown potential, lower corrosion current and corrosion rate. They also had a comparable corrosion resistance to the wrought – annealed 25Cr7Ni stainless steel.

The higher corrosion resistance of the L-PBF samples from the gas atomized powders over the L-PBF samples from the water atomized powders can be reasoned on two fronts. Subrata et al. [9] and Irrinki et al. [10] reported that the inherent part porosity in the as-printed L-PBF samples served as sites for localized pitting corrosion, primarily due the lack of exposure of the electrolyte in the pores to oxygen, decreasing their pH and promoting further corrosion [33,34]. Looking at the corrosion resistance trend in this context, the calculated porosity of the L-PBF samples from the water atomized powders was over 3% in comparison to less than 0.5% in the case of L-PBF samples from gas atomized powders which could in-turn contribute to a higher corrosion resistance in the L-PBF samples from the gas atomized powders. Next, the influence of the alloying elements in the starting powders and their corresponding influence on the phases evolved, have on the corrosion properties is considered. The gas atomized powders had higher amounts of N, Mn which being strong austenite stabilizers, promoted the retention of 15% austenite in the L-PBF samples in comparison to water atomized powders which had no N and nine times less Mn leading to complete suppression of austenite formation in their corresponding L-PBF samples. Austenite phase has been widely reported to have higher corrosion resistance properties than ferrite phase [12,35]. Apart from austenite stabilization, N inherently retards the corrosion rate of the corrosion process [36]. The gas atomized powders also had over three times more Mo than the water atomized powders. Presence of Mo is important for passivation of corroding surfaces in stainless steel systems in turn increasing their corrosion resistance [28].

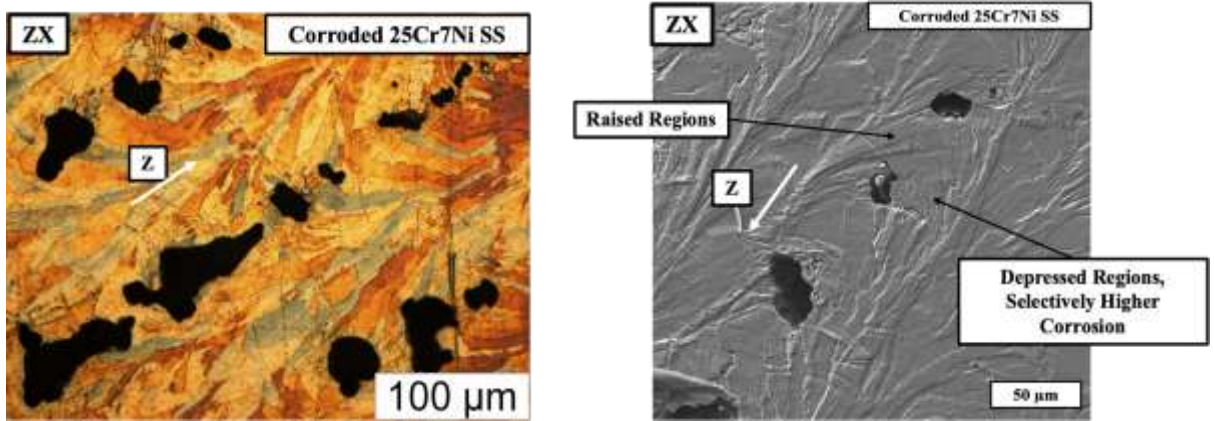


Figure 4.8 (Left) Optical micrograph of corroded & eletroetched, (right) SEM micrograph of corroded & un-etched L-PBF gas atomized sample

Dwelling on the corrosion of the L-PBF samples printed from the gas atomized powders, **Figure 4.8** (Left) captures the optical micrograph of corroded & eletroetched L-PBF sample from the gas atomized 25Cr7Ni stainless steel powder, (right) SEM micrograph of corroded & un-etched L-PBF sample from the gas atomized 25Cr7Ni stainless steel powder in the build direction (ZX). In the SEM micrograph, where the sample is only corroded, alternatively raised and depressed regions with the epitaxy similar to the etched microstructure of ferrite and grain boundary austenite is observed. The corrosion pits also are selectively present in the depressed regions. Upon eletroetching, the depressed / corroded regions are revealed to be ferrite possibly indicating the susceptibility of ferrite regions in 25Cr7Ni stainless steel samples to undergo a higher degree of corrosion than austenitic regions.

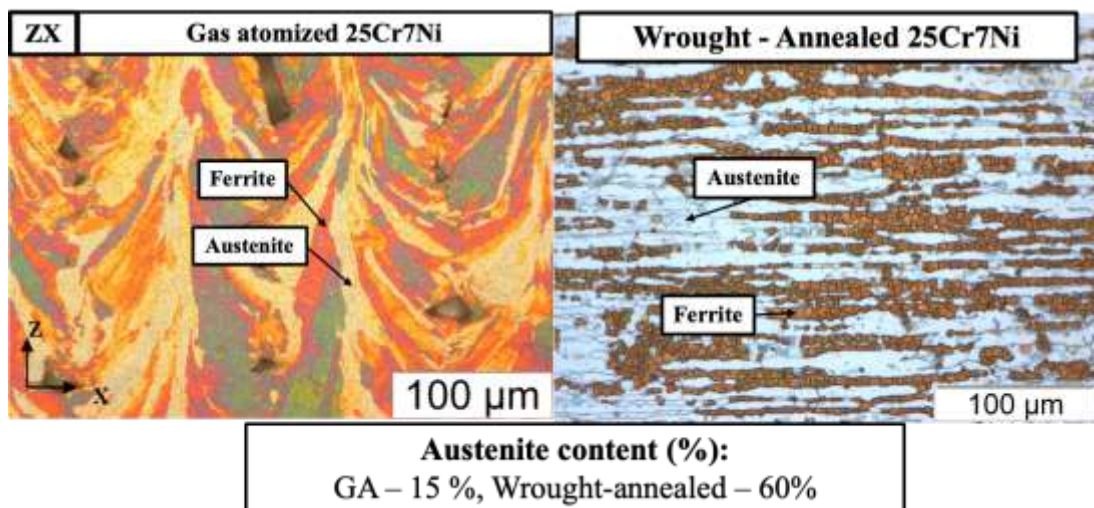


Figure 4.9 Eletroetched optical micrographs of L-PBF samples from gas atomized (GA) powders, wrought – annealed 25Cr7Ni stainless steel

The L-PBF samples from gas atomized powders had a comparable corrosion resistance to the wrought – annealed 25Cr7Ni stainless steel. Both the samples had comparable chemical compositions. However, the L-PBF samples from the gas atomized powders,

despite having four times lower amounts of austenite phase was able to match the corrosion resistance of the wrought – annealed samples. One observable difference between the etched micrographs was the texture of the evolved microstructure between the L-PBF sample and the wrought – annealed sample. With texture of grains and microstructure having a significant impact on the corrosion resistance of the alloy [37,38], the observed high corrosion resistance of L-PBF samples from gas atomized powders being comparable to wrought – annealed 25Cr7Ni stainless steel samples in spite of a lower austenite content can be attributed to the difference in their ferrite / austenite microstructure textures.

Conclusions

- Higher densification was achieved in L-PBF samples printed from gas atomized 25Cr7Ni stainless steel powder with spherical morphology compared to water atomized 25Cr7Ni powder with irregular morphology L-PBF samples due to higher powder bed packing density contributing to the superior densification of samples
- The microstructures of samples printed from gas atomized 25Cr7Ni powders displayed significant amount of retained austenite phase along with ferrite. The presence higher amounts of austenite stabilizers like N, Mn and Ni in gas atomized powders compared to water atomized powders, contributed to the presence of austenite phase in the microstructure which indicate the possibility of L-PBF technology to achieve duplex microstructure (50% - 50%) with additional thermal treatment
- Lack of porosities in the L-PBF samples from gas atomized powders translated to a higher set of mechanical properties (UTS, elongation, hardness) over L-PBF samples from water atomized powders and wrought – annealed 25Cr7Ni stainless steel
- The LPBF printed samples from gas atomized powders showed superior corrosion resistance properties compared to samples printed from water atomized powders possibly due to the presence of austenite phase, higher N, Mo, Mn and lower porosities in samples printed from gas atomized powders
- The comparable corrosion resistance of L-PBF samples from gas atomized powders with wrought – annealed 25Cr7Ni stainless steels despite having four times lower amounts of austenite could possibly be due to the characteristic microstructure texture in the L-PBF samples
- With higher UTS, hardness and comparable corrosion resistance properties, the as-printed L-PBF samples from the gas atomized powders can replace the wrought – annealed 25Cr7Ni stainless steel

CHAPTER 5 INFLUENCE OF PROCESSING ATMOSPHERE ON THE PROPERTIES OF LASER- POWDER BED FUSION FABRICATED 25CR7NI STAINLESS STEEL

Introduction

Laser-powder bed fusion (L-PBF) is an additive manufacturing technology which is based on successive iterations of powder spreading – laser melting – melt solidification, yielding near-net shape parts [1]. The entire process is carried out under an inert atmosphere to prevent oxygen pick up by the melt and to avoid any spontaneous combustion while working with flammable powders [2]. The process offers the capability to fabricate near-net shaped parts involving complex geometries [3]. The process is characterized by a very high cooling rate, $\sim 10^6$ k/s, which affords the means to process and preserve certain metal alloys of novel chemical compositions [4]. The 25Cr7Ni stainless steel is a high alloyed stainless steel with 25% Cr and 7% Ni, with a phase balance of approximately 50% ferrite and 50% austenite [5]. This unique phase balance gives the steel a robust combination of high strength and high corrosion resistance [6]. Owing to the higher cooling rates during the process, the 25Cr7Ni stainless steels fabricated through L-PBF contain a predominantly ferritic microstructure [7]. An additional heat treatment step is required post fabrication to promote and stabilize austenite phase within the stainless steel matrix [8]. Apart from a separate heat treatment step, one of the other avenues for promoting and stabilizing the formation of austenite phase is through addition of austenite stabilizers to the starting powder such as Mn, Ni, N [6,9]. For a given specific composition of the 25Cr7Ni stainless steel powder, addition of Mn, Ni is a relatively costlier proposition [10]. However, one can leverage the workflow of the L-PBF process, which involves continuous melting and solidification of the 25Cr7Ni stainless steel along with the inert atmosphere used during the process to promote austenite formation and stabilization in the as-printed state. Gases such as Ar and N are predominantly used for creating the inert atmosphere, with N being the cheaper alternative to Ar [10] gas. Having already established the role of N as an austenite stabilizer, this study explored the possibility of using N gas during the L-PBF fabrication as the process gas to promote the formation and stabilization austenite phase within the 25Cr7Ni stainless steel in the as-printed state. This study evaluated the physical, mechanical and corrosion properties of two different sets of samples fabricated through L-PBF from the same starting 25Cr7Ni stainless steel powder fabricated at the same L-PBF process conditions under Ar and N inert atmospheres.

Methodology

A gas atomized 25Cr7Ni stainless steel powder with a D_{10} of 20.6 μm , D_{50} of 32, D_{90} of 51.9 μm , provided by Sandvik Additive Manufacturing, USA, was used as the starting powder. The pycnometer density of the gas atomized powder was 7.66 ± 0 g/cc. The chemical composition of the gas atomized 25Cr7Ni stainless steel powder, shown

in **Table 5.1**, fulfilled ASTM standard 25Cr7Ni stainless steel composition (UNS 32750). The oxygen, carbon, nitrogen, sulphur and hydrogen composition of the as-printed L-PBF samples was also recorded using LECO elemental analyser.

A Concept Laser mLab cusing machine equipped with a single 100W Yb laser was used to carry out the L-PBF process to fabricate banks of five ASTM E8 M tensile specimens with the gas atomized 25Cr7Ni stainless steel powders, at an energy density of 47 J/mm³ (90W, 20 µm layer thickness, 120 µm hatch spacing, 800 mm/s scan speed). The samples were fabricated with the tensile axis parallel to the build plate / scan direction (XY). The build direction was (ZX). The samples were fabricated in a constant flow of both Ar and N gas within the build chamber limiting the oxygen content to less than 0.5%. The tensile samples were individually machined out of the as-printed banks through wire cut electrical discharge machining.

Table 5.1: Chemical Composition

Alloy (%)	Si	P	Cr	Mn	S	Ni	Cu	Mo	W	C	Fe	N
Gas atomized 25Cr7Ni SS	0.5	0.01	25.1	0.9	0.007	7	0.02	3.94	N.A	0.02	Bal.	0.28
UNS S32750 ASTM	0.8	0.035	24 - 26	1.2	0.02	6 - 8	0.5	3 - 5	0.01	0.03	Bal.	0.24 – 0.32

The pycnometer density of the starting powders was characterized using a micrometrics gas pycnometer. The as-printed samples were characterized for their Archimedes density using a Mettler Toledo XS104 analytical balance based on ASTM 962-17 standard. The relative density of the as-printed samples was calculated as the ratio of the Archimedes density to the pycnometer density of the starting powder.

The x-ray diffraction (XRD) of the as-printed samples were captured using a Discovery D8 diffractometer (BRUKER, AXS Inc., USA) at Cu-K α radiation ($\lambda = 1.54 \text{ \AA}$), 45kV, 40 mA. The microstructure of the as-printed samples was captured along the building direction (ZX), by sectioning the as-printed sample followed by mechanically grinding with grit sizes of 60, 120, 400, 800, and polished with 9 µm and 1 µm diamond solutions. The polished samples were then electrically etched in a DC current at 3V for 5 seconds in a 40% KOH solution, immediately followed by cleaning the sample with distilled water. This selectively etched ferrite phase and left the austenite unetched. The microstructures were also characterized at higher magnifications using a TESCAN scanning electron microscope at an electron accelerating voltage of 20 kV.

The L-PBF as-printed samples were subjected to tensile testing in an MTS Exceed hydraulic dual-column tensile testing system equipped with a 100 kN load cell, at a strain rate of 0.001 s⁻¹. The elongation of the samples was measured as the increase in gauge length prior to and after the tensile testing.

The corrosion properties of the as-printed samples were characterized in a 3.5% sodium chloride solution to simulate the salinity of the seawater. Using Linear sweep voltammetry (LSV). A pre-defined area was polished to mirror-like surface finish along the scan direction (XY) and was exposed to a 3.5% sodium chloride electrolyte. The as-printed sample served as the working electrode, a silver-silver chloride electrode

served as the reference electrode and a platinum wire mesh served as a counter electrode. All the electrodes were immersed in the sodium chloride electrolyte and externally connected through a potentiostat. The voltage was swept across -1 V to 2 V using the potentiostat and the corrosion current was recorded. The corrosion resistance was calculated using the Tafel plots and Tafel equations [2,11], to obtain polarization resistance, breakdown potential, corrosion current and the corrosion rate.

Results & Discussion

Figure 5.1 Shows as-printed L-PBF samples printed in N atmosphere. Cracks were clearly visible in the banks of tensile samples in the regions closer to base plate. No such cracks were formed in as-printed L-PBF samples printed in Ar atmosphere.

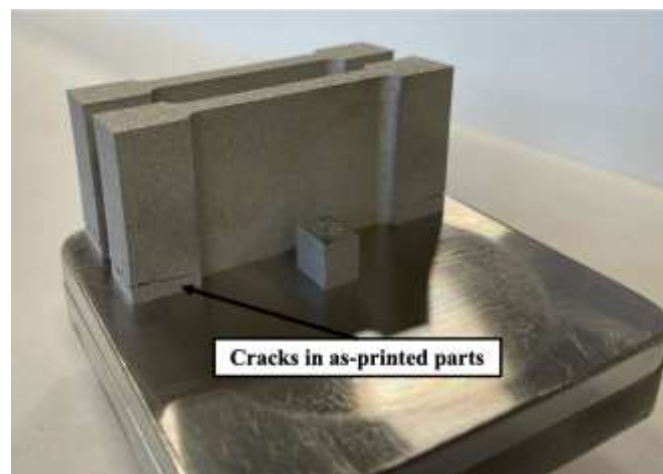


Figure 5.1 As-printed L-PBF samples fabricated from gas atomized 25Cr7Ni stainless steel under N atmosphere

The nitrogen content of the samples printed in Ar atmosphere was recorded to be $0.2597 \pm 0.003\%$ and in the N atmosphere was recorded to be $0.2683 \pm 0.001\%$.

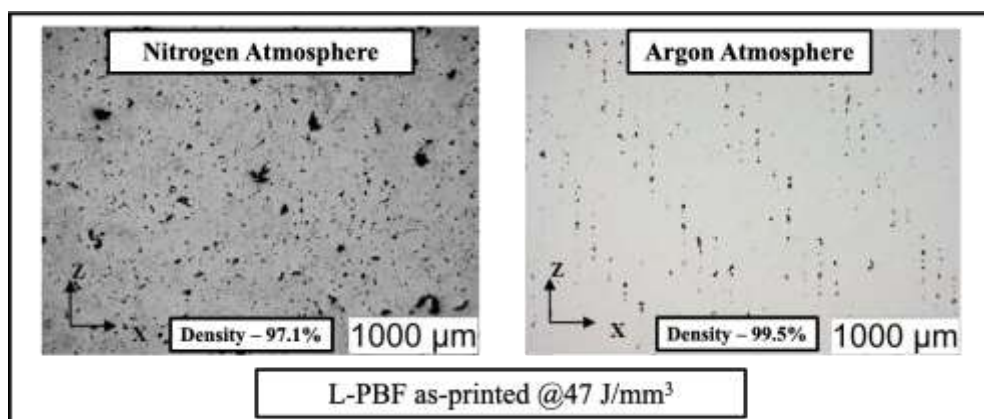


Figure 5.2 Polished optical micrographs along build direction (ZX)

Based on the pycnometer density of the starting 25Cr7Ni stainless steel powder (7.66 ± 0 g/cc), the samples printed in N atmosphere had a relative density of around 97.1% in comparison to 99.5% in samples fabricated in Ar atmosphere. The as-polished

micrographs of the samples along the build direction ZX revealed anisotropic pore distribution in samples printed in N atmosphere in comparison to a periodic distribution of pores in the samples printed in Ar atmosphere. The maximum size of pores also varied between the samples printed in the two different atmospheres with the samples printed in N atmosphere being 50 μm and the maximum size of pores in the samples printed in Ar atmosphere being 5 μm . The ordered / repeating & shifting of pores in the samples printed in Ar atmosphere indicates a possible co-relation to the 45° hatch angle used in the process parameter [12]. Nitrogen has a higher thermal conductivity than Ar, resulting in a faster heat removal from the melt formed during fabrication of samples in N atmosphere, leading to certain lack of fusion pores [2].

Table 5.2: Comparison of Mechanical Properties

Sample Type	Hardness (HRC)	Tensile strength (MPa)	Yield strength (MPa)	Strain (%)	Relative Density (%)
L-PBF 25Cr7Ni in N <i>present work</i>	40 ± 2	1030 ± 60	191 ± 38	8.3 ± 1	97.1
L-PBF 25Cr7Ni in Ar <i>present work</i>	41 ± 2	1375 ± 55	501 ± 40	15 ± 1	99.5

Samples printed in Ar atmosphere had a higher UTS, yield strength, elongation, over samples printed from the same starting powder, process parameters in N atmosphere. Presence of over 3% porosity could account for the reduced mechanical properties [2]. Hardness for both sets of samples were comparable in spite of higher porosity. From [4,13], an increase in part porosity has a limiting effect on the hardness of the L-PBF samples. However, the relatively higher (equal to the value of L-PBF samples printed in Ar atmosphere) seemed counter-intuitive.

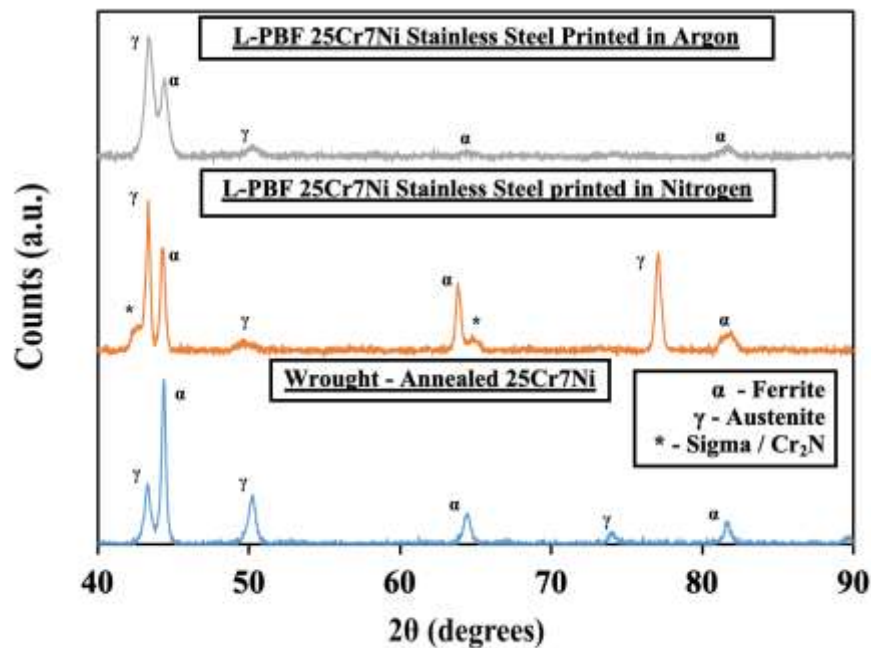


Figure 5.3 Collated XRD profiles of wrought & L-PBF samples

The x-ray diffraction profiles of the L-PBF samples printed in Ar / N atmosphere along with a wrought annealed 25Cr7Ni stainless steel are collated in Figure 3. Both the L-PBF samples recorded both ferrite ($2\theta = 44^\circ, 64^\circ, 81^\circ$) and austenite ($2\theta = 43^\circ, 50^\circ,$

74°) phases in the as-printed state. The L-PBF samples printed in N atmosphere additionally displayed peaks corresponding to chromium nitride / sigma phase. The presence of nitride precipitates could reason the higher values of hardness in L-PBF samples printed in N atmosphere in-spite of their porosity.

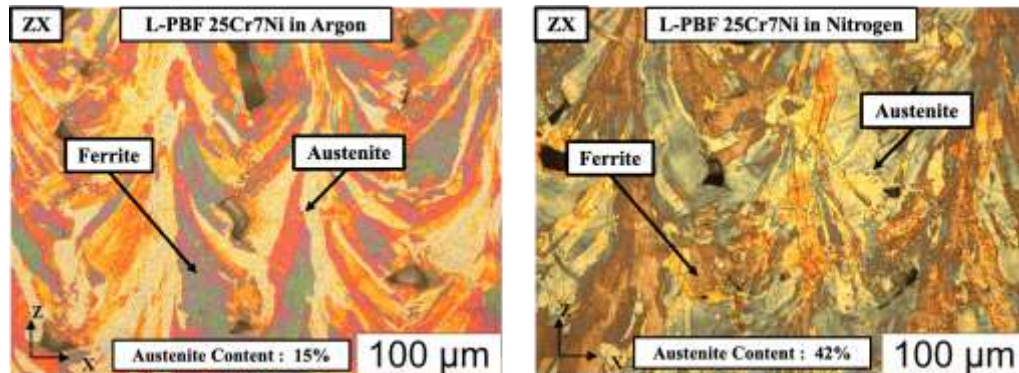


Figure 5.4 Electro-etched optical micrographs of L-PBF samples

Electro-etching of the 25Cr7Ni stainless steel samples, selectively etch the ferrite phase. Both sets of L-PBF samples, one printed in Ar atmosphere and the other printed in N atmosphere etched to reveal both ferrite and austenite phases corroborating the XRD results. The fraction of each individual phases was measured by ‘Image J’ software. The samples printed in the N atmosphere had over 40% austenite in the as-printed state compared to 15% austenite in the as-printed L-PBF samples printed in Ar atmosphere. This observation corroborated the thesis for this study which sought to leverage the solubility of N in stainless steel to promote and stabilize the evolution of austenite phase in the as-printed state. The significantly higher fraction of austenite phase in the as-printed L-PBF samples did not translate to a higher elongation as seen in [14]. This could be reasoned through the porosity present within the sample [15] as well as the secondary phases / precipitates observed in the XRD profiles of L-PBF samples printed in the nitrogen atmosphere [16].

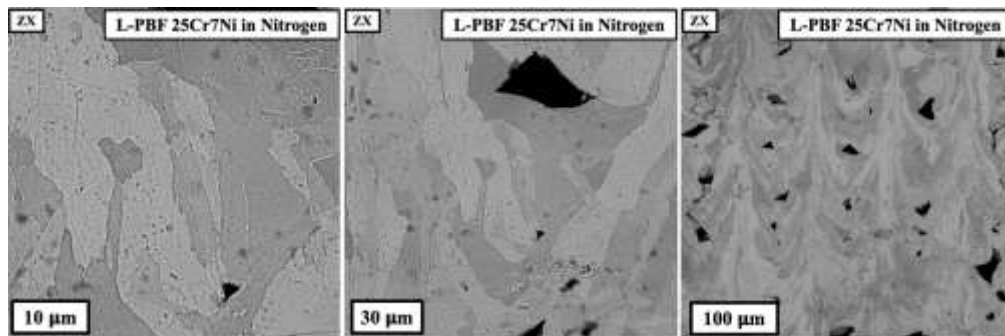


Figure 5.5 Electro-etched SEM micrographs of 25Cr7Ni L-PBF sample printed in N atmosphere

Resolving the anisotropic pores observed in the as-printed L-PBF samples fabricated under the N atmosphere observed under a light microscope, under a higher magnification scanning electron microscope, a preferential distribution of pores was observed. Apart from the larger lack of fusion pores these pores seem to have predominantly initiated along the melt-pool boundary indicating these pores not having been a result of lack of fusion pores. The observations could be explained by, ‘Nitrogen Porosity’, a phenomenon commonly encountered in laser based fabrication of stainless

steels which employ nitrogen as a cover gas [17,18]. These processes, which are defined by high cooling rates, saturate the stainless-steel melt with nitrogen under the applied vapour pressure. The melt due to the said high cooling rates, predominantly solidify as ferrite phase, which has poor solubility for nitrogen. Schwarz et al. [19] showed that, the nitrogen from the super saturated stainless matrix lead to the formation of nitride precipitates and nitrogen pores mainly along the grain boundaries. This further lends credibility to the notion of the pores observed in the present study along the melt-pool boundaries to be nitrogen-based porosities.

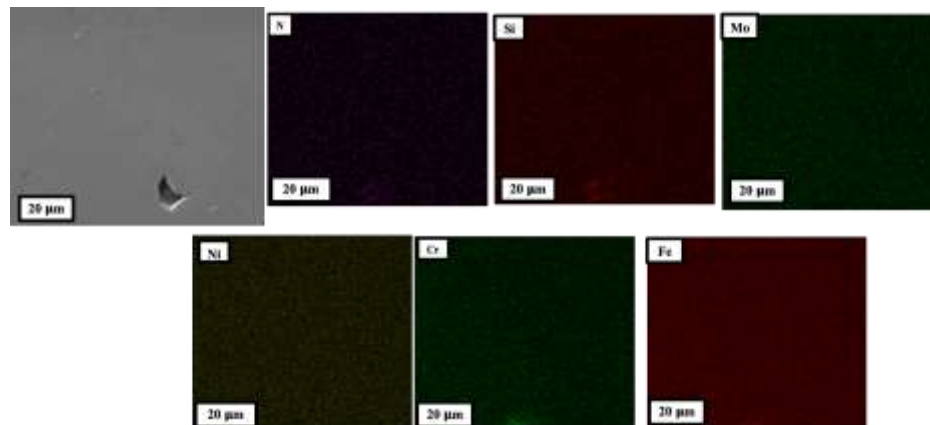


Figure 5.6 Energy Dispersive Spectroscopy of 25Cr7Ni L-PBF sample printed in N atmosphere

From the energy dispersive spectroscopy, no significant elemental partitioning between the ferrite and austenite phases were observed. Nitrogen enriched precipitates were recorded in the EDS maps, corroborating the XRD profiles for the presence of nitride precipitates in the L-PBF samples fabricated in the N atmosphere.

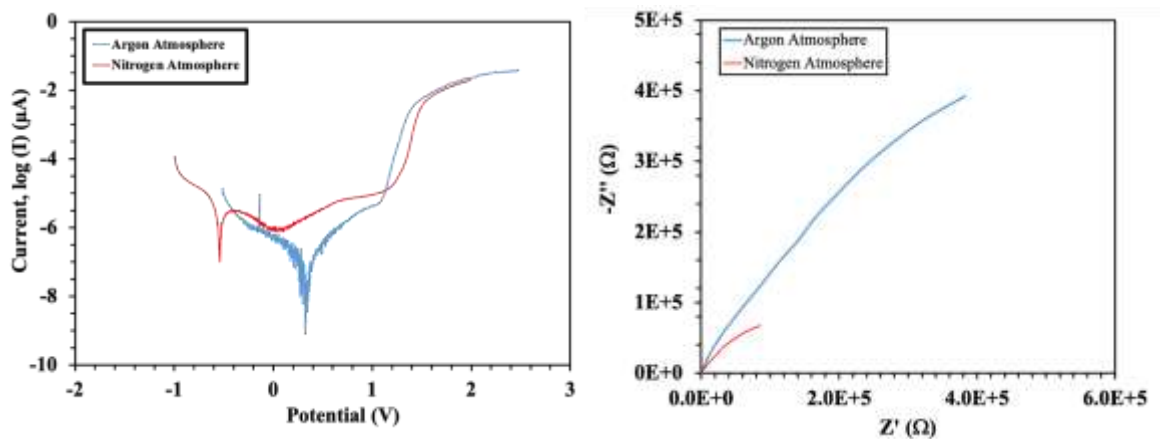


Figure 5.7 Comparison of (left) Tafel plots, (right) Nyquist plots of 25Cr7Ni L-PBF samples

Linear sweep voltammetry experiments and frequency response analyser experiments were used to characterize the Tafel and Nyquist plot responses for both sets of L-PBF samples and are collated in the Figure. L-PBF samples printed in the Ar atmosphere had a higher corrosion potential and charge transfer resistance than the L-PBF samples printed in N atmosphere. This indicates a higher propensity for corrosion among the L-PBF samples printed in N atmosphere than the samples printed in Ar atmosphere. Both samples had similar breakdown potential.

Table 5.3: Comparison of Corrosion Properties

Fabrication Atmosphere	Relative Density (%)	Corrosion Current, I_{corr} (μA)	Breakdown Potential, E_b (V)	Polarization Resistance, R_p (Ω/cm^2) $\times 10^5$	Corrosion Rate ($\mu\text{m}/\text{year}$)
Argon	99.5	0.06 ± 0.04	1.1 ± 0.02	6.3 ± 0.6	3.05 ± 2
Nitrogen	97.1	1.6 ± 0.4	1.15 ± 0.03	0.18 ± 0.3	80 ± 15

From the Tafel plots, corrosion properties were calculated based on Tafel equations [2,20]. The corrosion resistance of the L-PBF samples printed in the Ar atmosphere, was about 30 times greater than the L-PBF samples printed in N atmosphere in terms of a lower corrosion current and a higher polarization resistance. The observed behaviour could be reasoned through porosity [21] and based on sensitization from nitride precipitates [22]. In terms of porosity, localized acidification of the electrolyte that accumulates in the pores lead to the increase in corrosion of the samples [23,24]. A higher porosity than the L-PBF samples printed in Ar atmosphere, could be one of the reasons to the lower corrosion resistance of the L-PBF samples printed in N atmosphere. With respect to sensitization, Cr, Mo are some of the primary passivating elements in the stainless steel system and their depletion from the alloy open nitride precipitation leads to reduction in the corrosion resistance of the sample [25]. The presence of nitride precipitates in the L-PBF samples fabricated in the N atmosphere as corroborated by the XRD and EDS characterization could also aid in reasoning their lower corrosion resistance.

Conclusions

- The 25Cr7Ni stainless steel L-PBF samples fabricated in N atmosphere had a near duplex microstructure with 42% austenite, 58% ferrite in comparison to the samples printed in Ar atmosphere with 15% austenite, 85% ferrite
- The cracks in the as-printed parts and the higher porosity in the 25Cr7Ni stainless steel L-PBF samples printed in N atmosphere based on higher thermal conductivity of N leading to higher rate of heat removal from the melt in L-PBF fabrication causing lack of fusion pores and can also be attributed to the supersaturation of the stainless steel melt with N during melting / solidification of the L-PBF process which manifests as ‘Nitrogen Porosity’, anisotropic pores observable under optical microscope under higher resolution SEM showing a preferential evolution at the austenite / ferrite grain boundary
- With respect to phases evolved in the as-printed state, in comparison to samples printed in the Ar atmosphere which had ferrite and austenite, the samples printed

in the N atmosphere had, apart from ferrite and austenite, XRD peaks related to sigma phase and nitride phases corroborated by the EDS results

- The relatively poor UTS, elongation of the L-PBF samples printed in N atmosphere can be attributed to the brittle sigma phase & nitrides. The poor corrosion properties of the same samples compared to the L-PBF samples printed in Ar is related to the higher porosity & 'Sensitization' from the nitride precipitates

CHAPTER 6 CONCLUSIONS & FUTURE WORK

The present study set out with a scope of addressing the research gap by establishing the influence of L-PBF process parameters, starting powder attributes & chemical composition, effect of hot isostatic pressing and the fabrication atmosphere (N & Ar) on the physical, mechanical & corrosion properties of L-PBF fabricated 25Cr7Ni stainless steels. The conclusions from the studies and the potential for the extension of the work are listed in the following sections.

Conclusions

From chapter 2, effect of various L-PBF process parameters on the physical, mechanical and corrosion properties of a water-atomized 25Cr7Ni stainless steel powder fabricated through L-PBF were examined. The results from the study identified energy density as a critical factor, with the final density, mechanical and corrosion properties of samples increasing with increase in energy density. All the as-printed L-PBF samples of water atomized 25Cr7Ni stainless steel displayed a single phase ferritic microstructure. A higher UTS, yield strength (**1050 ± 15 & 990 ± 2 MPa**) in comparison to wrought, MIM, PM sintered 25Cr7Ni stainless steel alloy was recorded with the samples printed at 54 J/mm^3 . The as-printed samples fabricated at 63 J/mm^3 a corrosion rate of around **$5.7 \pm 2 \text{ } \mu\text{m/year}$** that was comparable to that of wrought 25Cr7Ni stainless steel **$5.01 \pm 0.7 \text{ } \mu\text{m/year}$** , possibly due to lack of nitrogen in the as-printed samples preventing **sensitisation** despite the presence of only ferritic microstructure.

Chapter 3 investigated the effects of hot isostatic pressing on the physical, mechanical and corrosion properties along with the microstructures of 25Cr7Ni stainless steels fabricated by L-PBF from a water atomized powder. The HIP treated samples achieved densification with corresponding reduction in porosity in both HIP conditions. An

increase in relative density from **$97 \pm 0.1\%$** to **$98.4 \pm 0.03\%$** @HIP₁₀₀₀ & **$98.2 \pm 0.02\%$** @ HIP₁₁₇₀ were observed. A duplex microstructure was achieved under both HIP conditions. With the evolution of austenite phase, the HIP treated samples recorded a decrease in UTS and hardness in comparison to as-printed samples. The variation in the morphology of the evolved austenite grains in the HIP treated samples affected their

elongation, with increase in elongation from **$12 \pm 0.6\%$** in as-printed condition to **$18 \pm 2\%$** @ HIP₁₀₀₀ was observed. No increase in elongation @ HIP₁₁₇₀ was observed. With reduction in porosity and evolution of austenite phase, the HIP treated samples showed a higher corrosion resistance in comparison top as-printed samples.

From Chapter 4, the influence of powder attributes, chemical composition on the samples from gas atomized, and water atomized 25Cr7Ni stainless steel powders, fabricated through L-PBF, on their as-printed microstructure and properties were

examined. The gas atomized powders with their spherical and uniform morphology yielded as-printed parts of higher relative densities over water atomized powders with irregular morphology, due to better powder bed compaction. The higher densification obtained in L-PBF samples from gas atomized powders translated to the highest UTS, hardness among L-PBF samples from gas atomized powders (**1375 ± 55 MPa & 41 ± 2 HRC**) than samples from water atomized powders and wrought – annealed 25Cr7Ni stainless steel. Presence of higher amounts of N, Mn in the chemical composition of the gas atomized powders over water atomized powders promoted the presence of retained austenite and elongation in the corresponding L-PBF samples. Higher amounts of Mo, combined with austenite content yielded a higher corrosion resistance of the L-PBF samples from the gas atomized powder than the L-PBF samples from the water atomized powders.

Chapter 5 investigated the effects of varying the fabrication atmosphere between Ar and N during L-PBF fabrication of a gas atomized 25Cr7Ni stainless steel powder. Samples fabricated in N atmosphere had a near duplex microstructure in the as-printed state compared to samples printed in Ar atmosphere due to N being a strong austenite stabilizer. The samples fabricated in N atmosphere presented with increased porosity, partly due to the higher thermal conductivity of N atmosphere leading to higher cooling rates of the melt causing large lack of fusion pores. Similarly, the XRD profiles of the samples fabricated in the N atmosphere presented with peaks corresponding to sigma phase and nitride precipitates in addition to the ferrite, austenite peaks. The additional N dissolution in the 25Cr7Ni stainless steel system during the L-PBF fabrication under the N atmosphere resulted in super saturation of the 25Cr7Ni system. The excess N in the alloy led to precipitation of nitrides along the grain boundaries & detrimental phases within the samples. The porosity along with the presence of brittle detrimental phases resulted in a reduced elongation of **8%** despite the presence of **42%** austenite in the samples printed under N atmosphere in comparison to samples printed under Ar atmosphere which had an elongation of around **15%** with **15%** austenite. Concurrently, the samples printed in N atmosphere also had lower UTS and yield strength (**1030 ± 60 & 191 ± 2 MPa**) than the samples printed in Ar atmosphere (**1375 ± 55 & 501 ± 40 MPa**). The corrosion properties of the samples printed in N atmosphere were also affected by the presence of chromium nitrides due to sensitization, with the corrosion rate more than **25** times that of samples printed in Ar atmosphere.

Future Work

The present study has generated quantitative relationship in terms of correlating the variation in the as-printed properties of L-PBF fabricated 25Cr7Ni stainless steel with the L-PBF process parameters, starting powder attributes / chemical composition, HIP treatment and fabricating atmosphere. Albeit the thesis provides a good starting point in addressing the research gap present in L-PBF fabrication of 25Cr7Ni stainless steel, it also offers interesting avenue for extending the current work to extend the value addition for L-PBF fabrication of 25Cr7Ni stainless steels.

From chapters 2 & 3, the ability of the economical water atomized 25Cr7Ni stainless steel powder (compared to gas atomized 25Cr7Ni stainless steel powder), to produce samples through L-PBF with corrosion properties in the as-printed state comparable to wrought – annealed 25Cr7Ni stainless steels was established. The main limitation was the lack of austenite evolution in the as-printed state due to the lack of N in this specific composition of water atomized 25Cr7Ni stainless steel. From chapter 5, the ability of using a N atmosphere during L-PBF fabrication of 25Cr7Ni stainless steel powder to fabricate samples with near duplex microstructure was documented. However, the gas atomized powder used in that specific study had 0.2% N inherently within its composition, which resulted in N supersaturation leading to detrimental phases / nitride precipitation. Instead, a study centred on using the water atomized powders with N deficient composition for L-PBF fabrication under N atmosphere would be a very interesting avenue to explore.

The HIP treatment parameters used in chapter 3 can be further expanded for different HIP temperatures under 1170° C and for different colling rates to further suppress the precipitate / detrimental phase formation.

Functional parts with actual application-based design requirements made from conventional steels can be explored for fabrication with 25Cr7Ni stainless steel through L-PBF. Under this scope, an ASTM standard flange design was modified to be fabricated through L-PBF without the use of supports by minimizing the overhangs greater than 45°. The generated design was qualified for structural integrity using thermo-mechanical simulations and fabricated using a water atomized 25Cr7Ni stainless steel powder at 63J/mm³ under Ar atmosphere. The as-printed part had a relative density of over 95%. Exploring the avenues for improving the L-PBF fabricated functional part density and properties based on the correlations established in this thesis can be another avenue for extending this work



Figure 6.1. L-PBF fabricated water atomized 25Cr7Ni stainless steel based flange design to be used in underwater offshore oil rigs – the original design was modified to be printed without the use of supports while fabricating through L-PBF primarily to limit post-processing enabling on-site L-PBF fabrication on oil rigs

Using L-PBF process simulation platforms such as ‘Simufact’ & ‘Ansys Additive’ as tools for predicting print errors. The authenticity of the data from the simulation must be established prior to using the platforms as predictive tools. To this end ‘Simufact’ simulation was used to compare the displacement results obtained through simulating a L-PBF fabrication of a simple 25Cr7Ni cube with the experimental results obtained from L-PBF fabrication of gas atomized 25Cr7Ni stainless steel under N atmosphere. This work is presently under development.

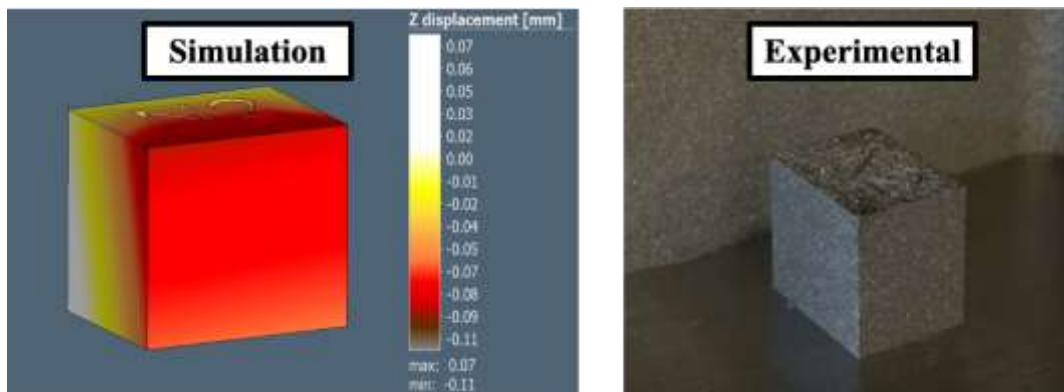


Figure 6.2. Comparison of simulation data with experimental data of L-PBF fabricated 25Cr7Ni stainless steel cube under N atmosphere

REFERENCES

Chapter 1:

- [1] Hosoi Y. Introduction to stainless steel. *Keikinzoku/Journal Japan Inst Light Met* 1987;37:624–35. <https://doi.org/10.2464/jilm.37.624>.
- [2] Bramfitt BL, Bescoter AO. Introduction to Steels and Cast Irons. *Metallogr Guid* 2019;1–21. <https://doi.org/10.31399/asm.tb.mgppis.t60400001>.
- [3] Gu D, Shen Y. Processing conditions and microstructural features of porous 316L stainless steel components by DMLS. *Appl Surf Sci* 2008;255:1880–7. <https://doi.org/10.1016/j.apsusc.2008.06.118>.
- [4] Chail G, Kangas P. Super and hyper duplex stainless steels: Structures, properties and applications. *Procedia Struct Integr* 2016;2:1755–62. <https://doi.org/10.1016/j.prostr.2016.06.221>.
- [5] Duplex Stainless Steels Microstructure, Properties and Applications. *Anti-Corrosion Methods Mater* 1998. <https://doi.org/10.1108/acmm.1998.12845bae.001>.
- [6] Charles Bernhardsson, S., J. Duplex stainless steels '91 : 28-30 Octobre 1991, Beaune, Bourgogne, France, Les Ulis, France: ?ditions de Physique; 1991.
- [7] Chen TH, Yang JR. Effects of solution treatment and continuous cooling on σ -phase precipitation in a 2205 duplex stainless steel. *Mater Sci Eng A* 2001. [https://doi.org/10.1016/S0921-5093\(01\)00911-X](https://doi.org/10.1016/S0921-5093(01)00911-X).
- [8] Charles J. Duplex Stainless Steels' 91, Proc. Conf. Les Ed Phys Paris, Fr 1991.
- [9] Davanageri MB, Narendranath S, Kadoli R, Chen TH, Weng KL, Yang JR, et al. Influence of heat treatment on microstructure, hardness and wear behavior of super duplex stainless steel AISI 2507. *Am J Mater Sci* 2015;5:48–52. <https://doi.org/10.5923/c.materials.201502.10>.
- [10] Larsson L, Berglund T. Effect of Processing Parameters on Intermetallic Phase Content and Impact Toughness for Super Duplex Alloy PM HIP Sandvik SAF 2507TM. *Hot Isostatic Press HIP'17* 2019;10:128–34. <https://doi.org/10.21741/9781644900031-18>.
- [11] Calliari I, Ramous E, Bassani P. Phase transformation in duplex stainless steels after isothermal treatments, continuous cooling and cold working. *Mater Sci Forum* 2010;638–642:2986–91. <https://doi.org/10.4028/www.scientific.net/MSF.638-642.2986>.
- [12] Sato YS, Kokawa H. Preferential precipitation site of sigma phase in duplex stainless steel weld metal. *Scr Mater* 1999. [https://doi.org/10.1016/S1359-6462\(98\)00483-7](https://doi.org/10.1016/S1359-6462(98)00483-7).
- [13] Sieurin H, Sandström R. Sigma phase precipitation in duplex stainless steel 2205. *Mater Sci Eng A* 2007;444:271–6. <https://doi.org/10.1016/j.msea.2006.08.107>.
- [14] Schulz Z, Whitcraft P, Wachowiak D. Availability and economics of using duplex stainless steels. *NACE - Int. Corros. Conf. Ser.*, 2014.
- [15] Zwiren A, Schade C, Hoeges S. Economic Additive Manufacturing using

- Water Atomized Stainless Steel Powder n.d.:1–16.
- [16] Gu D. Laser additive manufacturing of high-performance materials. *Laser Addit Manuf High-Performance Mater* 2015;1–311. <https://doi.org/10.1007/978-3-662-46089-4>.
- [17] Raffeis I, Vroomen U, Adjei-Kyeremeh F, Großmann D, Hammelrath H, Westhoff E, et al. Comparative investigations into microstructural and mechanical properties of as-cast and laser powder bed fusion (LPBF) fabricated duplex steel (1.4517). *Materwiss Werksttech* 2020. <https://doi.org/10.1002/mawe.201900136>.
- [18] Saeidi K, Kevetkova L, Lofaj F, Shen Z. Novel ferritic stainless steel formed by laser melting from duplex stainless steel powder with advanced mechanical properties and high ductility. *Mater Sci Eng A* 2016;665:59–65. <https://doi.org/10.1016/j.msea.2016.04.027>.
- [19] Arumugham Akilan A, Nath SD, Enneti RK, Gupta G, Atre S V. Mechanical and corrosion properties of gas and water atomized laser-powder bed fusion fabricated 25Cr7Ni stainless steel. *Manuf Lett* 2021. <https://doi.org/https://doi.org/10.1016/j.mfglet.2021.07.006>.
- [20] Kusuma C. The Effect of Laser Power and Scan Speed on Melt Pool Characteristics of Pure Titanium and Ti-6Al-4V Alloy for Selective Laser Melting The Effect of Laser Power and Scan Speed on Melt Pool Characteristics of Pure Titanium and Ti-6Al-4V alloy for Selective. *Wright State Univ* 2014:127. <https://doi.org/10.1007/s10704-016-0096-8>.
- [21] Brika SE, Letenneur M, Dion CA, Brailovski V. Influence of particle morphology and size distribution on the powder flowability and laser powder bed fusion manufacturability of Ti-6Al-4V alloy. *Addit Manuf* 2020. <https://doi.org/10.1016/j.addma.2019.100929>.
- [22] Schwarz B, Göhring H, Meka SR, Schacherl RE, Mittemeijer EJ. Pore Formation Upon Nitriding Iron and Iron-Based Alloys: The Role of Alloying Elements and Grain Boundaries. *Metall Mater Trans A Phys Metall Mater Sci* 2014;45:6173–86. <https://doi.org/10.1007/s11661-014-2581-x>.
- [23] Davanageri MB, Narendranath S, Kadoli R. Influence of heat treatment on microstructure, hardness and wear behavior of super duplex stainless steel AISI 2507. *Am J Mater Sci* 2015;5:48–52. <https://doi.org/10.5923/c.materials.201502.10>.
- [24] Reed RP. Nitrogen in austenitic stainless steels. *JOM* 1989. <https://doi.org/10.1007/BF03220991>.
- [25] Nath SD, Irrinki H, Gupta G, Kearns M, Gulsoy O, Atre S. Microstructure-property relationships of 420 stainless steel fabricated by laser-powder bed fusion. *Powder Technol* 2019;343:738–46. <https://doi.org/10.1016/j.powtec.2018.11.075>.
- [26] Irrinki H, Nath SD, Akilan AA, Atre S V. Laser Powder Bed Fusion. *Addit Manuf Process* 2020;24:0. <https://doi.org/10.31399/asm.hb.v24.a0006621>.

Chapter 2:

- [1] Hengsbach F, Koppa P, Duschik K, Holzweissig MJ, Burns M, Nellesen J, et al. Duplex stainless steel fabricated by selective laser melting - Microstructural and mechanical properties. *Mater Des* 2017;133:136–42. <https://doi.org/10.1016/j.matdes.2017.07.046>.
- [2] Irrinki H. Material-process-property relationships of 17-4 stainless steel fabricated by laser-powder bed fusion followed by hot isostatic pressing 2018.
- [3] Davidson KP, Singamneni SB. Metallographic evaluation of duplex stainless steel powders processed by selective laser melting. *Rapid Prototyp J* 2017;23:1146–63. <https://doi.org/10.1108/RPJ-04-2016-0053>.
- [4] Nath SD. Process-property-microstructure relationships in laser-powder bed fusion of 420 stainless steel . 2018.
- [5] Gu D. Laser additive manufacturing of high-performance materials. *Laser Addit Manuf High-Performance Mater* 2015:1–311. <https://doi.org/10.1007/978-3-662-46089-4>.
- [6] Duplex Stainless Steels Microstructure, Properties and Applications. *Anti-Corrosion Methods Mater* 1998. <https://doi.org/10.1108/acmm.1998.12845bae.001>.
- [7] Duplex Stainless Steels Microstructure, Properties and Applications. *Anti-Corrosion Methods Mater* 1998. <https://doi.org/10.1108/acmm.1998.12845bae.001>.
- [8] Raffeis I, Vroomen U, Adjei-Kyeremeh F, Großmann D, Hammelrath H, Westhoff E, et al. Comparative investigations into microstructural and mechanical properties of as-cast and laser powder bed fusion (LPBF) fabricated duplex steel (1.4517). *Materwiss Werksttech* 2020. <https://doi.org/10.1002/mawe.201900136>.
- [9] Saeidi K, Kevetkova L, Lofaj F, Shen Z. Novel ferritic stainless steel formed by laser melting from duplex stainless steel powder with advanced mechanical properties and high ductility. *Mater Sci Eng A* 2016;665:59–65. <https://doi.org/10.1016/j.msea.2016.04.027>.
- [10] Zwiren A, Schade C, Hoeges S. Economic Additive Manufacturing using Water Atomized Stainless Steel Powder n.d.:1–16.
- [11] Dobrzański LA, Brytan Z, Grande MA, Rosso M. Properties of duplex stainless steels made by powder metallurgy. *Arch Mater Sci Eng* 2007.
- [12] Lippold JC. *Welding Metallurgy and Weldability*. 2014. <https://doi.org/10.1002/9781118960332>.
- [13] Iams AD, Keist JS, Palmer TA. Formation of Austenite in Additively Manufactured and Post-Processed Duplex Stainless Steel Alloys. *Metall Mater Trans A Phys Metall Mater Sci* 2020. <https://doi.org/10.1007/s11661-019-05562-w>.
- [14] Mansouri K, Ibrik K, Bensalah N, Abdel-Wahab A. Anodic dissolution of pure aluminum during electrocoagulation process: Influence of supporting electrolyte, initial pH, and current density. *Ind Eng Chem Res* 2011. <https://doi.org/10.1021/ie201206d>.
- [15] Burstein GT, Pistorius PC. Surface roughness and the metastable pitting of stainless steel in chloride solutions. *Corrosion* 1995. <https://doi.org/10.5006/1.3293603>.
- [16] Burstein GT, Pistorius PC, Mattin SP. The nucleation and growth of corrosion

Chapter 3:

- [1] Duplex Stainless Steels Microstructure, Properties and Applications. Anti-Corrosion Methods Mater 1998. <https://doi.org/10.1108/acmm.1998.12845bae.001>.
- [2] Elmer JW, Palmer TA, Specht ED. Direct observations of sigma phase formation in duplex stainless steels using In-situ synchrotron X-ray diffraction. Metall Mater Trans A Phys Metall Mater Sci 2007;38:464–75. <https://doi.org/10.1007/s11661-006-9076-3>.
- [3] Chen TH, Yang JR. Effects of solution treatment and continuous cooling on σ -phase precipitation in a 2205 duplex stainless steel. Mater Sci Eng A 2001. [https://doi.org/10.1016/S0921-5093\(01\)00911-X](https://doi.org/10.1016/S0921-5093(01)00911-X).
- [4] Llorca-Isern N, López-Luque H, López-Jiménez I, Biezma MV. Identification of sigma and chi phases in duplex stainless steels. Mater Charact 2016;112:20–9. <https://doi.org/10.1016/j.matchar.2015.12.004>.
- [5] Iams AD, Keist JS, Palmer TA. Formation of Austenite in Additively Manufactured and Post-Processed Duplex Stainless Steel Alloys. Metall Mater Trans A Phys Metall Mater Sci 2020. <https://doi.org/10.1007/s11661-019-05562-w>.
- [6] Hengsbach F, Koppa P, Duschik K, Holzweissig MJ, Burns M, Nellesen J, et al. Duplex stainless steel fabricated by selective laser melting - Microstructural and mechanical properties. Mater Des 2017;133:136–42. <https://doi.org/10.1016/j.matdes.2017.07.046>.
- [7] Saeidi K, Kevetkova L, Lofaj F, Shen Z. Novel ferritic stainless steel formed by laser melting from duplex stainless steel powder with advanced mechanical properties and high ductility. Mater Sci Eng A 2016;665:59–65. <https://doi.org/10.1016/j.msea.2016.04.027>.
- [8] Raffeis I, Vroomen U, Adjei-Kyeremeh F, Großmann D, Hammelrath H, Westhoff E, et al. Comparative investigations into microstructural and mechanical properties of as-cast and laser powder bed fusion (LPBF) fabricated duplex steel (1.4517). Materwiss Werksttech 2020. <https://doi.org/10.1002/mawe.201900136>.
- [9] Davidson KP, Singamneni SB. Metallographic evaluation of duplex stainless steel powders processed by selective laser melting. Rapid Prototyp J 2017;23:1146–63. <https://doi.org/10.1108/RPJ-04-2016-0053>.
- [10] Redjaimia A, Prout A, Donnadiou P, Morniroli JP. Morphology, crystallography and defects of the intermetallic χ -phase precipitated in a duplex ($\delta + \gamma$) stainless steel. J Mater Sci 2004;39:2371–86. <https://doi.org/10.1023/B:JMISC.0000019999.27065.13>.
- [11] Igual Muñoz A, García Antón J, Guiñón JL, Pérez Herranz V. Effect of nitrogen in Argon as a shielding gas on tungsten inert gas welds of duplex stainless steels. Corrosion 2005;61:693–705. <https://doi.org/10.5006/1.3278204>.
- [12] Sola A, Nouri A. Microstructural porosity in additive manufacturing: The formation and detection of pores in metal parts fabricated by powder bed fusion. J Adv Manuf Process 2019;1. <https://doi.org/10.1002/amp2.10021>.
- [13] Bean GE, Witkin DB, McLouth TD, Patel DN, Zaldivar RJ. Effect of laser focus shift on surface quality and density of Inconel 718 parts produced via selective laser melting. Addit Manuf 2018;22:207–15.

- <https://doi.org/10.1016/j.addma.2018.04.024>.
- [14] Kunz J, Boontanom A, Herzog S, Suwanpinij P, Kaletsch A, Broeckmann C. Influence of hot isostatic pressing post-treatment on the microstructure and mechanical behavior of standard and super duplex stainless steel produced by laser powder bed fusion. *Mater Sci Eng A* 2020;794:139806. <https://doi.org/10.1016/j.msea.2020.139806>.
- [15] Gu D. Laser additive manufacturing of high-performance materials. *Laser Addit Manuf High-Performance Mater* 2015:1–311. <https://doi.org/10.1007/978-3-662-46089-4>.
- [16] Gu D, Shen Y. Processing conditions and microstructural features of porous 316L stainless steel components by DMLS. *Appl Surf Sci* 2008;255:1880–7. <https://doi.org/10.1016/j.apsusc.2008.06.118>.
- [17] Attar H, Calin M, Zhang LC, Scudino S, Eckert J. Manufacture by selective laser melting and mechanical behavior of commercially pure titanium. *Mater Sci Eng A* 2014;593:170–7. <https://doi.org/10.1016/j.msea.2013.11.038>.
- [18] Ronneberg T, Davies CM, Hooper PA. Revealing relationships between porosity, microstructure and mechanical properties of laser powder bed fusion 316L stainless steel through heat treatment. *Mater Des* 2020;189:108481. <https://doi.org/10.1016/j.matdes.2020.108481>.
- [19] M. Hatherly FJH. Recrystallization and related annealing phenomena. 2003.
- [20] Davanageri MB, Narendranath S, Kadoli R. Influence of heat treatment on microstructure, hardness and wear behavior of super duplex stainless steel AISI 2507. *Am J Mater Sci* 2015;5:48–52. <https://doi.org/10.5923/c.materials.201502.10>.
- [21] Rocha Cronemberger ME, Nakamatsu S, Della Rovere C, Kuri S, Mariano N. Effect of Cooling Rate on the Corrosion Behavior of As-Cast SAF 2205 Duplex Stainless Steel After Solution Annealing Treatment. *Mater Res* 2015;18. <https://doi.org/10.1590/1516-1439.352114>.
- [22] Kisasoz A, Karaaslan A, Bayrak Y. Effect of etching methods in metallographic studies of duplex stainless steel 2205. *Met Sci Heat Treat* 2017. <https://doi.org/10.1007/s11041-017-0081-5>.
- [23] Chen TH, Weng KL, Yang JR. The effect of high-temperature exposure on the microstructural stability and toughness property in a 2205 duplex stainless steel. *Mater Sci Eng A* 2002;338:259–70. [https://doi.org/10.1016/S0921-5093\(02\)00093-X](https://doi.org/10.1016/S0921-5093(02)00093-X).
- [24] Nath SD, Irrinki H, Gupta G, Kearns M, Gulsoy O, Atre S. Microstructure-property relationships of 420 stainless steel fabricated by laser-powder bed fusion. *Powder Technol* 2019;343:738–46. <https://doi.org/10.1016/j.powtec.2018.11.075>.
- [25] Irrinki H. Material-process-property relationships of 17-4 stainless steel fabricated by laser-powder bed fusion followed by hot isostatic pressing 2018.
- [26] Voronenko BI. Austenitic-ferritic stainless steels: A state-of-the-art review. *Met Sci Heat Treat* 1997;39:428–37. <https://doi.org/10.1007/bf02484228>.
- [27] Sander G, Thomas S, Cruz V, Jurg M, Birbilis N, Gao X, et al. On The Corrosion and Metastable Pitting Characteristics of 316L Stainless Steel Produced by Selective Laser Melting. *J Electrochem Soc* 2017;164:C250–7. <https://doi.org/10.1149/2.0551706jes>.
- [28] Bayoumi FM, Ghanem WA. Effect of nitrogen on the corrosion behavior of austenitic stainless steel in chloride solutions. *Mater Lett* 2005.

Chapter 4:

- [1] Duplex Stainless Steels Microstructure, Properties and Applications. Anti-Corrosion Methods Mater 1998.
<https://doi.org/10.1108/acmm.1998.12845bae.001>.
- [2] Engineering C. Chapter 05: Corrosion Resistance of Stainless Steels 1 n.d.:1–61.
- [3] Davanageri MB, Narendranath S, Kadoli R, Chen TH, Weng KL, Yang JR, et al. Influence of heat treatment on microstructure, hardness and wear behavior of super duplex stainless steel AISI 2507. Am J Mater Sci 2015;5:48–52.
<https://doi.org/10.5923/c.materials.201502.10>.
- [4] Llorca-Isern N, López-Luque H, López-Jiménez I, Biezma MV. Identification of sigma and chi phases in duplex stainless steels. Mater Charact 2016;112:20–9. <https://doi.org/10.1016/j.matchar.2015.12.004>.
- [5] Gu D. Laser additive manufacturing of high-performance materials. Laser Addit Manuf High-Performance Mater 2015:1–311.
<https://doi.org/10.1007/978-3-662-46089-4>.
- [6] Guo A, Beddow JK, Vetter AF. A simple relationship between particle shape effects and density, flow rate and Hausner Ratio. Powder Technol 1985.
[https://doi.org/10.1016/0032-5910\(85\)80009-7](https://doi.org/10.1016/0032-5910(85)80009-7).
- [7] Zwiren A, Schade C, Hoeges S. Economic Additive Manufacturing using Water Atomized Stainless Steel Powder n.d.:1–16.
- [8] Lawley A. Atomization. Encycl. Mater. Sci. Technol., 2001.
<https://doi.org/10.1016/b0-08-043152-6/00077-2>.
- [9] Nath SD. Process-property-microstructure relationships in laser-powder bed fusion of 420 stainless steel . 2018.
- [10] Irrinki H. Material-process-property relationships of 17-4 stainless steel fabricated by laser-powder bed fusion followed by hot isostatic pressing 2018.
- [11] Prof. Dr. Viktor Pocajt. Water Atomization Process: Part Two. Total Mater 2013:2021.
- [12] Reed RP. Nitrogen in austenitic stainless steels. JOM 1989.
<https://doi.org/10.1007/BF03220991>.
- [13] Tsuge H, Tarutani Y, Kudo T. EFFECT OF NITROGEN ON THE LOCALIZED CORROSION RESISTANCE OF DUPLEX STAINLESS STEEL SIMULATED WELDMENTS. Corrosion 1988.
<https://doi.org/10.5006/1.3583942>.
- [14] Saeidi K, Kevetkova L, Lofaj F, Shen Z. Novel ferritic stainless steel formed by laser melting from duplex stainless steel powder with advanced mechanical properties and high ductility. Mater Sci Eng A 2016;665:59–65.
<https://doi.org/10.1016/j.msea.2016.04.027>.
- [15] Hengsbach F, Koppa P, Duschik K, Holzweissig MJ, Burns M, Nellesen J, et al. Duplex stainless steel fabricated by selective laser melting - Microstructural and mechanical properties. Mater Des 2017;133:136–42.
<https://doi.org/10.1016/j.matdes.2017.07.046>.
- [16] Davidson KP, Singamneni SB. Metallographic evaluation of duplex stainless steel powders processed by selective laser melting. Rapid Prototyp J 2017;23:1146–63. <https://doi.org/10.1108/RPJ-04-2016-0053>.
- [17] Raffeis I, Vroomen U, Adjei-Kyeremeh F, Großmann D, Hammelrath H, Westhoff E, et al. Comparative investigations into microstructural and

- mechanical properties of as-cast and laser powder bed fusion (LPBF) fabricated duplex steel (1.4517). *Materwiss Werksttech* 2020;51:432–44.
<https://doi.org/10.1002/mawe.201900136>.
- [18] Nath SD. ThinkIR : The University of Louisville ’ s Institutional Repository Process-property-microstructure relationships in laser-powder bed fusion of 420 stainless steel . 2018.
- [19] Chao Q, Cruz V, Thomas S, Birbilis N, Collins P, Taylor A, et al. On the enhanced corrosion resistance of a selective laser melted austenitic stainless steel. *Scr Mater* 2017;141:94–8.
<https://doi.org/10.1016/j.scriptamat.2017.07.037>.
- [20] Anderson IE, White EMH, Dehoff R. Feedstock powder processing research needs for additive manufacturing development. *Curr Opin Solid State Mater Sci* 2018;22:8–15. <https://doi.org/https://doi.org/10.1016/j.cossms.2018.01.002>.
- [21] Tan JH, Wong WLE, Dalgarno KW. An overview of powder granulometry on feedstock and part performance in the selective laser melting process. *Addit Manuf* 2017;18:228–55.
<https://doi.org/https://doi.org/10.1016/j.addma.2017.10.011>.
- [22] Wischeropp TM, Emmelmann C, Brandt M, Pateras A. Measurement of actual powder layer height and packing density in a single layer in selective laser melting. *Addit Manuf* 2019;28:176–83.
<https://doi.org/https://doi.org/10.1016/j.addma.2019.04.019>.
- [23] Fedina T, Sundqvist J, Powell J, Kaplan AFH. A comparative study of water and gas atomized low alloy steel powders for additive manufacturing. *Addit Manuf* 2020;36:11. <https://doi.org/10.1016/j.addma.2020.101675>.
- [24] Li R, Shi Y, Wang Z, Wang L, Liu J, Jiang W. Densification behavior of gas and water atomized 316L stainless steel powder during selective laser melting. *Appl Surf Sci* 2010;256:4350–6.
<https://doi.org/https://doi.org/10.1016/j.apsusc.2010.02.030>.
- [25] Martin AA, Calta NP, Khairallah SA, Wang J, Depond PJ, Fong AY, et al. Dynamics of pore formation during laser powder bed fusion additive manufacturing. *Nat Commun* 2019;10:1987. <https://doi.org/10.1038/s41467-019-10009-2>.
- [26] Ly S, Rubenchik AM, Khairallah SA, Guss G, Matthews MJ. Metal vapor micro-jet controls material redistribution in laser powder bed fusion additive manufacturing. *Sci Rep* 2017;7:4085. <https://doi.org/10.1038/s41598-017-04237-z>.
- [27] Kaplan AFH, Powell J. Spatter in laser welding. *J Laser Appl* 2011;23:32005.
<https://doi.org/10.2351/1.3597830>.
- [28] Duplex Stainless Steels Microstructure, Properties and Applications. *Anti-Corrosion Methods Mater* 1998.
<https://doi.org/10.1108/acmm.1998.12845bae.001>.
- [29] Lippold JC. *Welding Metallurgy and Weldability*. 2014.
<https://doi.org/10.1002/9781118960332>.
- [30] Folkhard E. Significance of Constitution Diagrams for the Understanding of Welding Phenomena BT - *Welding Metallurgy of Stainless Steels*. In: Folkhard E, editor., Vienna: Springer Vienna; 1988, p. 1–51.
https://doi.org/10.1007/978-3-7091-8965-8_1.
- [31] Saeidi K, Gao X, Lofaj F, Kvetková L, Shen ZJ. Transformation of austenite to duplex austenite-ferrite assembly in annealed stainless steel 316L consolidated

- by laser melting. *J Alloys Compd* 2015;633:463–9. <https://doi.org/10.1016/j.jallcom.2015.01.249>.
- [32] Chail G, Kangas P. Super and hyper duplex stainless steels: Structures, properties and applications. *Procedia Struct Integr* 2016;2:1755–62. <https://doi.org/10.1016/j.prostr.2016.06.221>.
- [33] Buchanan RA, Stansbury EE. Electrochemical corrosion. 2005. <https://doi.org/10.1016/B978-081551500-5.50007-0>.
- [34] Sander G, Thomas S, Cruz V, Jurg M, Birbilis N, Gao X, et al. On The Corrosion and Metastable Pitting Characteristics of 316L Stainless Steel Produced by Selective Laser Melting. *J Electrochem Soc* 2017;164:C250–7. <https://doi.org/10.1149/2.0551706jes>.
- [35] Voronenko BI. Austenitic-ferritic stainless steels: A state-of-the-art review. *Met Sci Heat Treat* 1997;39:428–37. <https://doi.org/10.1007/bf02484228>.
- [36] Ghanem WA. Effect of nitrogen on the corrosion behavior of austenitic stainless steel in chloride solutions. *EUROCORR 2004 - Eur. Corros. Conf. Long Term Predict. Model. Corros.*, 2004. <https://doi.org/10.5539/mas.v9n11p119>.
- [37] Xin R, Wang M, Gao J, Liu P, Liu Q. Effect of Microstructure and Texture on Corrosion Resistance of Magnesium Alloy. *Mater Sci Forum* 2009;610–613:1160–3. <https://doi.org/10.4028/www.scientific.net/MSF.610-613.1160>.
- [38] Li D-W, Wang H-Y, Wei D-S, Zhao Z-X, Liu Y. Effects of Deformation Texture and Grain Size on Corrosion Behavior of Mg-3Al-1Zn Alloy Sheets. *ACS Omega* 2020;5:1448–56. <https://doi.org/10.1021/acsomega.9b03009>.

Chapter 5:

- [1] Gu D. Laser additive manufacturing of high-performance materials. *Laser Addit Manuf High-Performance Mater* 2015:1–311. <https://doi.org/10.1007/978-3-662-46089-4>.
- [2] Nath SD. Process-property-microstructure relationships in laser-powder bed fusion of 420 stainless steel . 2018.
- [3] Irrinki H, Nath SD, Akilan AA, Atre S V. Laser Powder Bed Fusion. *Addit Manuf Process* 2020;24:0. <https://doi.org/10.31399/asm.hb.v24.a0006621>.
- [4] Arumugham Akilan A, Nath SD, Enneti RK, Gupta G, Atre S V. Mechanical and corrosion properties of gas and water atomized laser-powder bed fusion fabricated 25Cr7Ni stainless steel. *Manuf Lett* 2021. <https://doi.org/https://doi.org/10.1016/j.mfglet.2021.07.006>.
- [5] Karlsson L, Pak S, Andersson SL. Microstructure and properties of super duplex stainless weld metals. *Proc. Int. Conf. Stainl. Steels*, 1991.
- [6] Duplex Stainless Steels Microstructure, Properties and Applications. *Anti-Corrosion Methods Mater* 1998. <https://doi.org/10.1108/acmm.1998.12845bae.001>.
- [7] Saeidi K, Kevetkova L, Lofaj F, Shen Z. Novel ferritic stainless steel formed by laser melting from duplex stainless steel powder with advanced mechanical properties and high ductility. *Mater Sci Eng A* 2016;665:59–65. <https://doi.org/10.1016/j.msea.2016.04.027>.
- [8] Iams AD, Keist JS, Palmer TA. Formation of Austenite in Additively Manufactured and Post-Processed Duplex Stainless Steel Alloys. *Metall Mater Trans A Phys Metall Mater Sci* 2020. <https://doi.org/10.1007/s11661-019-05562-w>.
- [9] Davidson KP, Singamneni SB. Metallographic evaluation of duplex stainless steel powders processed by selective laser melting. *Rapid Prototyp J* 2017;23:1146–63. <https://doi.org/10.1108/RPJ-04-2016-0053>.
- [10] Schulz Z, Whitcraft P, Wachowiak D. Availability and economics of using duplex stainless steels. *NACE - Int. Corros. Conf. Ser.*, 2014.
- [11] Chao Q, Cruz V, Thomas S, Birbilis N, Collins P, Taylor A, et al. On the enhanced corrosion resistance of a selective laser melted austenitic stainless steel. *Scr Mater* 2017;141:94–8. <https://doi.org/10.1016/j.scriptamat.2017.07.037>.
- [12] Ertay DS, Ma H, Vlasea M. Correlative beam path and pore defect space analysis for modulated powder bed laser fusion process. *Solid Free Fabr 2018 Proc 29th Annu Int Solid Free Fabr Symp - An Addit Manuf Conf SFF 2018* 2020:272–84.
- [13] Brown SGR, Cherry JA, Davies HM, Mehmood S, Lavery N, Sienz J. Investigation into the Effect of process parameters on microstructural and physical properties of 316L stainless steel parts by selective laser melting. *Int J Adv Manuf Technol* 2014. <https://doi.org/10.1007/s00170-014-6297-2>.
- [14] Hengsbach F, Koppa P, Duschik K, Holzweissig MJ, Burns M, Nellesen J, et al. Duplex stainless steel fabricated by selective laser melting - Microstructural and mechanical properties. *Mater Des* 2017;133:136–42. <https://doi.org/10.1016/j.matdes.2017.07.046>.
- [15] Nath SD. ThinkIR : The University of Louisville ' s Institutional Repository

- Process-property-microstructure relationships in laser-powder bed fusion of 420 stainless steel . 2018.
- [16] Raffeis I, Vroomen U, Adjei-Kyeremeh F, Großmann D, Hammelrath H, Westhoff E, et al. Comparative investigations into microstructural and mechanical properties of as-cast and laser powder bed fusion (LPBF) fabricated duplex steel (1.4517). *Materwiss Werksttech* 2020. <https://doi.org/10.1002/mawe.201900136>.
 - [17] Zhao L, Tian Z, Peng Y. Porosity and nitrogen content of weld metal in laser welding of high nitrogen austenitic stainless steel. *ISIJ Int* 2007;47:1772–5. <https://doi.org/10.2355/isijinternational.47.1772>.
 - [18] Yang SH, Lee ZH. Nitrogen Porosity in Nitrogen Bearing Austenitic Stainless Steel. *Mater Sci Forum* 2005;475–479:2679–82. <https://doi.org/10.4028/www.scientific.net/msf.475-479.2679>.
 - [19] Schwarz B, Göhring H, Meka SR, Schacherl RE, Mittemeijer EJ. Pore Formation Upon Nitriding Iron and Iron-Based Alloys: The Role of Alloying Elements and Grain Boundaries. *Metall Mater Trans A Phys Metall Mater Sci* 2014;45:6173–86. <https://doi.org/10.1007/s11661-014-2581-x>.
 - [20] Buchanan RA, Stansbury EE. Electrochemical corrosion. 2005. <https://doi.org/10.1016/B978-081551500-5.50007-0>.
 - [21] Irrinki H. Material-process-property relationships of 17-4 stainless steel fabricated by laser-powder bed fusion followed by hot isostatic pressing 2018.
 - [22] Burstein GT, Pistorius PC. Surface roughness and the metastable pitting of stainless steel in chloride solutions. *Corrosion* 1995. <https://doi.org/10.5006/1.3293603>.
 - [23] Schaller RF, Taylor JM, Rodelas J, Schindelholz EJ. Corrosion Properties of Powder Bed Fusion Additively Manufactured 17-4 PH Stainless Steel. *Corrosion* 2017;73:796–807. <https://doi.org/10.5006/2365>.
 - [24] Geenen K, Röttger A, Theisen W. Corrosion behavior of 316L austenitic steel processed by selective laser melting, hot-isostatic pressing, and casting. *Mater Corros* 2017;68:764–75. <https://doi.org/10.1002/maco.201609210>.
 - [25] Bassiouni M, Ward L, Singh R, O’Mullane A, Gideon B, Bhargava S. Studies on the degree of sensitization of welded 2507 super duplex stainless steel using a modified DL-EPR test procedure. 2010.

APPENDIX 1. CORROSION PROPERTIES OF LASER-POWDER BED FUSION FABRICATED 25Cr7Ni STAINLESS STEELS

Results

Table 7.1: Comparison of Chemical Compositions

Alloy (%)	Si	P	Cr	Mn	S	Ni	Cu	Mo	W	C	Fe	N
Gas atomized 25Cr7Ni SS	0.5	0.01	25.1	0.9	0.007	7	0.02	3.94	N.A	0.02	Bal.	0.28
Water atomized 25Cr7Ni SS	1.79	0.015	25	0.1	0.009	6.2	2.0	1.3	0.8	0.02	62.79	-
UNS S32750 ASTM	0.8	0.035	24 - 26	1.2	0.02	6 - 8	0.5	3 - 5	0.01	0.03	Bal.	0.24 – 0.32

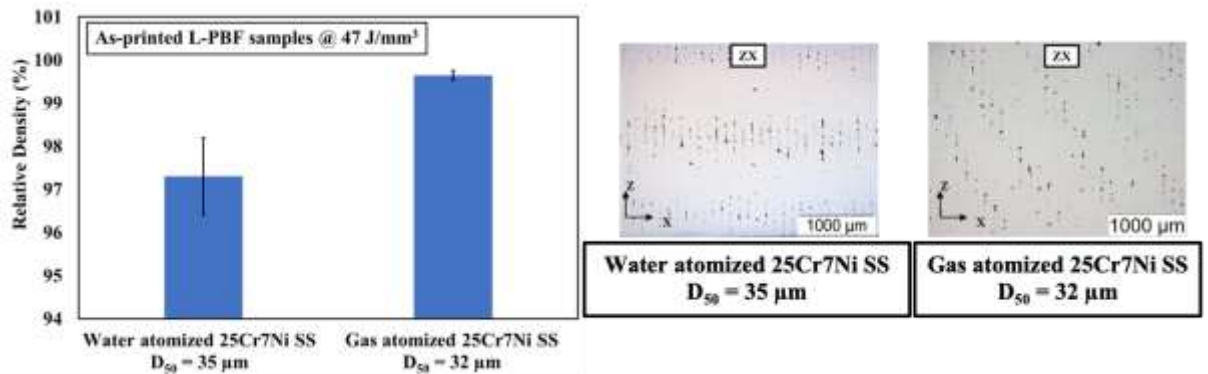
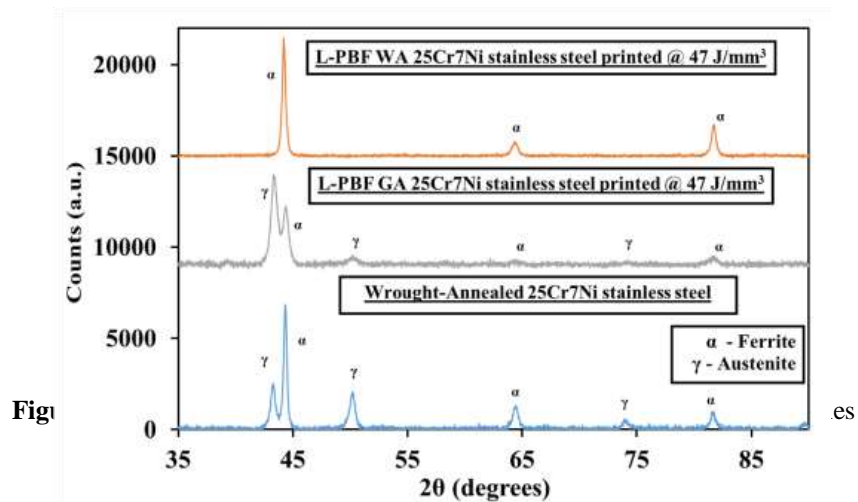


Figure 7.1. Comparison of densities and porosities of as-printed samples



Fig

es

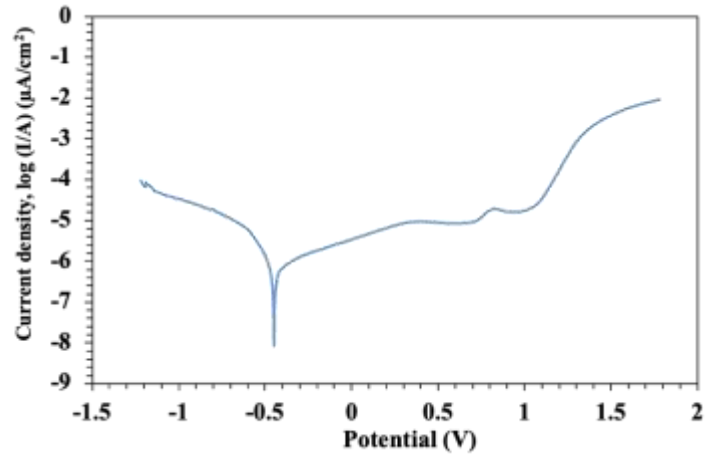
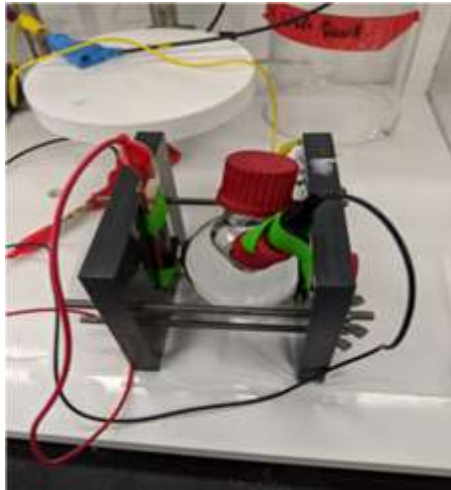


Figure 7.3. FRA – LSV corrosion setup

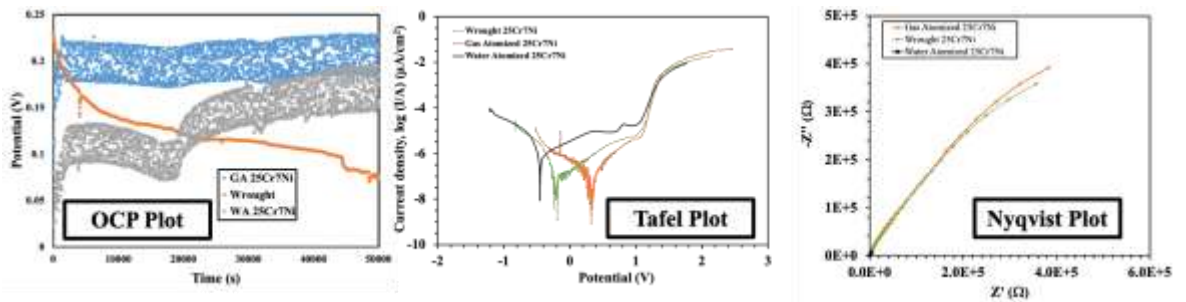


Figure 7.4. FRA / LSV curves for a set of wrought – annealed 25Cr7Ni , L-PBF fabricated water atomized & gas atomized 25Cr7Ni stainless steels

Table 7.2: Comparison of Corrosion Properties

Specimen	Relative Density (%)	Corrosion Current, I_{corr} (μA)	Breakdown Potential, E_b (V)	Polarization Resistance, R_p (Ω/cm^2) $\times 10^5$	Corrosion Rate ($\mu\text{m}/\text{year}$)
L-PBF gas atomized 25Cr7Ni	99.5	0.06 ± 0.04	1.1 ± 0.02	6.3 ± 0.6	3.05 ± 2
L-PBF water atomized 25Cr7Ni	97.6	0.3 ± 0.06	1.0 ± 0.01	1.7 ± 0.1	19.6 ± 1
Wrought 25Cr7Ni	100	0.1 ± 0.01	1.0 ± 0.05	4.4 ± 0.4	5.1 ± 0.7

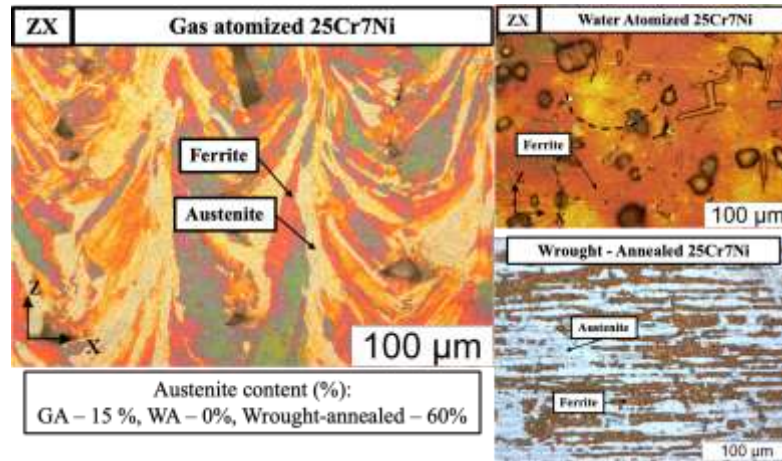


Figure 7.5. Electro-etched 25Cr7Ni stainless steel samples

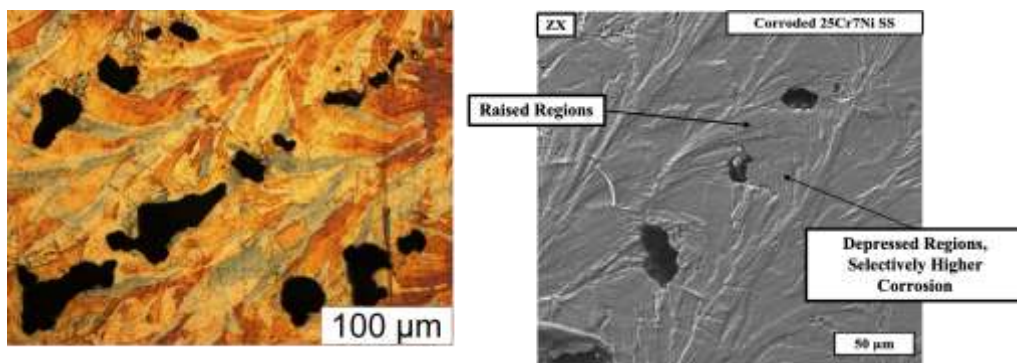


Figure 7.6. Electro-etched corroded sample of a L-PBF fabricated gas atomized 25Cr7Ni stainless steel

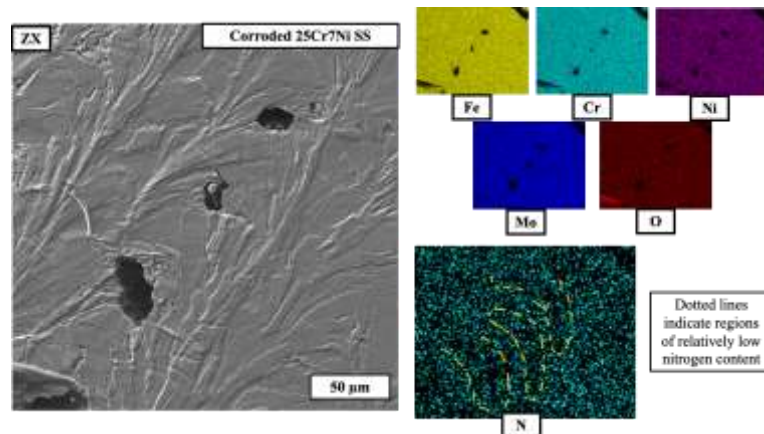


Figure 7.7. EDS maps of electro-etched corroded sample of a L-PBF fabricated gas atomized 25Cr7Ni stainless steel

APPENDIX 2. LASER POWDER BED FUSION OF IN-SITU COMPOSITES USING DRY MIXED Ti6Al4V AND Si₃N₄ POWDER

Results

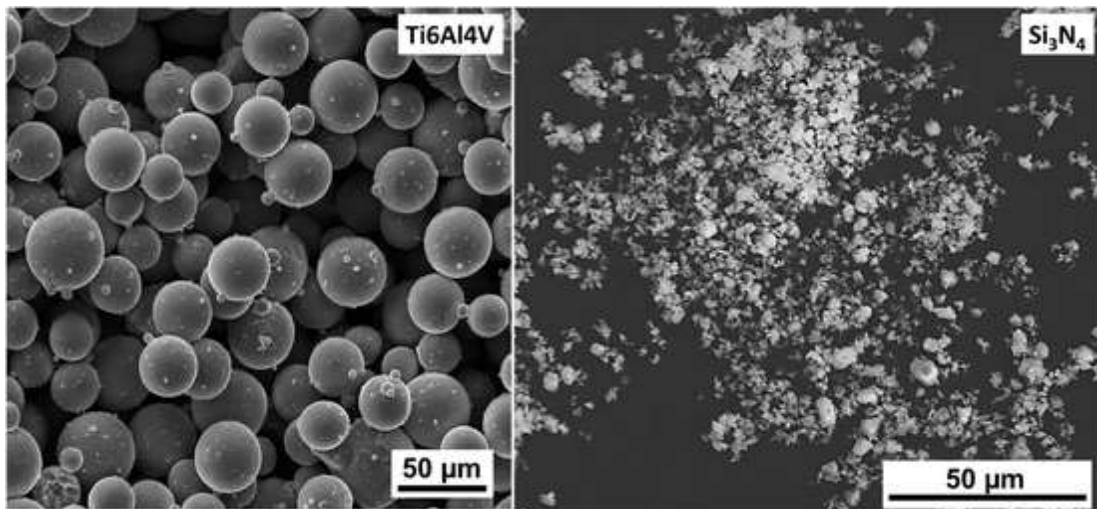


Figure 8.1. SEM images showing the size distribution and morphology of Ti6Al4V alloy and Si₃N₄ powder used in this investigation

Table 8.1: L-PBF Process Parameters

	Processing Conditions				
	Laser power, P (W)	Scan speed, v (mm/s)	Scan spacing, h (μm)	Layer thickness, t (μm)	Energy density $E = P/(v \cdot h \cdot t)$ (J/m ³) x 10 ⁹
1	96	400	90	20	130
2	96	600	90	20	90
3	96	900	90	20	60
4	96	1200	90	20	40

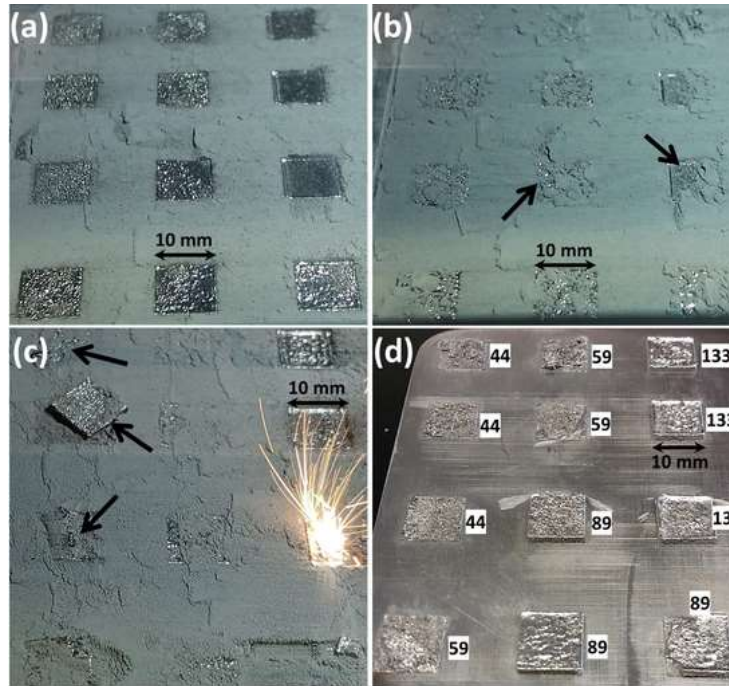


Figure 8.2. Powder bed photographs showing the changes in the powder spreading during L-PBF of Ti-TiN-Ti₅Si₃ in-situ composites (a) Relatively good powder spreading during initial layers, (b) Non-uniform spreading, powder agglomeration and dragging over prior deposits (arrows) after ~200 layers, (c) Aggravated inhomogeneity in powder spreading leading to detachment (arrows) of deposits (44 J/mm³), (d) In-situ composite samples after ~250 layers of printing and the numbers indicate energy density (J/mm³)

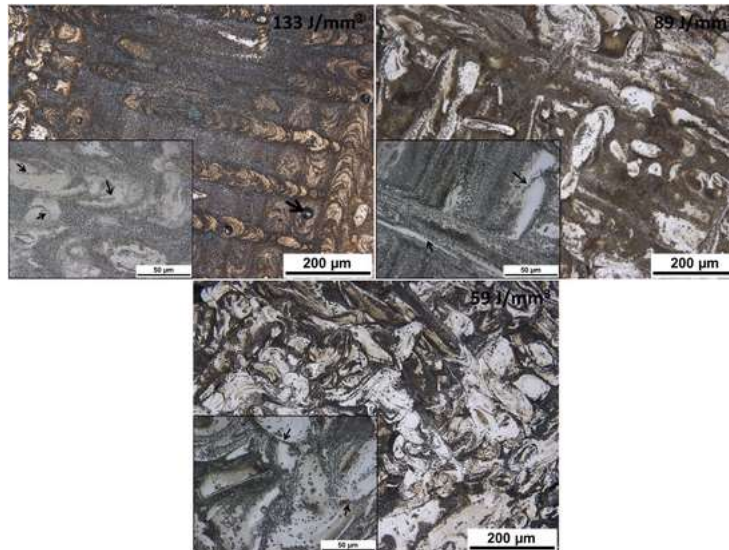


Figure 8.3. Low-magnification microstructures of L-PBF processed Ti-TiN-Ti₅Si₃ in-situ composites showing the influence of laser energy density on the amount of reaction products (dark particles/regions) and their distribution. Insets show migration of in-situ reaction products along the melt pool boundaries (arrows)

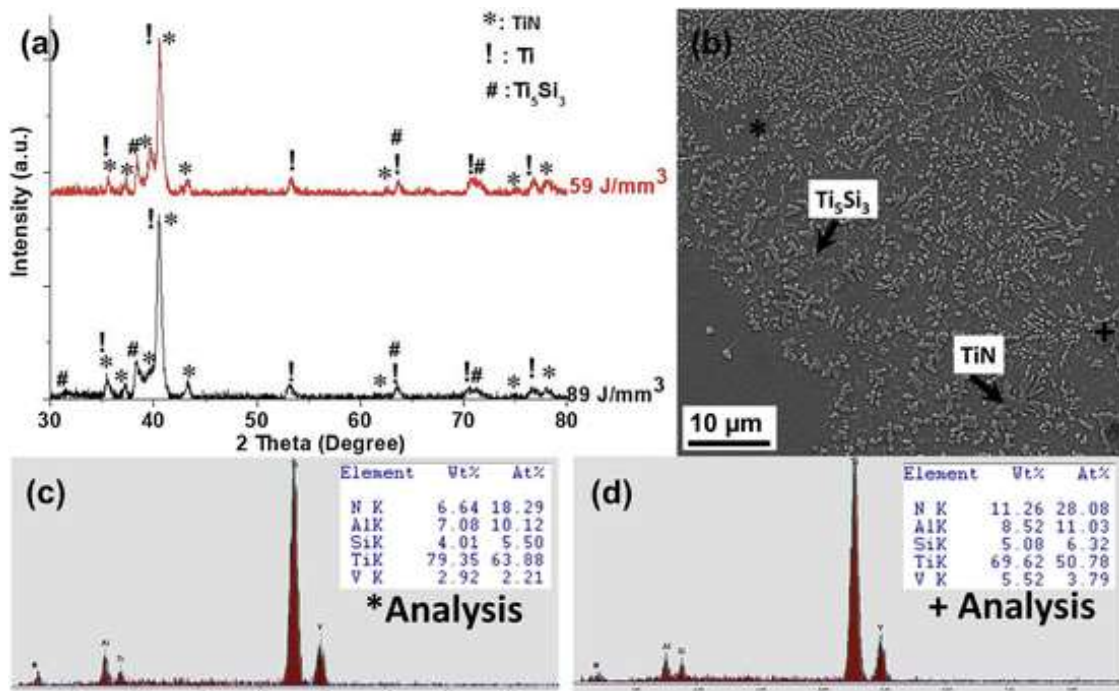


Figure 8.4. (a) XRD analysis showing in-situ reaction products in L-PBF processed TMCs and (b) Typical microstructural features of Ti-TiN-Ti₅Si₃ in-situ composites (89 J/mm³) and their compositional analysis (c and d)

Table 8.2: Composition of different microstructural constituents observed in the L-PBF processed Ti-TiN-Ti₅Si₃ in-situ composites

Energy density, E (J/mm ³)	Ti matrix	Blocky/ dendritic precipitates (TiN)
133	Ti: 77.5 ± 1.4	Ti: 74.4 ± 1.3
	Al: 7.9 ± 0.7	Al: 8.1 ± 0.6
	V: 3.5 ± 0.4	V: 3.1 ± 0.7
	N: 6.7 ± 0.6	N: 10.3 ± 0.9
	Si: 4.3 ± 0.8	Si: 4.1 ± 0.5
	Ti: 71.3 ± 2.8	Ti: 70.7 ± 2.0
89	Al: 9.2 ± 1.1	Al: 9.3 ± 0.7
	V: 4.0 ± 0.8	V: 4.5 ± 0.6
	N: 11.1 ± 1.9	N: 10.8 ± 1.7
	Si: 4.4 ± 0.6	Si: 4.6 ± 1.0

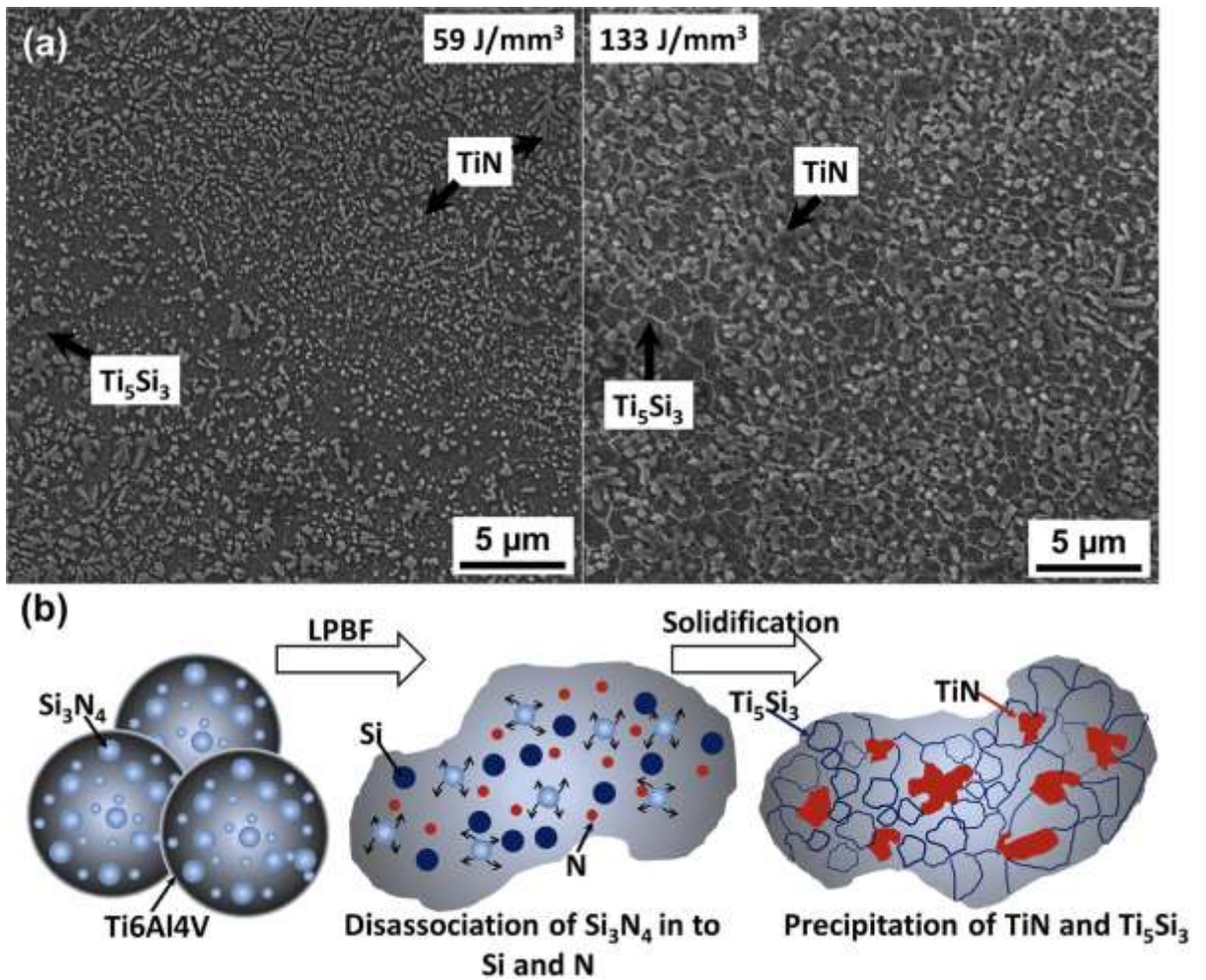


Figure 8.5. (a) Typical SEM microstructures showing the scale and distribution of microstructural features such as grain size and in-situ reaction products in LL-PBF processed Ti-TiN-Ti₅Si₃ in-situ composites. (b) Schematic in-situ reaction forming Ti-TiN-Ti₅Si₃ in-situ composites during LL-PBF of Ti6Al4V+5 wt.% Si₃N₄ dry-mixed feedstock

CURRICULUM VITAE

Arumugham Akilan, Arulselvan
aarulselvan@yahoo.com
+1 713 355 9412

A doctorate in the area of Laser-Powder Bed Fusion focused on stainless steel & titanium alloys with over 5 years of industrial R&D experience from working in/with Volkswagen AG, SLM solutions AG, Desktop Metal, Sandvik Additive, Quintus. Skilled in L-PBF, metallurgy, binder jetting, process simulation, process development, research & development and project management. A strong senior development engineer with a master's in material sciences from Technical University, Darmstadt, Germany and a PhD from the University of Louisville, USA

Summary of Qualifications

Laser-Powder Bed Fusion	Binder Jetting	Sintering
Stainless Steel Alloys	Titanium Alloys	Corrosion Characterization
Precious Metals	Failure Simulation	Non-destructive Testing
Process Development	Hot Iso-static Pressing	Process Simulation
English, German Fluency	Project Leadership	Automation in C++, Python

Education

- 01/2019 – 12/2021 Doctoral Candidate, Mechanical Engineering Department (**GPA: 3.74**), University of Louisville, United States of America
- 10/2012 – 09/2017 Masters, Material Science Department (**GPA: 2.03, 'good'**), Technical University Darmstadt, Germany
- 08/2008 – 04/2012 Bachelors, Mechanical Engineering Department (**CGPA: 8.56**), Anna University, India

Work / Research Experience

- 07/2021 – Present **Senior Development Engineer at Christian Tse Design & Manufacturing /Desktop Metal** under Dr. Animesh Bose

My responsibilities include,

- Qualification & process development/optimization of binder jetting/sintering for precious metals including sterling silver alloys, gold alloys, platinum alloys
- Atomization of precious metals for powder based additive manufacturing processes
- Powder characterization & metallurgy

01/2019 – Present **Doctoral candidate** at the **Additive Manufacturing Institute of Science & Technology** (AMIST) in the Mechanical Engineering Department at the University of Louisville, under Prof. Dr. Sundar V. Atre

- Developed and qualified novel alloy compositions of super duplex stainless steel with **North American Höganäs & Sandvik** for L-PBF
- Characterized and investigated the evolving physical, mechanical and corrosion properties of the L-PBF samples
- Performed process simulation of the L-PBF in Simufact to develop a correlation between experimental and simulation results
- Developed a titanium-based metal matrix composite in L-PBF through in-situ alloying

01/2020 – 12/2020 **Associate production engineer** at **Advanced Energy Materials LLC** under Dr. Sunkara and Dr. He

- Designed and fabricated metal die inserts for lab scale and commercial scale extruders through L-PBF
- Formulated and prepared catalyst-binder powder compositions for extrusion
- Characterized the physical and mechanical properties of the extrudates
- Deputized for the manufacture of reusable N-95 masks during the COVID-19 pandemic by the company

08/2015 – 03/2016 **Research Intern / Master thesis Student** at **SLM Solutions AG** in their Materials Development Department

Topic: ‘Quantification of Process Emissions in Selective Laser Melting into Real-time Temperature Measurement’

- Powder handling, preparation of build chamber prior to and post printing, post treatment of build jobs subjected to selective laser melting
- Calibrated the melt pool monitoring system through design and development of a prototype calibration apparatus for the thermal sensor diodes within the melt-pool monitoring system
- Performed literature and patent survey in optical thermography, SLM process monitoring, MPM, material specific influence of melt pool flow behaviour along with metallurgical analysis, metal powder recycling, analysis of build job porosity

02/2015 – 06/2015 **Research Intern at Volkswagen AG** in their Research and Development Department under Dr. Naake, Anja (K-EFW/S) & Dr. Dewald, Wilma (K-EFW/S)

Topic: ‘Selective Laser Melting of Aluminium & Titanium Alloys along with Optimization of the Process Parameters by Mechanical and Metallurgical Characterization’

- Mechanical, metallurgical characterization of additively manufactured (selective laser melting) build jobs of titanium and aluminium alloys of varying process parameters
- Performed metallography, hardness testing, static tensile testing using optical measurement system, nanoindentation, surface roughness testing

Research Publications

- Authored a paper titled, ‘*Laser powder bed fusion of in-situ composites using dry-mixed Ti-6Al-4V and Si₃N₄ powder*’, Journal of Manufacturing Processes, October 2020 with V. K. Balla, A. Gökce, K. Kate, and S. V. Atre
- Co-authored a chapter entitled, ‘*Additive Manufacturing Processes*’ in ASM Handbook, Vol - 24, with H. Irrinki, S. D. Nath, M. Ahlfors, G. Gupta and S. V. Atre*
- Presented a paper at AMPM 2019, Phoenix & KY NANO + AM 2019, Louisville conferences on the topic of ‘*Mechanical Properties and Corrosion Resistance of Laser - Powder Bed Fusion Processed Stainless Steel of Duplex Composition*’

Fellowship / Grant Awards

- NSF grant recipient, spring 2019, 2021

Skills

Languages	English (Professional and Fluent), German (Fluent in reading, Intermediate in writing and speaking), Tamil (Native tongue)
PC Skills	Simulation software: Solidworks, CAD, ABAQUS with PYTHON scripting, ANSYS, Simufact